

CALIFORNIA STATE POLYTECHNIC UNIVERSITY, POMONA
THESIS ELECTRONIC SIGNATURE PAGE

Submitted: Term spring Year 2021
Bronco ID: 010571743
Email Address: oteller@cpp.edu

THESIS INFORMATION

THESIS TITLE SOURCE(S) OF FLUID DISCHARGE IN FORMER OIL FIELD, WILEY CANYON, CALIFORNIA
AUTHOR Oscar Teller
PROGRAM Geology, M.S.

SIGNATURES

Stephen G Osborn
Committee Chair Name
Thesis Committee Chair
Position
Department of Geological Science
Department
Cal Poly Pomona
Organization


DocuSigned by:
Stephen G Osborn 6/8/2021
B1E6BFB18441457...
Signature
sgosborn@cpp.edu
Email

Nicholas J Van Buer
Committee Member 2 Name
Associate Professor
Position
Department of Geological Science
Department
Cal Poly Pomona
Organization

DocuSigned by:
Nicholas J Van Buer 6/8/2021
ED2E989A7B2A47B...
Signature
njvanbuer@cpp.edu
Email

Bryan P Murray
Committee Member 3 Name
Associate Professor
Position
Department of Geological Science
Department
Cal Poly Pomona
Organization

DocuSigned by:
Bryan P Murray 6/8/2021
20873EBAB5874F6...
Signature
bpmurray@cpp.edu
Email

Upload Thesis Attachment: 

**SOURCE(S) OF FLUID DISCHARGE IN FORMER OIL FIELD, WILEY
CANYON, CALIFORNIA**

A Thesis

Presented to the

Faculty of

California State Polytechnic University, Pomona

In Partial Fulfillment

Of the Requirements for the Degree

Master of Science

In

Geology

By

Oscar Teller

2021

SIGNATURE PAGE

THESIS: SOURCE(S) OF FLUID DISCHARGE IN FORMER
OIL FIELD, WILEY CANYON, CALIFORNIA

AUTHOR: Oscar Teller

DATE SUBMITTED: Spring 2021

Department of Geological Science

Dr. Stephen Osborn
Thesis Committee Chair
Geological Science

Dr. Nicholas Van Buer
Geological Sciences

Dr. Bryan Murray
Geological Sciences

ACKNOWLEDGEMENTS

I could not have completed this research if it weren't for the knowledge gained from every faculty member of Cal Poly Pomona Geological Sciences Department. I have learned a lot from each of you. It has been quite a journey to finally present this research. I would like to especially thank my advisor, Dr. Stephen Osborn, for believing in me and guiding me through this research and Dr. Nick Van Buer for directing me towards a better approach in some of the sections of this research.

“Gracias Totales”

ABSTRACT

Natural oil/gas seeps raise concerns about the potential environmental impact of hyper-saline brine from depth at the surface and shallow aquifers. In Wiley Canyon, California, oil/gas seep discharge at the surface. During the mid-1800s, commercial oil drilling took place in Wiley Canyon, and today is currently used for human recreation as a private park reserve. The motivation for this study was to qualitatively determine the source(s) of waters discharging at the surface and evaluate if there is a geological control on upward fluid migration. Water sampling took place between late summer 2018 and spring 2019 and were classified as groundwater and surface-water. A Thermo Scientific Dionex Ion Chromatography (IC) system was used to measure the waters anions concentration in ppm (precision $\pm 1\%$). Several binary graphs from the anion's concentrations were generated to determined trends and correlations between constituents. On December 2020, joint fractures measurements were obtained from 5 outcrops. The fractures were classified as bedding, longitudinal and transverse fractures, and used to estimate the permeability tensor on each outcrop. Based on the trends observed in the chloride and bromide concentrations, it seems that the discharging waters originate from two water sources. Five samples are from a freshwater source and possibly two out the five are mixing with some sort saline waters. The other two water samples are evident to originate from halite dissolution and mixing with a freshwater source, likely a shallow aquifer. There is a geological control on the oil/gas and water seeps. It is expected, based on the permeability tensor estimation and field observations, that fractures joints might be one of the controlling factors driving fluids upward from depth to the surface and the fracture connectivity network might be acting as preferential pathways for fluid flow.

TABLE OF CONTENTS

Signature Page.....	ii
Acknowledgements.....	iii
Abstract.....	iv
List of Tables	vii
List of Figures	vii
Equations.....	x
Plates.....	xi
Chapter 1: Introduction	1
1.1 Research Questions.....	1
1.2 Wiley Canyon Background.....	2
Chapter 2: Background	7
2.1 Brines Overview..	7
2.2.1 Chloride and Bromide.....	10
2.2.1 Cations and Anions in Brines	13
2.2 Fluid Migration in Sedimentary Basin.....	16
2.3 Fractures and Permeability	20
2.4 Potential Fluid Pathways along Abandoned Oil Wells.....	27
Chapter 3: Geological Setting.....	31
3.1 Regional Geology	31
3.2 Wiley Canyon Geology Relative to the East Ventura Basin	32
3.3 Stratigraphic Sequence of Wiley Canyon.....	35
3.3.1 Pico Formation.....	38

3.3.2 Towsley Formation	39
3.3.3 Modelo Formation	39
3.3 Pico Anticline	40
Chapter 4: Methods.....	41
4.1 Water Sampling..	41
4.2 Laboratory Procedure.....	46
4.3 Geological Measurements.....	47
Chapter 5: Results.....	54
5.1 Physiochemical Parameters..	54
5.2 Analytical Analysis.....	55
5.3 Geological Measurements.....	56
Chapter 6: Discussion	66
6.1 Field Parameters and Water Quality.....	66
6.2 Salinity Source	71
6.3 Fractures and Permeability	77
6.4 Abandoned Oil Wells	82
Chapter 7: Conclusions.....	84
Future Work	85
References.....	86
Appendix.....	92

LIST OF TABLES

Table 1. List of oil production wells drilled in Wiley Canyon	6
Table 2. Stage of evaporation with progressively concentration	10
Table 3. Geological map legend	43
Table 4. Modified table of water harness	46
Table 5. Orientation of a vector by directional cosine	53
Table 6. Trend and plunge of eigenvectors	61
Table 7. Orientation of a vector by directional cosine	56

LIST OF FIGURES

Figure 1. Regional map of Los Angeles and San Fernando Valley with main highways. The research site is marked as a red circle	3
Figure 2. Locations of Wiley Canyon historic hydrocarbon wells modified from Geologic Energy Management Division (Cal GEM) map (2020)	5
Figure 3. Modified graph from Carpenter (1978) research on Brines in Sedimentary Basins. This schematic diagram displayed possible trend between different end members	12
Figure 4. Modified block diagram from Fundamentals of Fluid Flow in Porous Media. The block represents the combination of three parallel rock layers.	19
Figure 5. Modified block diagram from Fundamentals of Fluid Flow in Porous Media. The block diagram represents a linear flow across three perpendicular layers to the steady flow..	20
Figure 6. An illustration of a fault zone, in which includes the damage zone and core.	22
Figure 7. Schematic diagram showing different joint sets configuration during folding their relationship as well with the orientation of tectonic stresses.	24
Figure 8. Block diagram illustrating a single fracture plane. Modified after Mokhtari et al., 2015 geometry of a parallel-plate 3D fracture diagram.	25
Figure 9. Schematic diagrams of an abandoned vertical well with casing strings and cement plugs between two strings, or a string of casing and formation.	30
Figure 10. Modified geological map from Yeast et., al (1994) research on Late Cenozoic tectonics of the east Ventura Basin, Transverse Ranges, California. Wiley Canyon is marked as red square north of the Santa Susana Fault.	31
Figure 11. Modified Paleogeophaphy of the eastern Venture basin during the Miocence time. The location of what is today Wiley Canyon can be seen in the red circle near the Newhall area.	36

Figure 12. Modified stratigraphic column of Newhall (San Fernando Pass) from Yeast et al., (1994) Neogene stratigraphic columns of the east Ventura basin.	37
Figure 13. Cross-sectional overview of the lithological sequence of the Ventura Basin (Campbell et.al, 2014). The black square shows an approximation of the three formations expose in Wiley Canyon..	38
Figure 14. Geological map of Wiley canyon showing the proximity of sampling locations with geological structure. The locations are illustrated as orange circles.	42
Figure 15. Photograph A shows the ocaation of O-S-1, where oil/gas and water are sporadic bubbling. Photograph B shows the location of W-S-1, where water is constantly and violently bubbling. Photograph C shows location W-S-2, where rocks are highly deformed and folded. Photograph D Is a close-up of location W-S-2 as water was being sampled.....	45
Figure 16. Aperture measurement in a transverse fracture on fine-grained sandstone of the Modelo formation using a portable microscope..	51
Figure 17. Field measurements on outcrops. Photograph A illustrates the strike and dip measurements on a fine-grained sandstone bed of the Modelo formation. Photograph B illustrates spacing measurements between bedding fractures on a sandstone outcrop of the Modelo formation. The purple and green lines represent the bedding and longitudinal fractures, respectively... ..	52
Figure 18. Illustration of the cartesian axis together with the angles of directional cosine.....	53
Figure 19. The right stereonet shows the bedding planes of the northern and southern limbs from broadly distributed outcrops. The left stereonet shows the poles to planes and the fold axis of the Pico anticline	56
Figure 20. Total Dissolved Solid (up graph) and Nitrate over Time (down grpah)	70
Figure 21. Binary graph of Chloride vs Bromide. The encircle numbers displayed the possible trends observed in the water samples	74
Figure 22. Binary graph of Chloride/Bromide ratio. The encircle numbers displayed the possible trends observed in the water samples	75

LIST OF EQUATIONS

Equation 1. Darcy’s Law Equation.....	18
Equation 2. Arithmetic-average permeability of parallel layers on a homogenous medium.....	19
Equation 3. Harmonic-average permeability of perpendicular layers on a homogenous medium	20
Equation 4. Single phase fluid flow in a fracture. Simplification of Navier-Stokes equations of fluid continuity	25
Equation 5. Simplification of Darcy’s law equation shown in vector notation.....	27
Equation 6. Mobility ratio of fluids	34
Equation 7. Alkalinity as calcium carbonate	46
Equation 8. Generalized permeability tensor equation.....	49
Equation 9. Permeability tensor of arbitrary single set of parallel fractures	50

LIST OF PLATES

Plate 1. Outcrops Locations with Stereographic Projection of Fracture Joints Planes on Wiley Canyon, California.....	62
Plate 2. Schematic Cross-Section of Potential Fluid Flow Pathways and Fracture Joints Density on Wiley Canyon, California.....	63
Plate 3. Eigenvectors of each Permeability Tensor from Outcrops on Wiley Canyon, California.....	64
Plate 4. Stereographic Projection of Fracture Planes	65

CHAPTER 1:

INTRODUCTION

Natural oil/gas seeps raise concerns about the potential environmental impact of hyper saline brine from depth at the surface and shallow aquifers. There are natural fluids discharging from oil/gas seeps and proximate springs on the surface of Wiley Canyon, California. These fluids are likely mixing with shallow aquifers, and plausibly impacting the southeast portion of the Santa Clara watershed. This canyon is currently used for human recreation as a private park reserve and it is open to the public. Yet, there has been little geochemical and hydrogeological data on the fluids discharging in Wiley Canyon available to the public. The absence of data regarding these fluids prevents a comprehensive understanding about the potential risk associated with hydrocarbon related fluids (hyper-saline waters). Hence, this thesis combines an analytical evaluation on the discharging waters to qualitatively determine the source(s), to understand basic water quality, and to evaluate the potential impact of waters associated with hydrocarbon reservoirs. Additionally, a geological assessment was carried out to establish a correlation between upward fluid migration and geological structures, and a conceptual was utilized to address potential fluid leaks on abandoned oil wells.

1.1 Research Questions

Based on field observations and historical use of Wiley Canyon, the goal is to identify the water source-(s) and address the potential impact on shallow aquifers and pathways for upward fluid movement by answering the following research questions.

- 1) What is/are the environment (s) of the discharging waters found in Wiley Canyon?
 - ❖ Based on historical use and geological setting, the waters discharging in Wiley Canyon may originate from different sources such as meteoric water

or from hydrocarbon reservoir or a combination of both.

2) What is the source of salinity of the waters?

- ❖ Natural brines, which are generally hypersaline waters, are associated with hydrocarbon reservoirs and may act as the main source of salinity on the discharging waters found in Wiley Canyon.
- ❖ Dissolution of evaporates by infiltration of meteoric waters can also act as additional source for salinity.

3) What is the current geological condition of Wiley Canyon?

- ❖ Historically, Wiley Canyon was involved in petroleum production during the late 1800s to the mid-1900 which involved drilling operations, plugging, and abandonment of oil wells.
- ❖ This canyon rests on a structural trough, which is inclined to active deformation. Currently, the main structural feature is the Pico Anticline, where beddings near the axis are highly deformed with near vertical bedding in the northern flank of the anticline and where most of the drilling operations were performed near and on the axis and the northern flank.
- ❖ It's possible that the deformation of the rocks layers together with the deterioration of the abandoned oil wells is acting as preferential pathways for upward fluid migration.

1.2 Wiley Canyon Background

Wiley Canyon is located northwest of Los Angeles and southwest of the City of Santa Clarita (Figure1). The current geological and hydrogeological condition of Wiley Canyon has been of interest due to unusual terrestrial oil/gas seeps and proximate springs.



Figure 1. Regional map of Los Angeles and San Fernando Valley with main highways. The research site is marked as a red circle (modified from USGS National Map 3D Elevation Program (3DEP) on April 2020).

Commercial oil drilling was performed in Wiley Canyon for more than one hundred years (Wilmington Journal, 1866; Walling, 1934: DOGGR records). During the mid-1800s, commercial oil drilling took place in Wiley Canyon, and today it is part of the Newhall Oil Field located in the eastern section of the Ventura Basin. On March 18, 1865, Henry Clay Wiley filed two one-thousand foot claims based on the Los Angeles Asphaltum and Petroleum Mining District (Wilmington Journal, 1866; Walling, 1934: DOGGR records). This claimed was called the “Wiley Lead,” and it is located in what is now Wiley canyon (Wilmington Journal, 1866; Walling, 1934: DOGGR records). The Sacramento Daily Union of March 31, 1865, mentioned the canyon to have more than 100 springs

“where the petroleum exudes out of the stratum of sandstone and decomposed slate.”

Wiley Spring Oil Company carried the initial oil production in 1865, but production was small to make it commercially viable. It was reported that a shallow well, 175-feet deep, was producing a small amount of oil (Peckham, 1866). The deepest well drilled was Wiley 25 with a total depth of 3,835-feet below ground surface (bgs); however, no commercial oil was found and it was abandoned in 1914, and plugged in 1991 (Walling, 1934, and DOGGR records). Historical records show another company, Pacific Coast Oil, drilled the first commercial production well in 1884, Wiley 4, at a depth of 1,275 feet (bgs) (Walling, 1934, and DOGGR records). A total of 29 wells were drilled in Wiley Canyon; however, only wells 18 and 19 yielded high production, and were drilled to 200 feet south of the Pico anticline (DOGGR records). The wells Wiley 18 and 19 produced an average of 83 and 109 barrels per day (bpd), respectively. Both wells were drilled at a depth of $1,518.5 \pm 9.5$ feet (bgs). At the end of 1934, only 8 wells were producing an average of 1.7 barrels of oil and 3.4 of barrels of water per day. The highest production wells were drilled at depths less than 2,000 feet (bgs) and were located adjacent or on the Pico anticline axis (Wilmington Journal, 1866). Today, there are remnants of abandoned oil wells across the canyon and natural oil/gas seeps.

Modified from Walling, a 1934 map of the Newhall oilfield and DOGGR records, Figure 2 and Table 1 illustrate the locations of all wells drilled in Wiley Canyon and summaries significant information for each well, such as original and maximum depth drilled and the year the wells were abandoned and plugged, respectively.

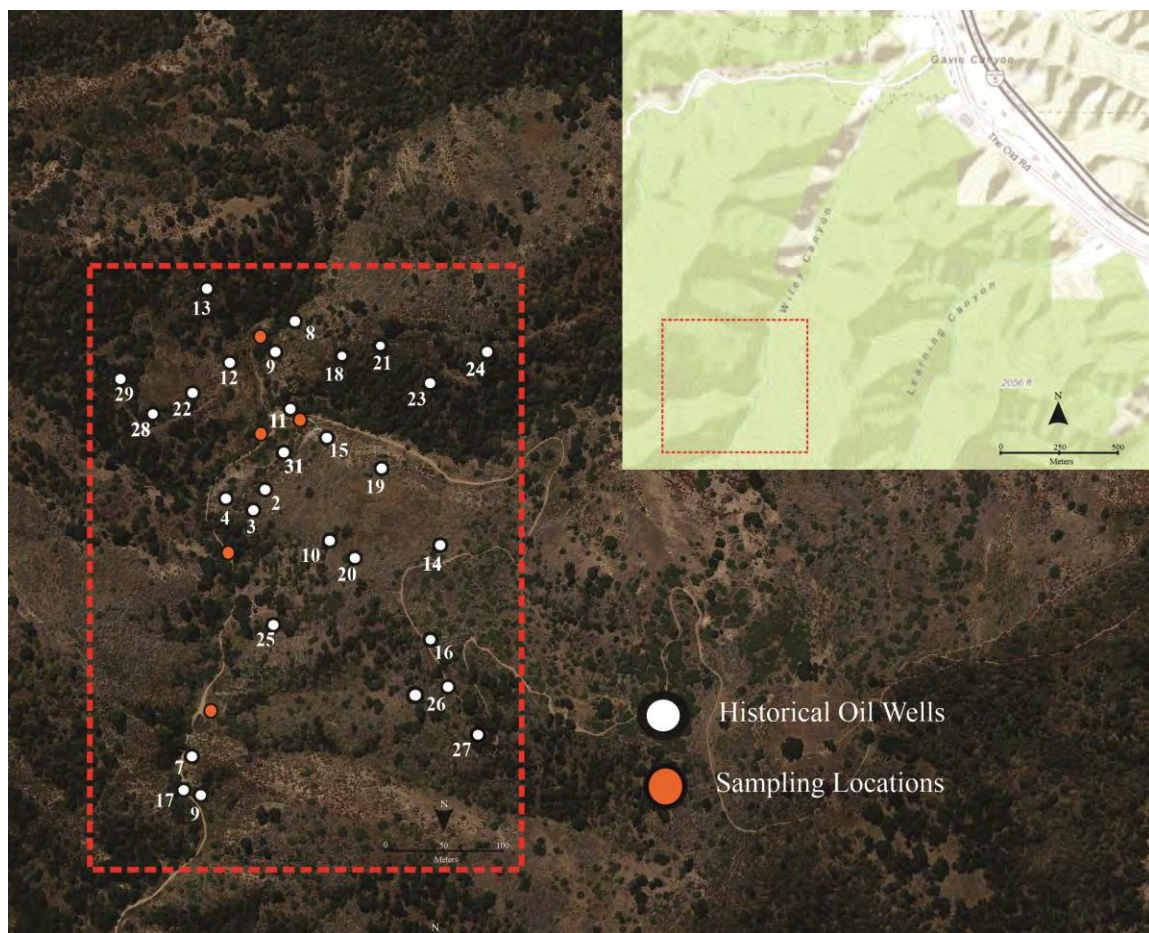


Figure 2. Locations of Wiley Canyon historic hydrocarbon wells modified from Geologic Energy Management Division (Cal GEM) map (2020). Map was obtained from google earth and USGS National Map viewer on April 2020.

In the early 1990's the Santa Monica Mountains Conservancy purchased Wiley Canyon from the Chevron Corporation (Elsmercanyon.com, 2019), and today it is an open space and used for public recreation activities.

Table 1. List of oil production wells drilled in Wiley Canyon with their original/max depth drilled and important remarks of each well (From Walling, 1934, and DOGGR records)

Well ID	Original/Max Depth Drilled (ft)	Statements
1		
2		Abandoned before 1890. Plugged in 1972.
3		Abandoned before 1890. Plugged in 1991.
4	1275	Abandoned in 1884. Plugged in 1991.
5	1408	Troubled with water and abandoned in 1890. Plugged in 1991.
6	435/1258	Plugged in 1972.
7	1200	Abandoned in 1889. Plugged in 1991.
8	970	Excessive water and abandoned. Plugged in 1991.
9	1650	Plugged in 1991.
10	860	Abandoned in 1892. Plugged in 1991.
11	1325	Water below 800 feet. Abandoned 1911. Plugged in 1991.
12	1030/1735	Abandoned 1919. Plugged in 1991.
13	1395/1395	Plugged in 1977.
14	1648	Plugged in 1972
15	0	Never Drilled
16	1730	Abandoned 1921. Plugged in 1991
17	1111	No production, abandoned while drilling. Plugged in 1972.
18	2207	Well flowed while drilling between 1000-1528 ft. Plugged in 1972.
19	1786	Plugged in 1972.
20	2600	Flowing water at 2600 ft. Plugged in 1991.
21	2412	Abandoned in 1911. Unable to plug in 1991
22	390/2280	Excessive water below 500 ft. Plugged in 1977.
23	2181	Excessive water. Abandoned in 1911. Plugged in 1977.
24	1500	Flowing water at 845-860ft. Abandoned and plugged in 1991.
25	3835	Excessive water. Abandoned 1914. Plugged in 1991.
26	1702	Plugged in 1972
27	1712	Plugged in 1972
28	420	Plugged in 1977
29	420	Plugged in 1977.
30	400	Plugged in 1977.
31	2015	Plugged and abandoned in 1956.

CHAPTER 2:

BACKGROUND

The study of brines in oil-production fields has been investigated intensively due to significant influence on oil recovery (Mills and Wells, 1919; Stosessell and Moor, 1985; Franks and Uchytíl, 2016). The variant salinity present in oil-fields significantly effects reservoir calculations (Franks and Uchytíl, 2016). Modifying the water salinity on an oil reservoir has shown to increase oil recovery (Alshakhs, 2013), therefore the study of natural brines has been well studied. A brines overview coupled with a framework on possible controls that might influence upward fluid migrations were considered.

2.1 Brines Overview

Brines are hypersaline fluids associated with hydrocarbon reservoirs and deep sedimentary basins. The brines found in deep sedimentary basins are commonly denser, older and hold high salinity (Dickey, 1969). Salinity generally increases with depth in sedimentary basins containing denser brines in the deepest parts of the basin (Dickey, 1969; Ferguson et al., 2018). Density and salinity are directly correlated and essentially caused by the wide range of dissolved solids present in brines. The brines found in deep marine sedimentary basins are frequently caused by seawater evaporation and halite precipitation (Carpenter, 1978). These brines form within the pore spaces of sedimentary rocks and their mobility is generally controlled by fluid dynamic conditions (Awadh et al., 2019). The word “brines” in terms of hydrocarbon reservoirs and sedimentary basins, are hyper-saline waters (Kharaka and Honor, 2003). They hold high amounts of dissolved salts and nearly 20% of the total volume present in the pore spaces of sedimentary basins contain salinities of 3,000 to 300,000 mg/L of total dissolved solids (Kharaka and Honor, 2003; Alcalá et al., 2008; Osborn et al., 2011). Several geological processes generally govern the chemistry

of brines. In fact, the brines chemical composition and concentration doesn't remain fixed but is variable throughout geological time. The age of brines can vary from millions to hundreds to millions of years (Gupta et al., 2012). In sedimentary basins, where regional meteoric water influx is absent, the high salinity and residence time in brines are maintained by the different mineral dissolution and fluid density, respectively (Bachu & Hitchon, 1996; Grasby & Chen, 2005; McIntosh et al., 2011; Gupta et al., 2012). Kharaka and Honor (2003), explains that the brines salinity in sedimentary basins varies within the basin itself, which in many cases limits the understanding to identify the brines origin.

Additionally, brines thought to be formed by paleo-seawater are expected to be retained since their formation has higher residence time (Spencer 1987; Walter et al., 1990; Connolly et al. 1990a; Steuber & Walter 1991), while other brines are anticipated to be shaped by dissolution of evaporate-bearing units and expected to have shorter residence time (Kharaka et al. 1987; Grasby & Chen 2005; McIntosh & Walter 2005; Hanor & McIntosh 2006, 2007). Meteoric water infiltration holding low total dissolved solids generates a wider spectrum in salinity within shallow regions of a sedimentary basin (Kharaka and Honor, 2003). In research done in Western Pennsylvania, numerous brines, in particular those from oil wells, contained only 10 to 30 percent of evaporated water, whereas 70 to 90 percent were diluted Paleozoic seawater (Dress and Rose 2010; Osborn and McIntosh, 2010). As above mentioned, the brines salinities in sedimentary basins are variable and generally caused by the mixture of different water sources or by physiochemical processes. Significant geological processes that modify the hydrochemistry of brines in hydrocarbon reservoirs and deep sedimentary basins are, among other processes, clay diagenesis, precipitation and dissolution of minerals

(Kharaka and Honor, 2003).

Diagenetic processes in sediments changes the chemistry in pore water. Diagenetic reactions, such as dolomitization and albitization of Ca-plagioclase, might explain the depletion of Mg and the enrichment of Ca in brines (Kharaka & Hanor 2003). Brines are generally formed by seawater evaporation and can exceed Cl⁻ concentrations of 300,000mg/L like those found in the Appalachian Mountains (Osborn and McIntosh, 2010). The evaporation of seawater causes depletion and enrichment of different chemical species during difference evaporation stages. The first mineral that precipitates is calcite followed by gypsum, halite and potassic salts (Carpenter, 1978 and Harraz, 2015). The formation and sequence of these minerals are controlled by climatic conditions and solubility (Harraz, 2015). In terms of dissolution, the underlying control is the solubility of existent minerals during rock-water interaction, which largely determines the concentrations of each chemical species in solution. Brines progressively become saturated with minerals that are less soluble until seawater is depleted or evaporation rate decreases. Table 2 displays the chemical concentrations during seawater evaporation and mineral precipitation at different evaporation stages, determined graphically and after Carpenter (1978) and Holland (1978)

Table 2. Stage of evaporation with progressively concentration increase in different constituents and mineral formation (Carpenter and Holland, 1978)

Stage of Evaporation	Ca	Mg	Na	K	SO4	Cl	Br
Black Sea water	233	679	5,820	192	1,460	10,340	35
Normal seawater ²	420	1,330	11,060	410	2,790	19,890	69
Gypsum precipitation begins ³	1,700	5,200	44,000	1,460	11,000	80,000	269
Gypsum visible	1,040	7,590	59,700	2,220	13,300	107,800	396
Halite precipitation begins ³	600	10,200	99,000	3,300	18,000	180,000	617
Halite visible	307	19,600	94,300	5,600	27,700	183,300	1,010
Halite	-	50,500	55,200	15,800	76,200	187,900	2,670
MgSO4 precipitation begins	-	56,100	48,200	17,700	82,200	190,500	2,970
K-salt precipitation begins	-	72,900	22,100	25,100	56,100	224,000	4,770
Potassium salts	-	92,600	8,960	54,200	54,200	254,000	6,060

Notes:

1 After Carpenter (1978).

2 After Holland (1978) at density 1.028 g/cm³.

3 Determined graphically.

Quantities are in mg/L

2.1.1 Chloride and Bromide

Elemental analyses, particularly chloride and bromide, have been used to study the origin and evolution of salinity. Since chloride and bromide concentrations are well established as a reliable and underlying tool for understanding the salinity source(s) and evolution of groundwater in sedimentary basins, both of these constituents will be the focus of this research. Considering the hydrophilic behavior and small ionic radii ($\text{Cl}^- = 1.18 \text{ \AA}$, $\text{Br}^- = 1.96 \text{ \AA}$) of chloride and bromide they become ideal conservative tracers for groundwater characterization (Custodio and Llamas, 1983; Davis et al., 1998). Both chloride and bromide are considerably unaffected by chemical reactions due to their conservative behavior until precipitation of halite or other evaporitic minerals, such as sylvite and carnallite (Banks et al. 2000; L ders et al. 2003).

Both chloride and bromide can be derived from atmospheric, precipitation, and dissolution of minerals (Davis, et al., 1998). A significant, yet minor, source of salinity in sedimentary basins is atmospheric chloride and bromide. They are transported and infiltrated into the groundwater via wind and rainfall, respectively. Additionally, their availability decreases with distance from the ocean, making it possible for atmospheric chloride to be differentiated from other chloride sources (Alcala, 2008). Dissolved chloride and bromide in groundwater hold a representative signature of the rainfall input. This allows to back-track the brines salinity source and distribution by comparing Cl/Br ratios and mixing the relationship between different end members (Alcala, 2008). The atmospheric chloride and bromide that interacted with the subsurface prior to infiltration can be identified as natural and/or anthropogenic. In a study done in England, the variation in chloride/bromide ratios was identified as seasonal and caused by street runoff. Higher and lower chloride/bromide mean ratios were found in winter and summer, respectively,

and caused by the use of salt to control icy roads and ethylene dibromide as a gasoline additive (Sollars et al., 1982).

Generally, at low temperatures, chloride and bromide are highly soluble and do not participate in ion exchange reactions, nor in the mineral face absorption (Alcala, 2008). Under extreme temperatures halite starts to precipitate and chloride is integrated in the crystal lattice while bromide remains in solution (Alcala, 2008). As halite precipitation continues to the point of sylvite and carnallite precipitation, the bromide/chloride ratio increases (Carpenter, 1978).

Rock-water interaction essentially controls the salinity in groundwater, in particular when water reacts with low solubility minerals (e.g. Halite). The salinity in brines gained from the formation and/or dissolution of minerals can be used to track the hydrochemical evolution of waters. Brines that derive from halite dissolution generally contain higher chloride/bromide molar ratios relative to seawater, whereas the brines that hold lower chloride/bromide ratios are from seawater evaporation. (Gaupp et al., 2008). A graphical Cl-Br plot was introduced by Rittenhouse (1967) to visually show that bromide behaves more conservatively than chloride during seawater evaporation (Rittenhouse 1967 and Honor, 1978). An important difference between chloride and bromide is the variation in their natural abundance. In natural fluids, chloride can be as abundant as 4×10^1 to 8×10^3 times higher as bromide (Davis, 1998). Furthermore, small changes in bromide mass would generate variation in the chloride/bromide ratios considering the chloride mass stays unchanged (Davis, 1998). A generalized and modified binary graph illustrated in figure 2 shows the seawater evaporation line relative to chloride and bromide concentrations obtained from Carpenter (1978) research.

Aside from the dissolution or precipitation of evaporite minerals, neither chloride nor bromide partakes in diagenetic reactions with carbonate, silicate or sulfide minerals (Chen et al., 2013). Therefore, chloride and bromide analysis are used to study the water origin (Worden, 1996; Kharaka & Hanor 2007) by comparing water samples with the seawater evaporation/dilution trend line. The schematic graph below (figure 3) is a modified binary graph from Carpenter (1978) research, which displays the evolutions of brines showing the relationship between the seawater evaporation trend line with different end members.

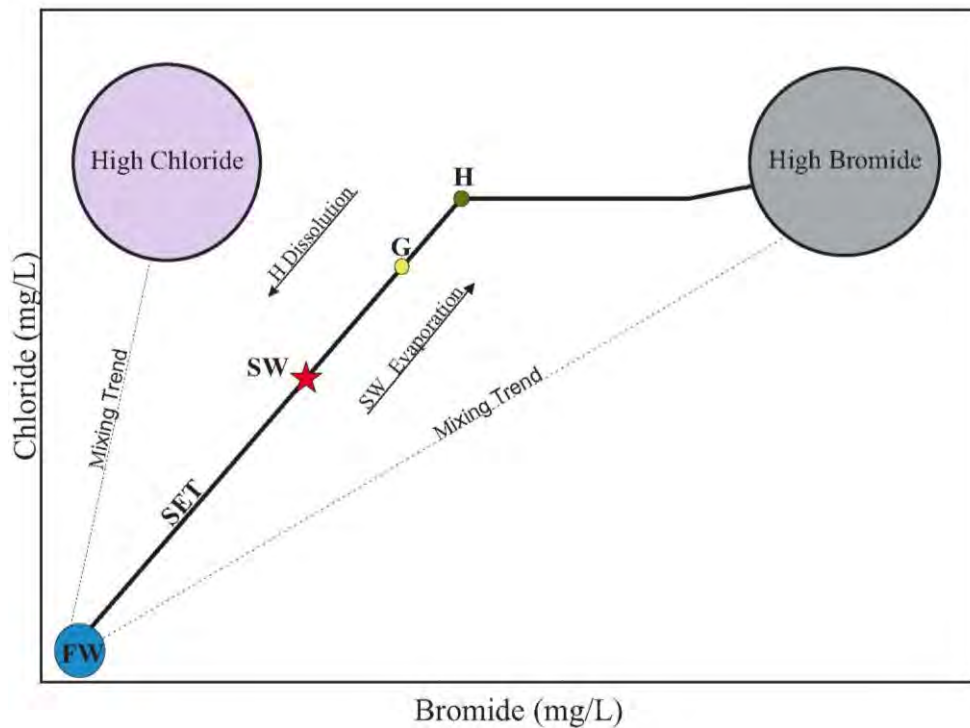


Figure 3. Modified graph from Carpenter (1978) research on Brines in Sedimentary Basins. This schematic diagram displayed possible trend between different end members. FW=Freshwater, SET=Seawater Evaporation Trend, SW=Seawater, G=Gypsum, and H=Halite.

The black line represents the seawater evaporation/dilution trend line; furthermore, each black dot along the line illustrates the point where gypsum and halite precipitate during

seawater evaporation. As seawater progressively evaporates to the point where halite is saturated, the brines become enriched in bromide. This occurs because only a small percentage of bromide is incorporated into the halite crystal lattice and, as evaporation continues, the bromide remains in the solution while the chloride bonds together with sodium to form halite (Kharaka and Hanor, 2005). Nevertheless, if the evaporation reaches 90 times that of seawater, a considerable fraction of bromide is removed from the solution (McCaffrey et al. 1987). Before halite is precipitated, chloride concentrations during evaporation increase conservatively (McCaffrey et al. 1987). The concentration of chloride becomes constant after halite formation; however, as the degree of evaporation reaches 60 times greater than that of seawater, chloride slowly begins to increase (Caffrey et al. 1987). The high chloride/ bromide ratios observed in brines are representative of halite dissolution (Carpenter, 1978). High concentrations of chloride are plotted above the evaporation/dilution trend line. Brines that have a wide spectrum of chloride/bromide concentrations are indicative of some sort of mixture with different sources of water or feasibly some type of physiochemical changes.

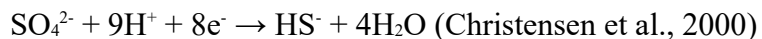
2.1.2 Cations and Anions in Brines

Other than chloride and bromide, certain cations and anions that participate in rock-water interaction in sedimentary rocks are used to characterize and evaluate the evolution of brines in sedimentary basins (Banks et al. 2000; L ders et al. 2005). The abundance of several cations and anions delineates the type of waters predominantly present in hydrocarbon reservoir and sedimentary basins. In the *Classification and Origin of Brines* from Carpenter (1978), the author shows that hydrocarbon related brines hold a considerably high amount of strontium and calcium, and depleted sulfate, relative to evaporated seawater. The abundance of strontium in brines is a result of physical and

chemical similarities with other elements. Strontium is frequently found in the mineral barite, calcite, gypsum, and anhydrite due to the replacement of barium and calcium ions in the crystal lattice (Forjanés et al., 2018). Two well-studied reactions that increase calcium while reducing magnesium and sodium are dolomitization of limestone and albitization of plagioclase feldspar (Kharaka and Honor, 2007). In dolomitization of limestone, the calcium carbonate will react with waters containing elevated magnesium forming dolomite, and consequently depleting magnesium and enriching calcium. In the case of albitization of plagioclase, which is the substitution of andesine for albite, sodium is reduced, and calcium is depleted (Kharaka and Honor, 2007).

Native sulfur can be formed by different abiotic and biotic processes, such as deeply buried sediments by thermochemical sulfate reduction (Warren, 2006), in lake sediments (Philip et al., 1994; Lindtke et al., 2011), or in shallow marine sediments (Schulz and Schulz, 2005), and on a geological timescale the native sulfur can be short-lived based on the environment (Labrado et al., 2019). Native sulfur can be reduced to sulfide; however, exposure to an oxic environment over a period of time, sulfide can be oxidized to sulfate (Labrado et al., 2019). The concentration of sulfate in seawater holds two orders of magnitude higher than freshwaters. Carpenter 1978, highlights that excess of calcium, generated by dolomitization, reacts with sulfate to form gypsum and anhydrite while reducing the amount of sulfate in brines. Sulfate reduction is the second highest reducing condition in natural groundwater systems (Miao et al., 2012). The reduction of sulfate to hydrogen sulfite is determined from the oxidation of organic carbon (Jørgensen et al., 2019). Biogeochemical reactions such as dissimilatory sulfate-reduction, triggered by a particular bacteria group (Miao et al., 2012) cause the oxidization of hydrogen sulfite and

the reduction of sulfate (Jørgensen et al., 2019). Sulfate reduction caused by the reaction with hydrogen ions is given in the general form of:



The concentrations of sulfate in natural waters can be associated with the dissolutions and oxidation of sulfate and sulfide minerals, respectively. In sedimentary rocks, in particular those that hold evaporitic minerals constitute a source for sulfate in groundwater by dissolution of gypsum and/or anhydrite and by the oxidation of pyrite (Dworkin and Land, 1996). The dissociation of sulfate minerals and the total sulfate concentrations in natural water is generally controlled by the environmental conditions (Hem, 1970). Sillen and Martell (1964, P.232-251) inferred using thermodynamic data that sulfate concentrations of ~ 1000-100mg/L will be influenced based on the amount of ionic pairs. Based on the high affinity of sulfate to form complex species such as calcium sulfate and sodium sulfate, the concentration of sulfate in solution becomes linked to those ionic pairs (Hem, 1970).

In a study conducted on brines, Kessler et al., 1995 used a systematic Na-Cl-Br approach to differentiate the sources of brines, whether they were derived from evaporation of seawater or from dissolution /recrystallization of halite. It was observed in this study that high sodium/chloride ratios were generated from halite dissolution whereas low sodium/chloride ratios were from seawater evaporation (Kessler et al., 1995), and fluids that deviated from the seawater evaporation or halite dissolution line were likely a result of water-rock interaction, in particular sodium exchange (Banks et al. 2000; L ders et al. 2005).

The presence of evaporite deposits changes the composition of surface and groundwater. Several locations in the Ventura Basin, particularly the Ojai Valley, have been shown to

have gypsum deposits and are commercially exploited. The presence of gypsum suggests that conditions may have been favorable for the growth of halite or other evaporite minerals.

2.2 Fluid Migration in Sedimentary Basin

In general, basin-scale groundwater flow is governed by topography gradient (Flewelling et al., 2014; Osborn et al., 2019), sediment compaction, buoyancy, hydrocarbon generation (Ferguson et al., 2018), density difference and fluid pressure (Bruhn et al. 2000). Field studies and quantitative basin modeling have shown large-scale fluid flow and solute transport via advection caused by fluid potential difference that move primarily through fracture zones (Ortoleva et al., 1995; Garven, 1995; Person et al., 1996; Wilson et al., 1999; Kharaka and Hanor, 2003.) Several small and large controlling factors govern the fluid mobility in sedimentary basins; nonetheless, the essential control in fluid mobility is the permeability of the sedimentary rocks (Pedersen et al., 2004). Porosity is also crucial in terms of fluid flow, particularly secondary porosity. This type of porosity includes fracture porosity, which is generated after the sedimentary rocks are formed as a result of physical and chemical processes.

Fluid mobility in sedimentary basins can be horizontal and vertical, and based on a wide range of spatial scales studies. Sedimentary basins largely contain an anisotropic permeability and their horizontal permeability commonly holds an order of magnitude or higher than vertical permeability (Desbarats 1987; Clennell et al. 1999; Flewelling et al. 2014). Recent studies have anticipated that upward migration (vertical) can be substantial with migration times up to a few days (Flewelling and Sharma, 2013). The anisotropic permeability refers to the ratio between horizontal permeability (K_h) and vertical permeability (K_v) (Shedid, 2009). These are critical controlling factors to understand fluid

mobility in sedimentary basins. It is, however, necessary to recognize spatial heterogeneity variation in horizontal layers and vertical sequences on sedimentary rocks for permeability characterization.

In terms of heterogeneities, scaling-up procedures are significantly complex due to small to intermediate scale heterogeneities (Lasseter et al. 1986). Permeability is directly correlated to heterogeneity distribution in a medium. Generally, small-scale heterogeneity implies grain-size while large-scale heterogeneity refers to geological layers, and nonetheless, the spatial scale distribution in sedimentary basins can range from rock lamination $< 0.05\text{m}$, lamination sets $0.05\text{m} - 2\text{m}$, geological beds $0.5\text{m} - 5\text{m}$, and geological sequences $5\text{m} - 100\text{m}$ or more (Wen et.al 1998). Numerous statistical and numerical studies on different spatial scales coincide on the premise that heterogeneities differences influence fluid behavior across sedimentary basins and hydrocarbon reservoirs (Lou et.al, 2017).

To fundamentally recognize fluid mobility throughout homogenous geological layers, a straightforward and simple approach in average permeability was considered. It's important to note that this approach by no means gives a substantial and definite understanding of fluid mobility in porous media, but rather, a simplified overview on fluid flow through a homogenous medium. There are many controlling factors, small and large, that govern fluid mobility in sedimentary basins, and the details of those factors are out of this scope of research.

Fluid flow is comparatively greater when only a single fluid is present in a medium, rather than if two or more fluids coexist in the same medium. In hydrocarbon reservoir, multiphase fluids coexist, and their mobility is determined by the effective permeability. Relative permeability of a rock is by definition the ratio of effective permeability of a fluid phase over the absolute permeability of the rock (Wu, 2016). Absolute permeability is

based on the steady flow of a single fluid through a medium, while effective permeability depends on the behavior of two or more coexisting fluids (Wu, 2106). Essentially, effective permeability measures the steady flow of the target fluid when the medium is saturated with one or more fluids. Derivations of Darcy's Law are used to approximate the average permeability of a system and hydraulic conductivity of fluid flow through porous rock layers that are parallel and perpendicular to each other. Equations based on absolute permeability are shown below to show how small changes affect the average permeability of a system. They are fundamentally from a fluid flow equation where a constant permeability value, a uniform pore medium, and a steady in-flow and out-flow are assumed. The equations are derived from Darcy's Law and each equation represents a different flow behavior across a geological medium.

Arithmetic-average permeability integrates linear flow in parallel layers associated with horizontal flow. It's basically the summation of every single flow rate, derived from a re-arranged Darcy's Law equation (1856):,

$$Q = \frac{K * w * h}{\mu L} (\Delta P) \quad \text{Eq. (1)}$$

Where Q is the steady rate of flow, the proportionality constant K is now the coefficient of permeability, the cross-sectional area A is now the width (w) and height (h), L is the length, μ is the fluid viscosity and ΔP the differential pressure. Equation (1) can be used to represent the fluid flow rate of a layer. The arithmetic-average permeability equation along with a schematic block diagram is shown below:

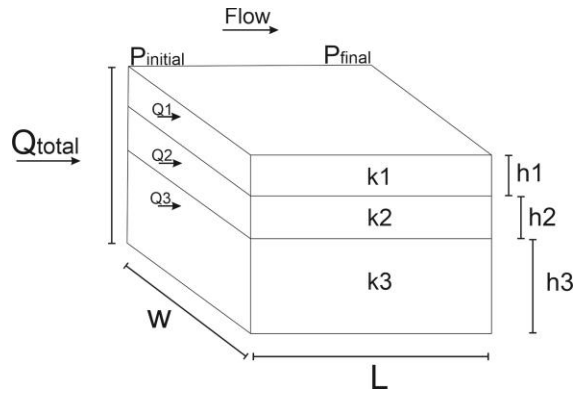


Figure 4. Modified block diagram from Fundamentals of Fluid Flow in Porous Media (Kantzas et al., 2014). The block represents the combination of three parallel rock layers.

Each layer will give a different flow rate when Darcy's Law Equation (Eq.1) is applied for each parallel layer. To obtain the arithmetic-average permeability, the total flow rate Q_{total} of the block is calculated then by substituting and rearranging, the average permeability for all three parallel layers of a homogenous block can be defined as:

$$K_{avg} = \frac{\sum_{j=1}^n k_j \cdot h_j}{h_{total}} \quad \text{Eq. (2)}$$

where K_{avg} represents the average permeability of all parallel and n indicates the number of layers

Harmonic-average permeability is related to the drop in pressure due to layers that are perpendicular to the direction of a steady flow. When a steady flow crosses the sequence of layers with different permeability, the pressure drops across each layer then the summation of all pressure drops is the total pressure of a steady flow. By setting up the pressure drop of each layer equal to the total pressure and then substituting it into a rearrange Darcy's Law Equation, the harmonic-average permeability equation along with schematic block diagram follows:

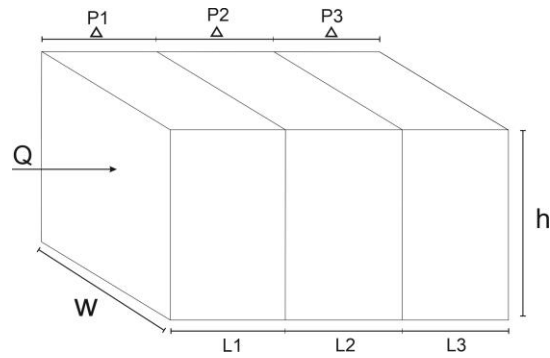


Figure 5. Modified block diagram from Fundamentals of Fluid Flow in Porous Media (Kantzas et al., 2014). The block diagram represents a linear flow across three perpendicular layers to the steady flow.

$$K_{avg} = \frac{\sum_{j=1}^n L_j}{\sum_{j=1}^n \left(\frac{L}{k}\right)_j} \quad \text{Eq. (3)}$$

where K_{avg} represents the average permeability of all parallel and n indicates the number of layers

Both approaches, mathematically listed in Equations (2) and (3), are practical for a firsthand understanding of fluid mobility across a medium that is homogeneous and isotropic, in which small changes in the layers arrangement generally influence the permeability of rock formations. It is to be expected that Wiley Canyon might have different permeability in the rock formations based on the current geological configuration of the sedimentary layers. Structural deformations on the stratigraphic succession might have enhanced or reduced the permeability of the rocks. To understand whether there is a correlation between the geology and upwelling discharging fluids, a conceptual approach on the controlling factors related to fluid mobility and a quantitative method to approximate the permeability of the rock formations in Wiley Canyon was performed.

2.3 Fractures and Permeability

Upward fluid migration from hydrocarbon reservoir to shallow water-bearing units through preferential pathways is an environmental concern. Rock fractures enhance and generate preferential pathways for fluids to migrate from depth. Fractures increase the permeability

in rocks and can be generated by tectonics, seismicity (Jacobi and Fountain, 1993, 2002; Abrams, 2005), and chemical processes. From initial work on seepages related to fractures performed by Link (1952), it showed that oil seepages occur on oil-bearing sedimentary rocks that have undergone structural deformation. There are numerous mechanisms, small and large, that induce fluid mobility in sedimentary rocks. For the purpose of this research, the emphasis is aimed on the general understanding of fractures joints and their association with fluid mobility.

Joints on rocks are created in response to stresses. Changes in the subsurface caused by dynamics stresses, such as tectonic forces, might change fracture joints opening generating preferential pathways for fluids to migrate upwards from depth. In a study done by Jacobi and Fountain (1993), direct evidence of fractures linked to natural hydrocarbons seepage was revealed from the appearance of oil seeps after an earthquake. Fault zones are surrounded by highly fractured rocks with complex geometry that induce the overall permeability distribution (Schimmelmann et al., 2018). Fault zones are composed of a fault core and a damage zone, which control the fluid flow within and near the fault zone (Caine et al., 1993). There have been correlations on the proximity of seepages to fault zones. A schematic block diagram adapted from Mitchell and Faulkner (2009) shows fracture density concentrated in the damage zone, shown in Figure 6. The damage zone contains highly dense fracture networks where permeability is likely to be higher than the surrounding photolith rock, which is the rock lacking fault-related permeability structure (Caine et al., 1993). Studies and analysis on fluid flow, showed that fractured rocks generally contain higher permeability than the surrounding non-fractured matrix rock (Berre et al., 2018)

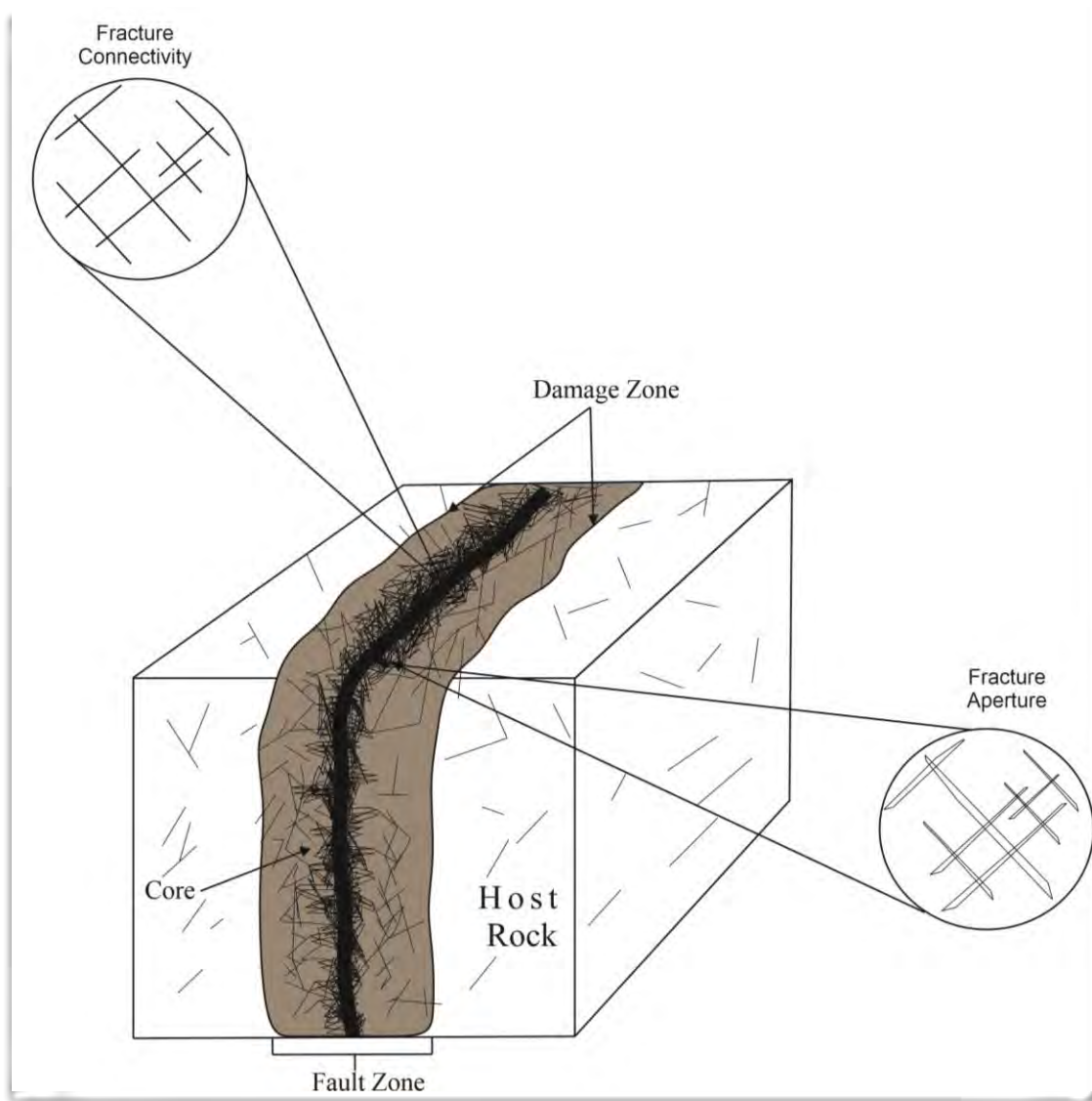


Figure 6. An illustration of a fault zone, in which includes the damage zone and core.

Understanding how fractures interact with each other and their effect on fluid mobility can be challenging. The connectivity and aperture of fracture networks likely enhance the rock permeability and would generate preferential pathways for fluids to flow. Many studies use direct and firsthand model approaches for natural fracture networks. The stochastic approach is one of those tools used for fracture simulations that can be integrated into complex numerical models for fracture connectivity and fluid flow assessment (Lei et al., 2017). Generally, stochastic models adopt fractures as straight lines and planar

disc/polygons in 2D and 3D, respectively, and then use the fractures geometrical properties as independent and random variables (Lei et al., 2017). These models are very useful for fracture simulation, which can then be applied to groundwater flow models.

Fractures act as conduits or barriers for fluids and their geometrical arrangements and connectivity are significantly important for fluid flow. High permeability zones generated by fracture connectivity, as a result of diverse fracture orientation (Maillot et al., 2017), are likely to generate preferential zones for fluid flow.

Complex fracture networks are also generated during folding events. The highest strains are likely to be near the hinge region of a fold, and it is there, where most fractures are concentrated. Fractures and fluid-rock interaction during folding have been extensively studied due to the importance of hydrocarbon migration. An example of fluid systems and fractures developments caused by an anticline fold is shown in work by Beaudoin et al. (2014). Using fracture network analysis coupled with geochemical data from calcite veins, Beaudoin et al. (2014) showed that vertical migration occurs in fractures during folding events (Beaudoin et al., 2014). In early work, Price (1966) revealed that fracture sets are expected to form on thrust related anticlines. These fracture sets can be visualized in the schematic diagram below, which illustrates region of high and low intensity fractures.

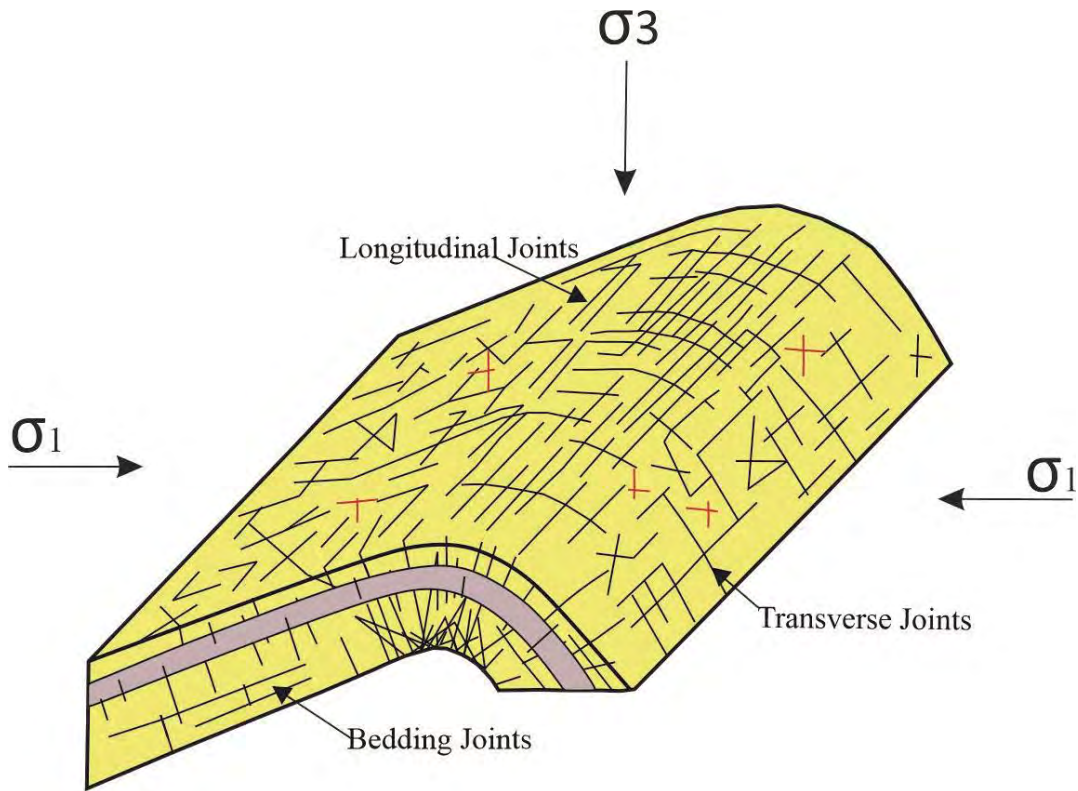


Figure 7. Schematic diagram showing different joint sets configuration during folding their relationship as well with the orientation of tectonic stresses. σ_1 = Maximum compressional stress. σ_3 = Least compressional stress.

These joints fractures sets can be classified relative to the fold hinge and bedding plane orientation. Bedding Joints are parallel to bedding and have similar strike and dip. Longitudinal Joints strike parallel to bedding and fold hinge, and dip normal to bedding. Transverse Joints strike perpendicular to bedding and fold hinge, and dip normal to bedding. Based on fracture intensity it is feasible that high permeability zones occur proximate to the axial hinge plane. Bergbauer and Pollard (2004) reported on their work done on the Emigrant Gap anticline in Wyoming that fracture intensity are 5-10 times higher in folded sandstone and shales in comparison to unfolded regions.

Fractures have been shown to be essential for storage and/or permeability, and the importance of fractures for fluid flow has been documented in Huitt, 1956 work on “*Fluid*

Flow in Simulated Fractures.” In a single fracture, the fluid flow simulation can be implied as two infinite parallel plates (Huitt, 1956 and Parsons, 1966). Figure 8 and equation 4 shows the geometrical arrangement of a parallel plate in a 3D fracture and the variables represented mathematically, respectively.

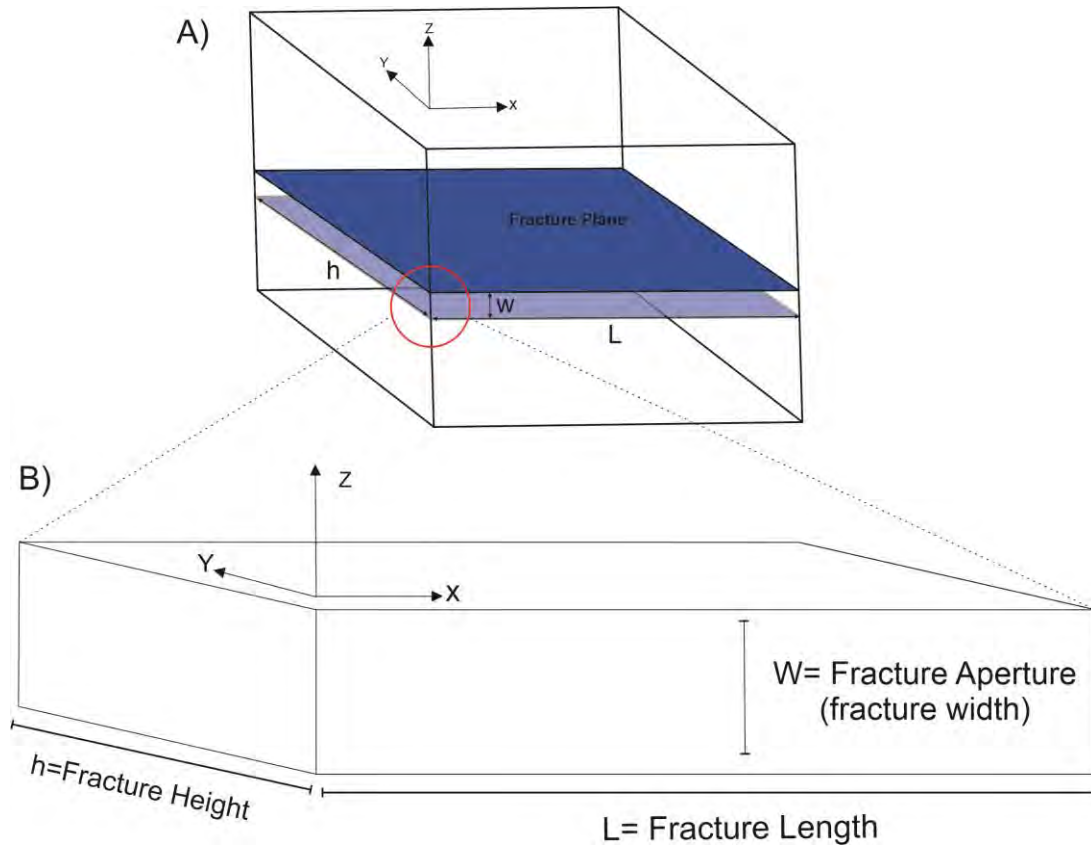


Figure 8. A) Block diagram illustrating a single fracture plane. B) Modified after Mokhtari et al., 2015 geometry of a parallel-plate 3D fracture diagram.

A forward equation that resembles a fluid flow along a single fracture adopted from the cubic law approach and after (Huitt, 1956 and Parsons, 1966) is given as:

$$q = \frac{h w^3 \Delta p}{12 \mu L} \quad \text{Eq. (4)}$$

where q is the flow rate, h is the fracture height, w represents the fracture aperture, Δp is the differential pressure in the direction of flow, which is represented usually in the x -

direction (refer to figure 8), μ is the fluid viscosity and L is the fracture length.

Fracture joints geometry are governed by how they propagates and ends, which generally is controlled by the type of rock, loading conditions and interactions with surrounding fractures (National Research Council, 1996). Equation 4 is useful in terms of fracture permeability, particularly the aperture of the fracture. The geometric arrangement of fracture joints and other controlling factors such as connectivity, density, roughness, and filling, influence the permeability of fractures. The specific details on those factors are outside of this scope of work.

Based on the theoretical model by Snow (1968, 1969) on anisotropic permeability that is centered on the parallel plate flow notion, and using the concept that fluid flow is dominant along fractures; anisotropic permeability on fractured rocks was reviewed. Fractures parallel to flow generally hold higher permeability than fractures perpendicular to flow (Lei et al., 2014). The orientation of a fracture commonly limits flow direction due to the anisotropy permeability of a fracture (Lang et al., 2018). The anisotropic permeability of a rock is when permeability varies at a given sample point with the direction of fluid flow through that sample (Meyer, 2002). The importance of an anisotropic permeability of a fractured media provides a significant understanding of the permeability of a rock formation, in particular where fractures reveal a control on fluid flow (Chen et al., 1999). The permeability of the subsurface rocks is essential for groundwater flow, storage, chemical transport, and extraction of hydrocarbons. In nature, especially in regions of high structural deformation, the subsurface rocks are generally fractured, which means the permeability will often be anisotropic. The block diagrams presented in figure 8 shows a fracture plane with an isotropic permeability throughout a single horizontal fracture, but in fact, fractures in nature are oriented in different directions

holding an anisotropic permeability in fractures. To address the permeability in fractures, numerous studies have attempted using theoretical approaches experimental approaches and numerical approaches (Chen et al. 1998). Permeability tensor is needed to model anisotropic permeability in fractures.

Based on Darcy's law, the velocity of water (v) is proportional to the hydraulic gradient (I), and the relation between both vectors should have a coefficient, which in this case is the permeability (K). Darcy's equation can be shown in vector notations as follows:

$$v_i = K I_i \quad \text{Eq. (5)}$$

According to tensor calculus rules, K is second rank tensor and can be written in 3x3 matrix. The nine components expressed in the 3x3 matrix describe the transformation of the hydraulic gradients vector (I_i) components into those of the velocity vector (v_i) (Liakopoulos, 1965). This is how Darcy's equation is related to the permeability tensor.

Mathematically the permeability tensor can be calculated similar to the stress tensor. After Chen et al., 1999 mathematical approach and solutions for random oriented fractures, a quantitative approach was modeled after Chen et al., 1999, and adapted to this research to estimate the permeability tensor of outcrops containing fractures joint sets with different orientations. The details on how the permeability tensors were obtained are explained in the methods section, chapter 5.

2.4 Potential Fluid Pathways along Abandoned Oil Wells

The proximity of groundwater to oil production fields in California has led to changes in regulations centered on concerns about groundwater quality. Failure and improper abandonment of hydrocarbon production wells can generate preferential pathways for fluids to leak into different geological strata, including water-bearing strata. The purposed goal of well abandonment is to isolate zones that might possibly leak into freshwater

aquifers and other lithological units. Abandoned wells, improperly sealed in oil-producing states, have caused contamination of groundwater, surface waters and soils (Kharaka and Dorsey, 2005). In the late 1980s, the U.S. Environmental Protection Agency (EPA) estimated that approximately 200,000 wells were not properly abandoned, particularly wells that were drilled prior to 1950 (Allison and Mandler, 2018). Proper well abandonment reduces environmental risk from fluids (oil, gas and brines) from migrating into shallow uncontaminated aquifers. In a risk analysis done on well plug failure after abandonment, Mainguy et. al, 2006 showed that the down-hole condition of the well changes after it is plugged, which reduces the plug sealing capability leading to fluid leakage. The condition of the well after abandonment can lead to microannulus formation, inducing fluid mobility along the well itself (Mainguy et. al, 2006). Furthermore, the degradation of the steel casing and cement plug decreases the integrity of the well, and potentially creates additional leakage pathways. A well casing is inserted into the borehole when the well is developed for hydrocarbon production (Celia et. al, 2005), and if the production well is later abandoned, cement plugs are placed throughout the well to isolate the hydrocarbon related fluids from shallow aquifers. Although the cement plugs have low permeability, small changes, such as micro fractures or irregularities on the cement, alters the permeability of the overall well material (Celia et. al, 2005). Figure 10 illustrates a schematic diagram of a vertical tree well with string casing with cement plugs and several possible fluid pathways. It is likely that abandoned wells would increase the probabilities of leakage over time based on many factors that affect the integrity of the well. Norsok (2013) defines the well integrity as “application of technical, operational and organizational solutions to reduce risk of uncontrolled release of formation fluids and well fluids throughout the lifecycle of a well.” A general cause that could lead to well failure is

the differential stress generated by the surrounding rock and the well void, which potentially decreases the strength of the steel casing, the cement fill and the cement plug. Other stresses applied to the well are induced by natural forces such as tectonic stresses and subsidence. The details and controlling factors affecting the well integrity are beyond the scope of this research; however, it is important to acknowledge these issues to understand possible preferential pathways for upward fluid migration.

Celia et al. (2005) described potential fluid leakage after the well has been abandoned. Figure 9 illustrated the potential pathways for fluid leakage, which are (a) between cement and outside of casing, (b) between cement plug and inside of casing, (c) through cement fill between casing and formation rock, (d) through casing, (e) in cement fractures between casing and formation rock, and (f) between cement and formation rock. These well failures after abandonment together with natural fractures likely increase the permeability of the overall rock formations.

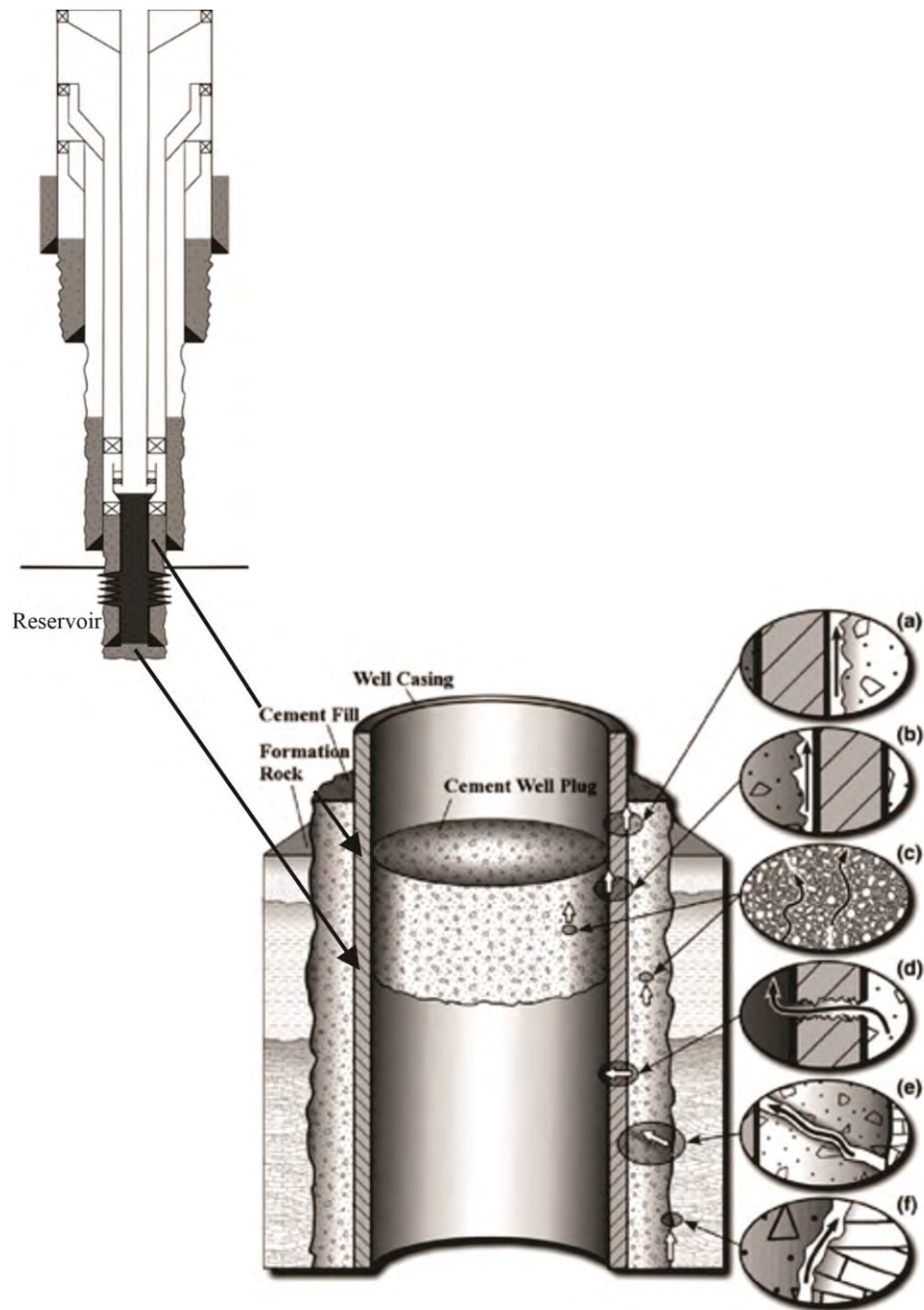


Figure 9. Schematic diagrams of an abandoned vertical well with casing strings and cement plugs between two strings, or a string of casing and formation.

CHAPTER 3: GEOLOGICAL SETTING

3.1 Regional Geology

Wiley Canyon is located in the Eastern Ventura Basin of California, on the western section of the geomorphological Transverse Range provenance (Figure 5). The western Transverse Range block was formed during the tectonic configuration of southern California (Atwater, 1998).

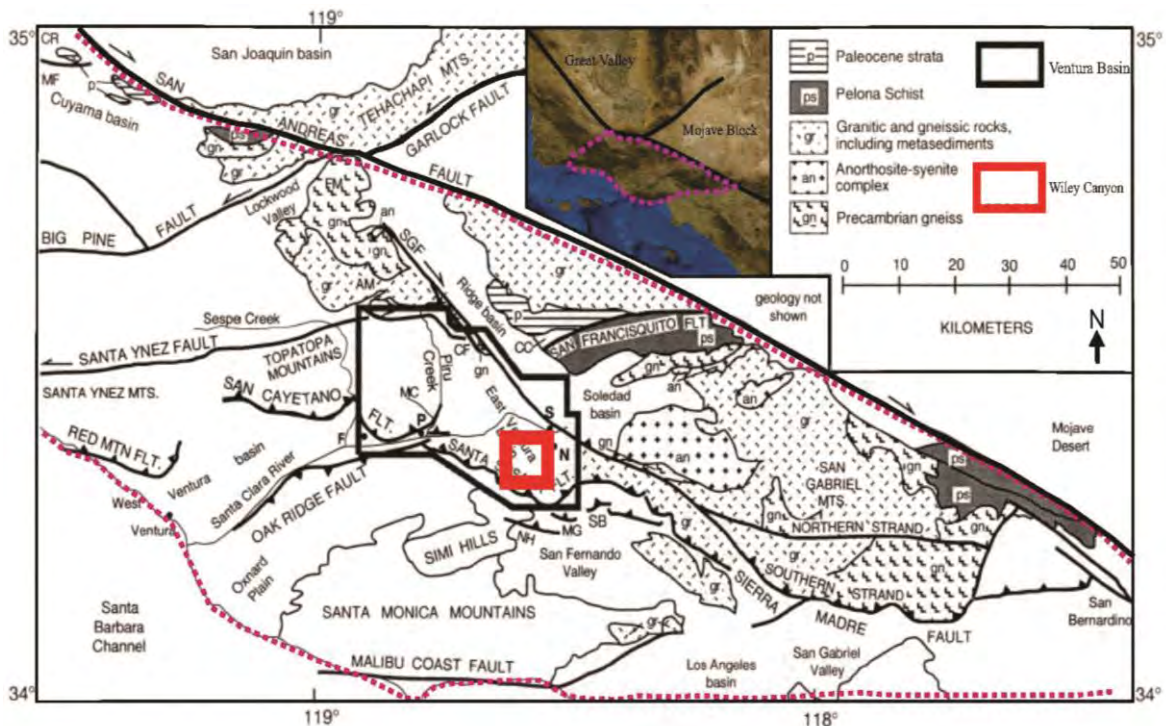


Figure 10. Modified geological map from Yeast et., al (1994) research on Late Cenozoic tectonics of the east Ventura Basin, Transverse Ranges, California. Wiley Canyon is marked as red square north of the Santa Susana Fault.

The tectonic evolution of the western Transverse Range can be described and understood by three deformational stages. Atwater, 1998, delineates the initial deformational event to have been caused by the contact of the spreading center between the Farallon and Pacific Plate against the North American Plate during the late Oligocene.

Two microplates that broke from the Farallon Plate were caught and moved along the Pacific Plate motion (Nicholson et.al, 1994). The microplate of the Monterrey Plate moved with the Pacific Plate towards the northwest, thereby shifting the plate configuration and initiating extension in the continental crust (Atwater, 1998). It has been estimated a rotation of 80°-110° clockwise was caused by the interaction of the Pacific-North America plates (Kamerling and Luyendyk, 1985). This led to a transcontinental regime in southern California that lasted nearly all of the Miocene epoch (18 to 5 Ma). Lastly, another microplate from the Farallon Plate broke down and obliquely subducted at the south end, until suddenly it changed motion and rearranged the southern California tectonic configuration into a transpressional regime. This caused the formation of the Gulf of California and initiated the San Andreas Fault system (Atwater, 1998). This deformational regime compressed the continental crust in an east-west direction shortening it through reverse faulting and folding. Today, the west Transverse Range is jammed against the “Big Bend” and has an east-west orientation tangential to the current overall orientation of many southern California Mountains

3.2 Wiley Canyon Geology Relative to the East Ventura Basin

To simplify the Transverse Range kinematics in relation to the East Ventura Basin, it is likely that the basin experienced extension and contraction behavior during the Miocene and early Pliocene, respectively. Several tectonic studies of the Eastern Ventura Basin, such as the one done by Yeats et.al (1994), describe the structural evolution of the Eastern Ventura Basin up to current day geological configuration. These structural changes have induced the generation, accumulation and distribution of hydrocarbons across the Eastern Ventura Basin. Crustal extension was the first structural event described by Yeats et.al (1994) that led to the deposition of sediments along a depression that trended southeast

across the Santa Susana Mountains. The deposition on the basin started mid-Miocene superimposing Paleogene strata, which overlays the basement crystalline metamorphic and igneous rocks (Yeats et.al, 1994).

The stratigraphic sequences of Wiley Canyon is diverse, from deep to shallow marine, and were deposited during the mid-Miocene and Pliocene. During the early Pliocene, the eastern Ventura basin underwent compression stress reactivating existing faults and forming folded strata. Furthermore, Levi and Yeast (1993) point out the uplift of the Santa Susana Mountains as a result of the upward ramping of the Santa Susana fault around 0.7-0.6 Ma (Yeast et.al 1994). Pre-existing structures can reactivate to accommodate deformational stress changes (Cruz et.al, 2015; Charrier et.al 2020; Butler et.al, 2006). It is likely that this occurred in the eastern Ventura basin as it changed from transtensional to transpressional regime. The Santa Susana Mountain uplift is feasibly an example of positive tectonic inversion, a mechanism described by Letouzey, (1990) as the reactivation of normal faults to compensate compressional deformation by reverse faulting. This brittle deformation might have formed the Oak Ridge syncline and the tightly folded asymmetrical Pico anticline. The folded asymmetrical Pico anticline is indicative of principal stress direction slightly inclined clockwise relative to the rock-bedding plane (Johnson, 2012). The northern strand of the Santa Susana Fault bounds the Pico anticline, and it is below the Pico anticline where the Modelo formation holds a hydrocarbon reservoir.

Hydrocarbon generation is commonly determined by the amount of organic matter, kerogen type, and thermal maturation proficiency present in the source rock (Al-Areed, 2018). As maturation increases in the source's rock the volume and pressure increase, and the oil and natural gas migrate into a surrounding porous rock. This movement of oil and

natural gas from the organic matter source to a reservoir rock is called primary migration. The movement of a single continuous-phase fluid through water saturated rocks or geological structures such as fracture networks and faults are called secondary migration (Schowalter, 1979).

The hydrocarbons existing in the East Ventura Basin are Miocene and early Pliocene in age (Yeats et.al, 1994) and it is likely that the hydrocarbons found in Wiley Canyon are of the same age. As for now, there hasn't been research on the age of the discharging waters found in Wiley Canyon. Near ninety-nine percent of the hydrocarbon production in the Ventura Basin is from the mid-Tertiary, in particular from the Miocene epoch (Taylor, 1976). The displacement of the Miocene hydrocarbons that exist today in the Ventura Basin occurred during the Pleistocene structural deformation, which created an ideal setting for oil migration and entrapment (Yeast, 1983).

In the initiation of natural hydrocarbons, the existing waters in sedimentary rocks are trapped with the hydrocarbons. The hydrocarbons generated in the source rocks would migrate and accumulate with the brines in a reservoir rock, which is generally porous and permeable and likely sealed by an impermeable rock or capped by a geological structure. Hydrocarbons naturally coexist with pore waters, and these waters are generally hypersaline fluids (brines). Due to the oil and gas specific gravity, oil and gas are generally found in structural highs and above dense brines (Tissot et al. 1978). The brines capability to move in a hydrocarbon reservoir can be considered by the mobility ratio of water to oil. If the mobility ratio is generally greater than one it indicates that water travels faster than oil in a porous medium. This can be described with the mobility ratio equation 5 defined below:

$$M = \frac{K'_{rw}/\mu_w}{K'_{ro}/\mu_o} \leq 1 \quad \text{Eq. (6)}$$

where;

M= Mobility Ratio

K'_{rw} = Water Relative Permeability

K'_{ro} = Oil Relative Permeability

μ_w = Water Viscosity

μ_o = Oil Viscosity

The mobility ratio is important in terms of brines mobility in hydrocarbon reservoirs and sedimentary basins because it provides an understanding of displacement and displaced fluids. In oil production fields, water injection is used to enhance oil recovery caused by displacing oil from water initial saturation state. In natural conditions, rainfall infiltration likely influences the mobility ratio to be less than one, favoring oil to be displaced.

3.3 Stratigraphic Sequence of Wiley Canyon

There are three geological units present in Wiley Canyon which are part of the sequence of the East Ventura Basin. The deposition of these units took place during the Miocene up to the late Pliocene (Yeast et al., 1994). The oldest formation present is the Modelo Formation exposed along the axis of the Pico anticline. The Modelo Formation is middle to late Miocene and is overlaid by the Towsley formation of late to early Pliocene. In some localities, the Towsley formation shows to be interfingering with the Modelo formation and at the Santa Susana Mountains is position upward into the Pico formation (Winterer and Durham, 1962). The Pico formation, of Pliocene age, grades upward and interfingers with the Saugus formation in the lower part of the Santa Susana Mountains (Winterer and Durham, 1962). A paleogeographic diagram of the Eastern Ventura basin by Winterer and Durham (1962), shows the main features of late Miocene time figure 11. South of a deep trough that trended east-west, the Oak Ridge –Simi Hills uplift generated two different depositional environments, which includes the non-marine deposits near Castaic and deep marine near Newhall (Winterer and Durham, 1962). Wiley Canyon

stratigraphic sequence are apparent to be from a marine environment, (refer to Figure 11. As the movement along the San Gabriel fault begins as early late Miocene, shallow-water deposits begin to accumulate around the Newhall area (Winterer and Durham, 1962). Shallow marine deposits are observed in both Towsley and Pico formations throughout Wiley Canyon. The shallow marine deposits observed in the Pico formation could be attributed to the structural changes that occurred during the Pliocene time. Winterer and Durham (1962) explained that the basin experienced a higher subsidence rate relative to the depositional rate, which gradually shallowed the basin creating conditions for shallow marine deposits to accumulate.

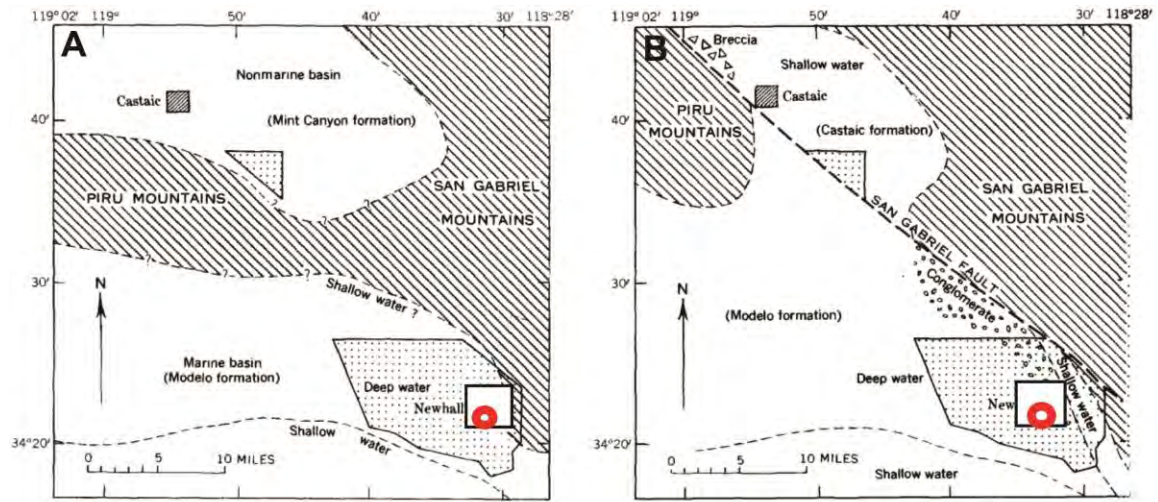


Figure 11. Modified Paleogeography of the eastern Venture basin during the Miocene time (Winterer and Durham, 1962). Figure A illustrate the geographic features of the region at the beginning of late Miocene time and before the displacement of the San Gabriel Fault (SGF). Figure B shows the features after the apparent movement of the SGF during the late Miocene time. The location of what is today Wiley Canyon can be seen in the red circle near the Newhall area.

The disposition of the stratigraphic sequence found in Wiley Canyon initiated in mid-Miocene and ended in the Pliocene. A generalized stratigraphic column (Figure 7) was generated after Yeast et al., (1994), Neogene stratigraphic column of the east Ventura basin. The Newhall sequence was used as a proxy for the Wiley canyon strata. In addition, a cross-sectional stratigraphic sequence of the overall Ventura Basin (Campbell et.al, 2014) is illustrated in Figure 8.

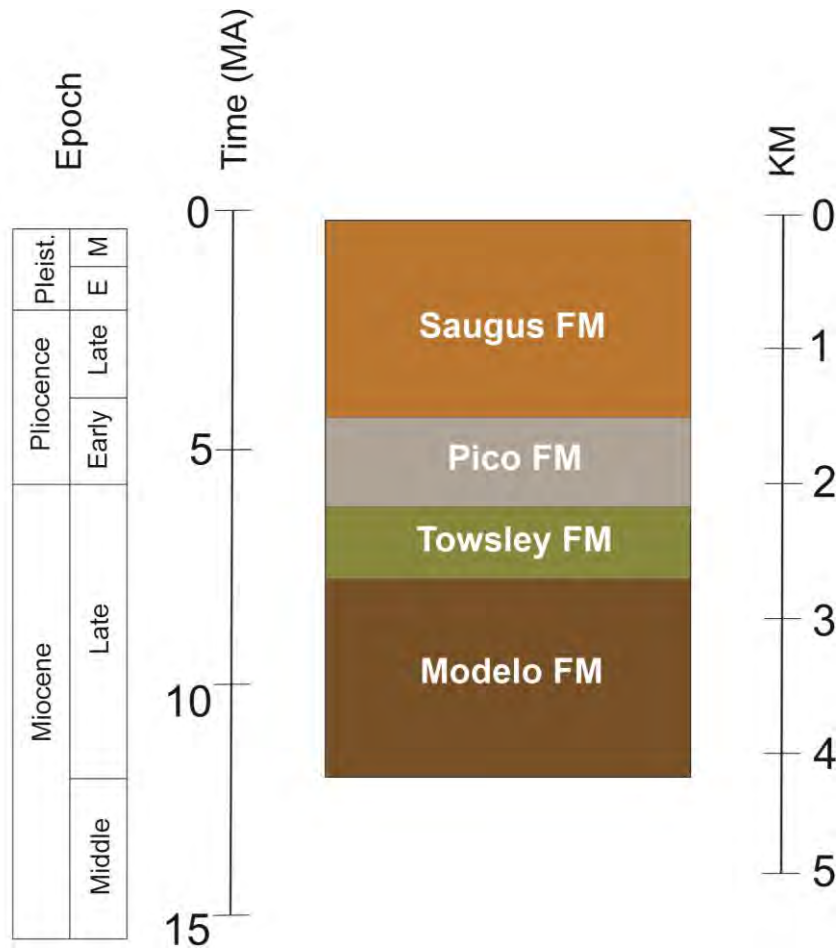


Figure 12. Modified stratigraphic column of Newhall (San Fernando Pass) from Yeast et al., (1994) Neogene stratigraphic columns of the east Ventura basin.

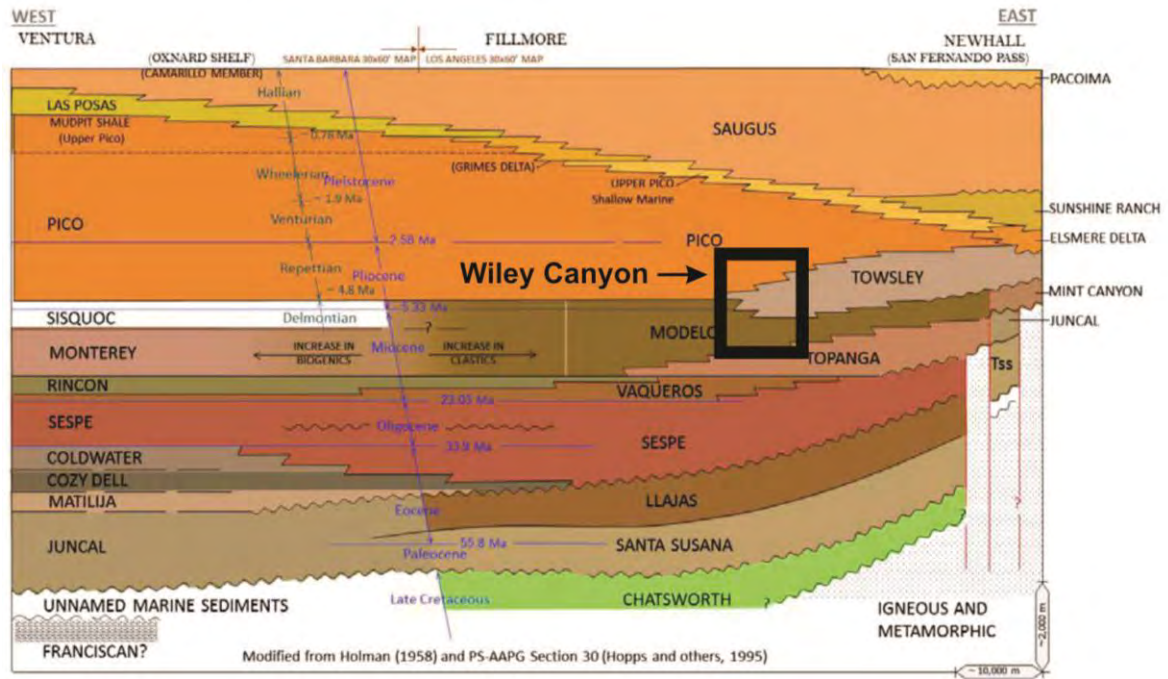


Figure 13. This is a cross-sectional overview of the lithological sequence of the Ventura Basin (Campbell et.al, 2014). The black square shows an approximation of the three formations expose in Wiley Canyon.

The geological unit description was acquired from different sources (Winterer and Durham, 1962; Dibblie, 1992; Yeast et al., 1994; Beyer et al., 2009). Numerous studies within the Los Angeles 30'x 60' quadrants have been carried out, and to avoid confusion we used the Geological map of the Oak Mountains and Canoga Park (north ½) quadrants of Dibblie, (1992) as reference and nomenclature for the geological units descriptions. The map was assembled based on field observations, former literature and geological maps. The units are described from youngest to oldest as follows:

3.3.1 Pico Formation (Early to Mid-Pliocene)

Based on observations, the Pico Formation is mostly shallow to intermediate marine based on deposits seen on exposed outcrops. The Pico Formation is made of fine-grained sandstone, silty sandstone, and platy siltstone. Inter-bedded matrix supported conglomerate with medium-grained sandstone were observed. According to Winterer and

Durham (1962) the Pico Formation can be differentiated from the underlain Towsley Formation by the Pico olive gray siltstone with limonite. The Pico Formation, on the north end of Wiley Canyon, exhibits interfingering layers of fine-grained marine deposits with the non-marine fluvial strata of the Saugus Formation. This occurrence of interfingering layers observed is generally caused by sea water fluctuation.

3.3.2 Towsley Formation (Early-Pliocene)

The Towsley Formation is well exposed and inter-fingered with the underlain Modelo Formation. Fine-grained layers of sandstone were observed that contained an arrangement of fractures in the bedding planes. Weathered shales and siltstones, and occasionally silty sandstones, intercalated with fine thin mudstone layers, were visible on well-exposed outcrops. Matrix supported conglomeratic layers were spotted in between fine-grained sandstone, and in some locations the sandstone was extremely weathered and laminated. The previous observation points to an abrupt deposition, perhaps a particular type of underground landslide or slump. Graded bedding on the fine-grained sandstone and conglomerate layers were observed, also graded beds enclosed sudden changes within their structure. We observed gypsum along fractures with interbedded layers of thin siltstones.

3.3.3 Modelo Formation (Middle Miocene Age)

We observed very thin-bedded siltstone, clay shales, and mudstones. These layers were folded, fractured and in some locations overturned. North of the Pico anticline, the bedding layers are steeply inclined to almost vertical and are extremely fractured. On the anticlinal axis, the layers are relatively horizontal and composed of fractured shales, interbedded with some fine-grained siltstone and siliceous layers. South of the anticline, silty claystone intercalated with very fine sandstones and interbedded turbidite layers were observed. Based on massively cobble and conglomerate units interbedded with fine-grained and calcareous

siltstone, these deposits are a result of submarine canyon or proximal to submarine fan deposits (Beyer et.al, 2009). The Modelo formation has been estimated to be around 3,000 feet thick on the north side of the Santa Susana Mountains (Kew, 1918). This formation acts as a hydrocarbon reservoir and potentially correlates with the Monterey oil-bearing formation (Yerkes and Campbell 1996). Obtained from the Preliminary Geologic Map of the Los Angeles 30' x 60' Quadrangle, California, Figure 6 illustrates the longitudinal cross-section of the Ventura Basin.

3.4 Pico Anticline

The primary geological structure found in Wiley Canyon is the Pico anticline. This anticline, along with the parallel Pico syncline, trends in a north-west direction with an axial plane near vertical, and it rests in the southern section of the Ventura Basin. Along the axis of the anticline, several oil-producing canyons are present. On both flanks, the beds are tilted over 40 degrees, yet the northern flank has beds that are near vertical and overturned. At the east and west ends, the anticline plunges; however, it is easier to observe at the western end due to the well exposed outcrops (Bonham, 1957). The deformation of the anticline was generated by simple flexure slip folds and most of the sandstone and conglomerate beds were deformed by laminar slip, while the sandstones and shale beds near the anticline axis were drag-folded, sheared, rotated and crumpled (Bonham, 1957).

CHAPTER 4:

METHODS

A combination of water sampling and field measurements were conducted in Wiley Canyon to address the research questions. The data collections obtained from these methods were intended to primarily test if deep fluids exist and what are the controls on fluid flow migration. Past water sample data, gathered in Towsley and Wiley Canyon from graduate Debbie Kunath (2014), were used to compare, support and enhance this research. Direct field measurements were taken on exposed outcrops to outline the distribution and orientation of fractures, and determine the fractures' relationship with water sampling locations

4.1 Water Sampling

To test if deep hydrocarbon related waters discharging in Wiley Canyon surface exist, fifty-one (51) water samples were collected from six (6) locations. The water sampling took place between late summer 2018 and spring 2019. The locations of the water samples collected are shown in figure 11. The water samples were classified as groundwater and surface water. The groundwater samples includes one oil seep (O-S-1), one water/gas seep (W-S-1) due to persistent bubbling, and three water seeps (W-S-2, W-S-3 and W-S-4). The surface samples included two water streams (W-STR-5 and W-STR-6), and they were only collected if flowing water was present. The sample locations were selected based on the water availability of the discharging waters and the proximity to geological structures and abandoned oil wells.

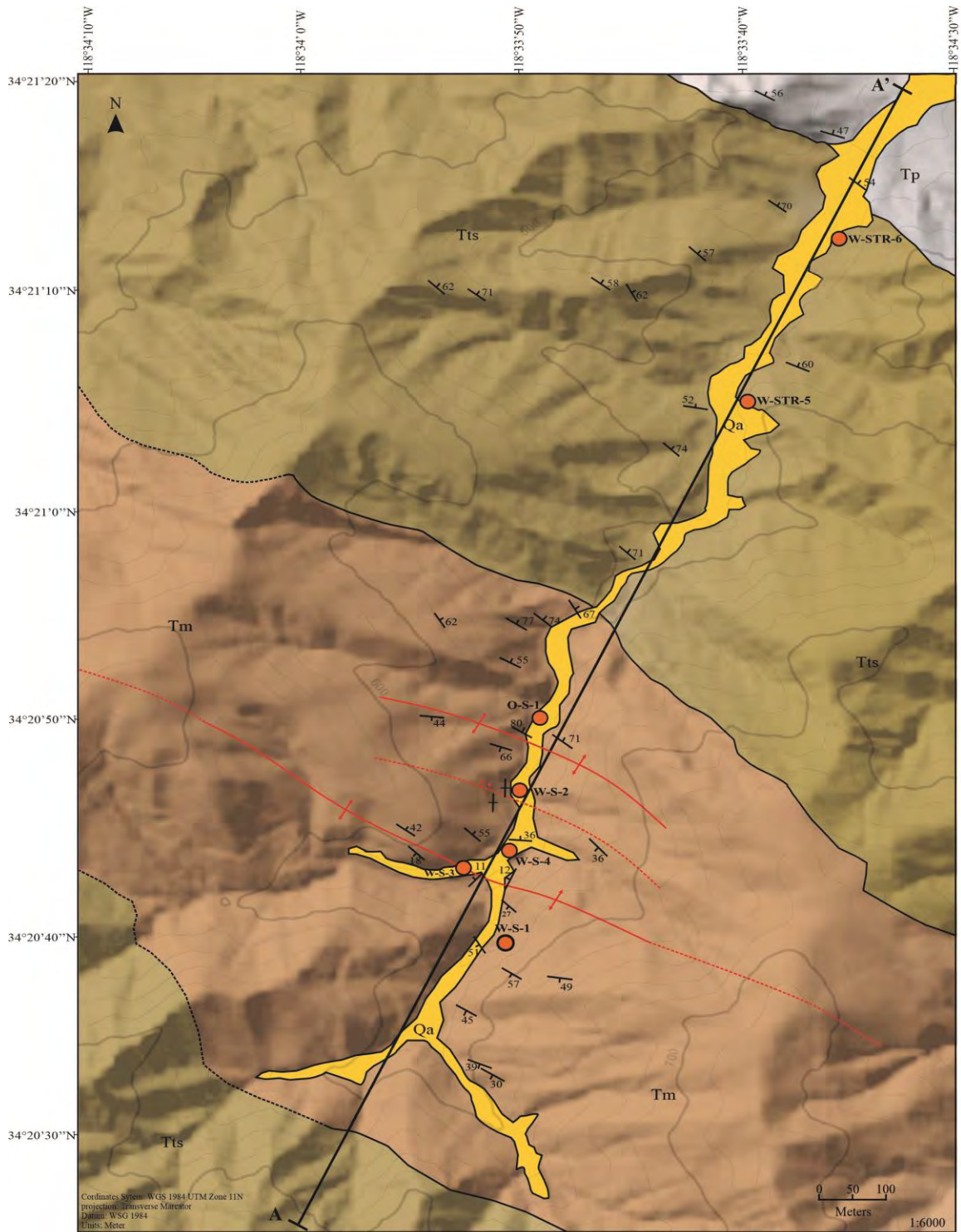



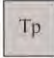








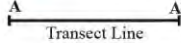


Figure 14. This geological map was developed after Bonnano (2018) geological map, to identify and correlate the proximity of sampling locations with geological structures in Wiley Canyon. The locations are illustrated as orange circles. The geological units and symbols are displayed below.

Table 3. Geological map legend

Geological Units		Age	Symbols
 Qa	Quaternary Alluvium. Unconsolidated gravel, sand and silt; light gray to light brown or reddish brown. Conglomerates gently dipping	Upper Pleistocene and Recent (USGS, 1952)	 Depositional Contact  Inferred Contact
 Tp	Pico Formation. Very-fine grain sandstone or siltstone. Conglomeritic sandstone interfingering with fine-grain sandstone. Marine with non-marine interbedded layers.	Pliocene (USGS, 1952)	 Anticline  Inferred Overturned Syncline  Inferred Anticline
 Tst	Towsley Formation. Dark brown siltstone or mudstone. Light gray siltstone and conglomerate interfingering with Pico formation.	Upper Miocene and lower Pliocene (USGS, 1952)	 Bedding  Vertical Bedding
 Tm	Modelo Formation. Dark brown siltstone and shales. Very-fine grain light gray sandstone, interfingering with lower section of Towsley formation	Upper Miocene (USGS, 1952)	 Sampling Location  Transect Line

Before collecting the water samples, the physical-chemical parameters pH and electro conductivity were measured in order to obtain a robust in-situ measurement. Two handheld device YSI EC300 and YSI pH 100A were used to measure electrical conductivity, temperature and pH, respectively.

In every sampling location, the water samples were collected differently. When sampling from oil seep (O-S-1), the oil slick was displaced using a tree branch while the oil and water bubbled and quickly the field physical-chemical parameters were measured. A waiting period was held until the YSI stabilized before the final reading was recorded. After the parameters were measured, a pre-cleaned, 2-liter, high-density polyethylene (HDPE) bucket was used to collect the water sample and then it was poured into a pre-cleaned 100 ml HDPE bottle via a plastic funnel. Sampling location W-S-1 was unique due to the constant and violent bubbling, which is likely to be source of methane. The parameters were first taken directly from the bubbling hole and then, using the same sampling technique as O-S-1, but without removing the oil slick, the water sample was collected. In location W-S-2, the water was slowly seeping out of the ground. To competently take a sample from W-S-2, a small pool was generated by pressing on to the

soil and then, with a 30 ml syringe, the water was extracted and poured into the HDPE bucket. The parameters were measured from the bucket before transferring the water into a pre-cleaned 100 ml HDPE bottle. Locations W-S-3 and W-S-4 were sampled similar to location W-S-2. Sampling locations W-STR-5 and W-STR-6 were directly sampled from a running stream. The waters from both of these locations were collected with the HDPE bucket, then the parameters were measured directly from the bucket and recorded, and finally the waters were transferred to a pre-cleaned 100 ml HDPE bottle. Figure 11 illustrates the three sampling locations O-S-1, W-S-1 and W-S-2, and a close-up from where W-S-2 samples were collected.

All water samples collected were stored in a cooler with ice and kept cold until arrival at the Cal Poly Pomona hydrogeological laboratory. To avoid any dilemma on the holding period of the samples, each water sample collected was held for twelve hours to allow suspended solids to settle. Once the sediments settled, a vacuum filtration technique was used to filter the sample. This filtration procedure was necessary due to the heavy oil globules and large sediment particles in the water samples. After the first filtration, a 30-ml syringe attached with a $0.45\mu\text{m}$ Millex filter was used to re-filter the water samples into three pre-cleaned 30-mL HDPE bottles to test for alkalinity, anions and cations. A 2% optima grade nitric acid was added into the cations 30-mL bottles for preservation. After the three bottles were filtered, they were placed in the refrigerator with a constant temperature of 5°C to 10°C to avoid any temperature fluctuation.

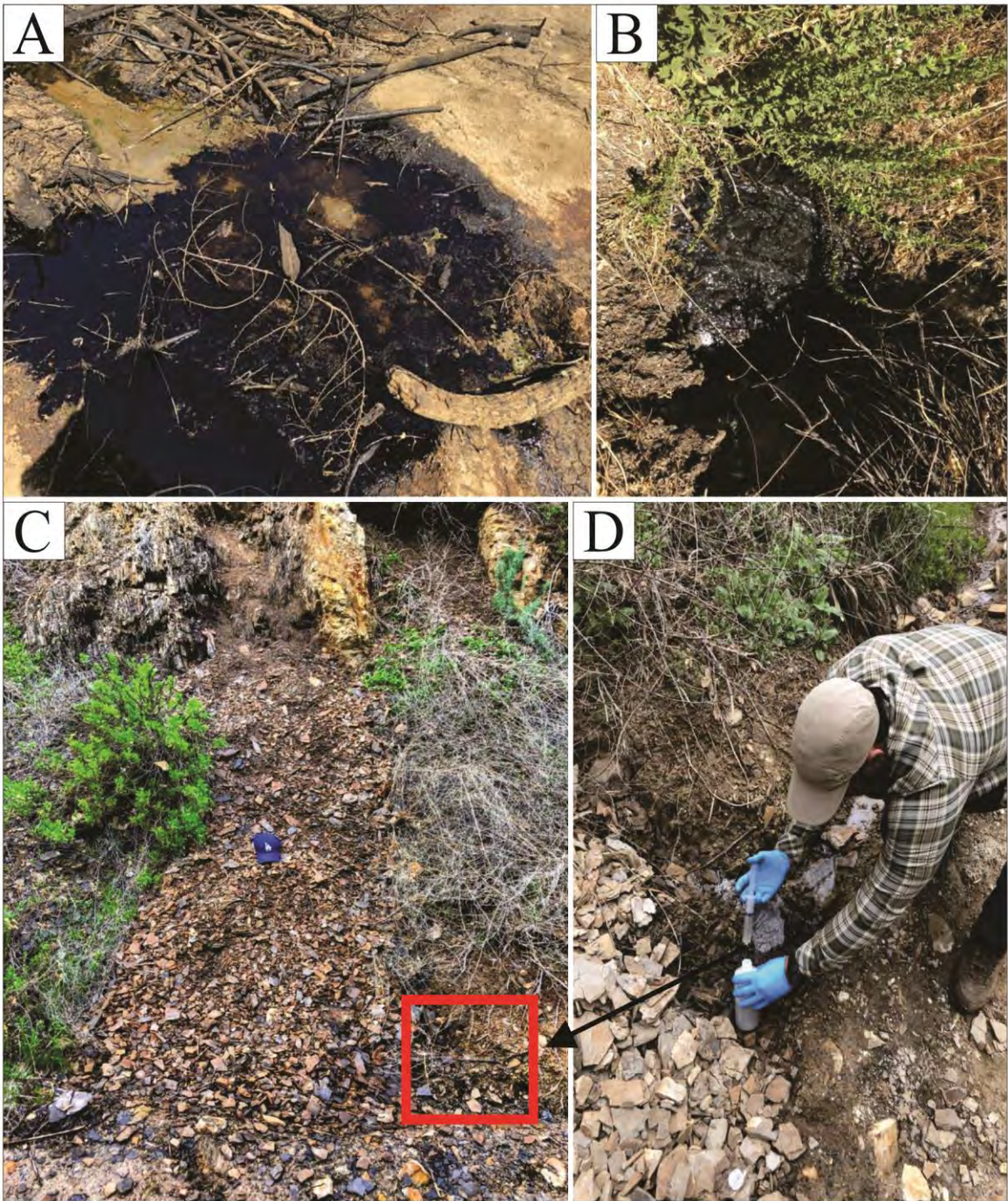


Figure 15. A) Location O-S-1, where oil/gas and water are sporadic bubbling. B) Location W-S-1, where water is constantly and violently bubbling. C) Location W-S-2, where rocks are highly deformed and folded. D) Is a close-up of location W-S-2 as water was being sampled directly from the water pool generated by pushing down into the soil and letting water seep out of the soil. A strong rotten egg odor was sensed in location W-S-2.

4.2 Laboratory Procedure

The alkalinity was analyzed in the Hydrogeological Laboratory at California Polytechnic State University, Pomona. Within 24 hours of sampling and proper filtration, the alkalinity was measured using the potentiometric titration technique after Gran-Alk titration method (Gieskes and Rogers, 1973). Alkalinity is defined as the capacity of water to neutralize acids and bases while maintaining a stable pH level (USGS, 2020). The probe used for titration was calibrated using a buffer solution of known pH. After every titrated sample, the pH probe was cleaned with deionized water to avoid any cross contamination between water samples. Hydrochloric acid (HCl) 0.1 N standard solution was used as the neutralizer. Given the alkalinity of many aqueous systems that are predominately controlled by carbonate solutes (Rounds et al., 2001), the alkalinity of the water samples collected were calculated as Calcium Carbonate (CaCO₃) concentration using the equation 7:

$$\text{Alkalinity} = \frac{(\text{mL HCL}) (0.1\text{HCl Normality}) (50,00\text{mg CaCO}_3)}{(\text{mL of sample})}$$

In natural waters, carbonate alkalinity is the most common water alkalinity due to the dissolution of minerals present in carbonate rocks. Subsequently, the hardness of water is associated to the amount of CaCO₃ present in water. Table 4 shows the water harness based on the concentration of CaCO₃.

Table 4. Modified table of water harness from the USGS Water Science School (2020)

Water Harness as CaCO ₃ (mg/L)	
Classification	Concentration (mg/L)
Soft	0-60
Moderately Hard	60-120
Hard	120-180
Very Hard	>180

A Thermo Scientific Dionex Ion Chromatography (IC) system was used to measure anions concentration in ppm (precision $\pm 1\%$). The tested anions included fluoride, chloride, bromide, nitrate, and sulfate. The calibration standards preparation was generated with known detection levels and used for calibration. Nearly 70% of all water samples that were analyzed were diluted after the first IC run due to the high chloride and sulfate concentrations that ran above standard concentrations. High anion concentration peaks generally overlapped with lower anion concentration peaks giving misleading results; in that case the dilution of high anion concentrations were necessary to avoid inaccurate readings. The diluted samples were re-analyzed; however, only the result from which the water sample was diluted by was used. If the sample was diluted by chloride then strictly, and only, chloride concentration was used. The analytical results obtained from the water samples collected together with Kunath (2014) results from Wiley and Towsley canyons were cautiously used to generate binary graphs. The samples collected for cations/metals analyses weren't measured due to Covid-19 precautions as the research came to an end.

4.3 Geological Measurements

During October 2019 through December 2020 structural measurements were collected in Wiley Canyon. These measurements consisted of strike and dip on bedding planes and joint fractures on numerous outcrops. A Garmin handheld Global Positioning System (GPS) with assigned UTM coordinates was used to obtain accurate locations on every point measured. The bedding plane measurements are displayed in the appendix and plotted in the modified and simplified geological map shown in figure 9. The importance of adding a structural assessment into this research was to recognize possible avenues for fluid migration.

The structural measurements were taken using a Brunton compass and converted from quadrant notation to an azimuth notation. The fracture joints measured were classified based on their orientation relative to the bedding plane and were grouped as bedding fractures, longitudinal fractures and transverse fractures. A total of 37 and 180 points were measured on bedding planes and fracture joints, respectively. The orientation and dip direction of fracture joints were obtained directly from well-exposed outcrops; conversely, some dip directions in the fractures were difficult to measure, so a line of intersection of two different plane surfaces was measured, and then a stereographic projection program was used to obtain the plane containing those two lines.

Stereonet projections were made using the program Stereonet 11 (Allmendinger, 2016) to visually represent the bedding planes and fracture joints orientation. These stereographic projections were used to detect cluster patterns and fracture density distribution. Rose diagrams were developed using the same program and shows in two dimensions the spatial distribution and frequency of fracture joints. These circular histograms are used as directional data distribution and calculated by counting data points within a given degree bin. The bin can be fixed at different degrees. For example, if the degree bin is set at 20, the data points would be counted within 20-degrees, and the radial distance from the center of the stereonet is assigned as the frequency of data points that occurs with-in the 20-degree bin. Finally, the data points are normalized and converted into percent frequency of the total and displayed as rose pedal. Additionally, the measured data was contoured to illustrate the density patterns using the 1% area method. This approach was useful to visually represent and interpret the density distribution of the fracture joints. The data is plotted as poles in an equal-area stereonet where the contours are generated by calculating the poles density within $1/10^{\text{th}}$ radius of the stereonet.

The geometric arrangement and fracture patterns on joint fractures have been related to groundwater flow; similarly, the distribution of the high-angle fractures has been linked to vertical connectivity (DesRoches et al., 2014). Five outcrops were used to measure the fracture joints. The outcrops were chosen based on their proximity from the seep/springs and accessibility to take measurements. One of the outcrops was located in the Towsley formation, while the remaining four were located in the Modelo formation. To avoid bias on the measurements' density and frequency, the fracture joints measurements on each outcrop were constrained within a 5 square meter area. The measurements and outcrop locations are shown in appendix and plate, respectively.

The purpose of obtaining joint fracture measurements was to integrate them into a quantitative analysis to recognize possible controls on upward fluid migration. Fractures generally produce high permeability in the direction of the fracture (Li et al. 2009), and the coefficient of permeability in fractures is influenced by the orientation of the fractures (Hsieh et al 1985; Li et al. 2009). A mathematical approach was used to obtain the permeability tensor after Chen et al. 1996, analytical solution on arbitrary oriented fractures. The permeability tensor is commonly used to exemplify the anisotropic properties of a fractured medium (Lang et al. 2014). The permeability tensor K is the symmetric second rank tensor and shown as:

$$K = \begin{bmatrix} K_{xx} & K_{xy} & K_{xz} \\ K_{yx} & K_{yy} & K_{yz} \\ K_{zx} & K_{zy} & K_{zz} \end{bmatrix} \quad \text{Eq.(8)}$$

where K 's are components that link the flux and pressure gradients along the x, y, and z axes in the 3D Cartesian coordinate system, the principal permeabilities are related to the direction of the eigenvectors, and the eigenvalues represent the magnitude of the corresponding eigenvector (Lang et al., 2014).

Using the Chen et al. 1996 method to obtain the permeability tensor of a single set of parallel fractures, equation 9 was adopted to calculate the permeability tensor for each joint fracture set. The authors, Chen and others, considered the inclined fractures to be within a representative elementary volume (REV), in where the REV arrangement is related to the fractures spacing and orientation (Chen et al. 1996). The permeability tensor is a second order tensor can be treated as a stress tensor where the principal stress directions (eigenvectors) would represent the direction of the maximum and minimum permeability. The permeability tensor is estimated and expressed as a 3 by 3 matrix with the eigenvalues being an approximation (magnitude) of the permeability along the fractures.

$$[k_{ij}] = \frac{b^3}{12d} \begin{bmatrix} (n_2)^2 + (n_3)^2 & -n_1n_2 & -n_3n_1 \\ -n_1n_2 & (n_3)^2 + (n_1)^2 & -n_1n_2 \\ -n_3n_1 & -n_2n_3 & (n_1)^2 + (n_2)^2 \end{bmatrix} \quad \text{Eq. (9)}$$

Chen et al. 1996

where K_{ij} is the permeability tensor, b fracture aperture, d fracture spacing, and n_1, n_2 and n_3 are the components of the unit vector in the directions x, y and z , respectively.

The vector components of the unit vector shown in the 3x3 matrix represent the directional cosines from trend (t) and plunge (p) of poles to fracture planes because lines (poles) are vectors, and the direction of a line is represented by the directional cosine, where $n_1 = \cos(p) \sin(t)$, $n_2 = \cos(p) \cos(t)$, and $n_3 = -\sin(p)$. The average mean vector of the poles to planes of the joint fractures measured was obtained using stereonet 11 (Allmendinger, 2016), which is computed using Fisher mean vector statistical analysis (Fisher et al. 1987). The aperture and spacing of each fracture were measured using an mm ruler and tape measure, respectively. A portable, digital microscope with magnification up to 100x and 1080p resolution of digital image was used to measure and capture fracture aperture for fractures that were difficult to measure and see with the naked eye. The strike

and dip of each joint fracture were measured in a quadrant notation, but then converted into an azimuth notation and plotted in Stereonet 11. The permeability tensor calculations for each outcrop are shown in the appendix.

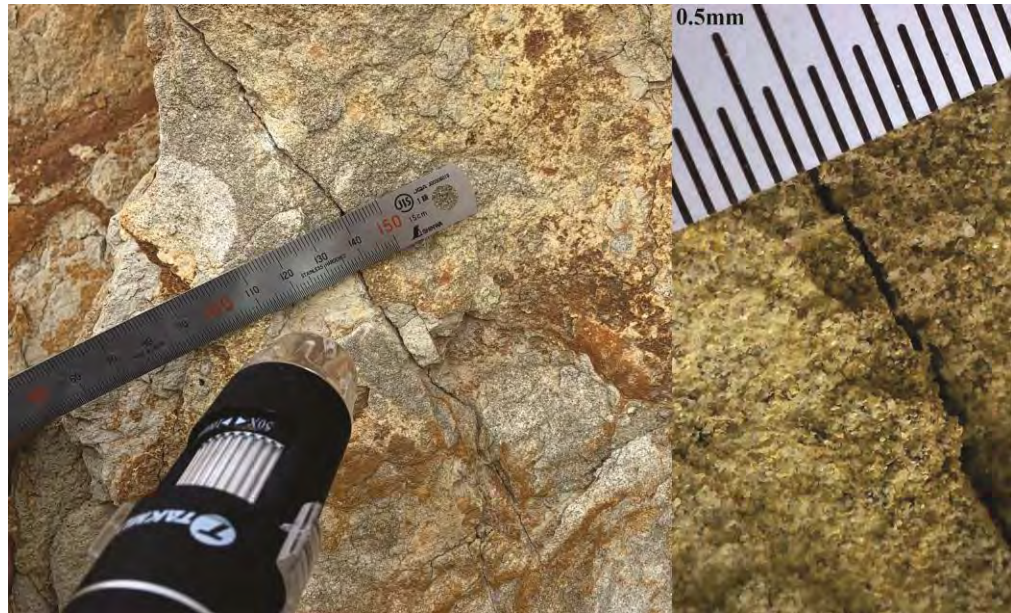


Figure 16. Aperture measurement in a transverse fracture on fine-grained sandstone of the Modelo formation using a portable microscope. The aperture was approximate 0.3mm.

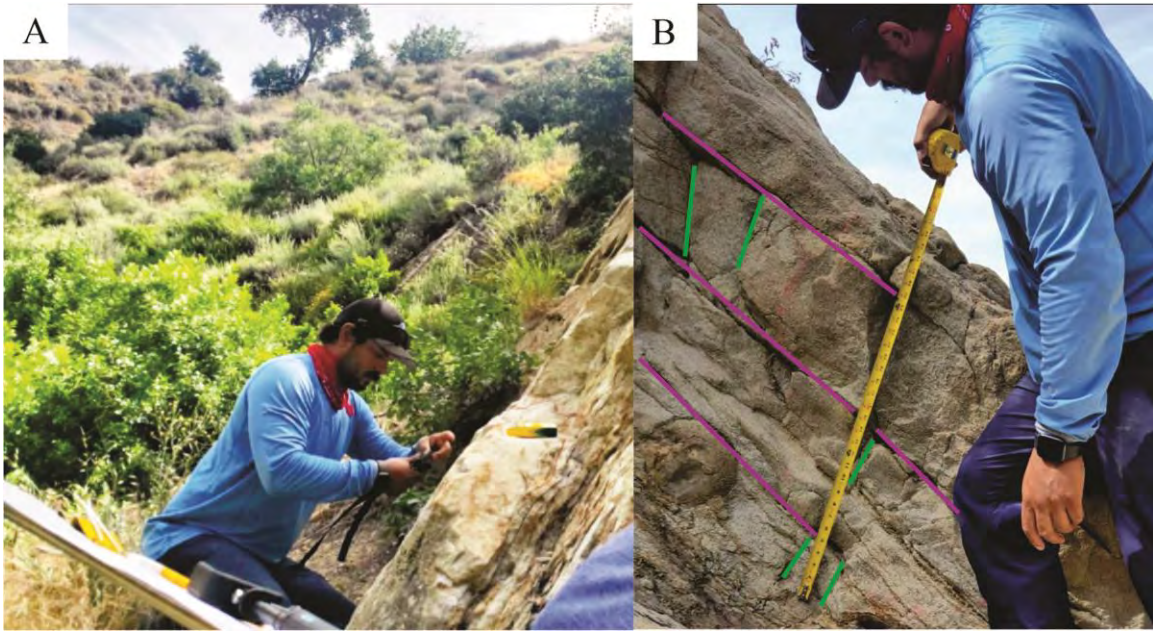


Figure 17. Field measurements on outcrops. Photograph A illustrates the strike and dip measurements on a fine-grained sandstone bed of the Modelo formation. Photograph B illustrates spacing measurements between bedding fractures on a sandstone outcrop of the Modelo formation. The purple and green lines represent the bedding and longitudinal fractures, respectively.

Once the permeability tensor was calculated using equation 9 on a single set of parallel fracture joints, the permeability tensor on every outcrop was added using matrix addition. In every outcrop, the permeability tensor was calculated for each joint set using equation 9. The eigenvalues and eigenvectors from the sum of all tensors by site were calculated using dcode.fr/matrix-eigenvectors, where λ is the eigenvalue with its corresponding eigenvector.

$$\lambda_1, \text{yield an eigenvector } \begin{bmatrix} E \\ N \\ Z \end{bmatrix} = \begin{bmatrix} \text{Value Component 1} \\ \text{Value Component 2} \\ \text{Value Component 3} \end{bmatrix}$$

$$\lambda_2, \text{yield an eigenvector } \begin{bmatrix} E \\ N \\ Z \end{bmatrix} = \begin{bmatrix} \text{Value Component 1} \\ \text{Value Component 2} \\ \text{Value Component 3} \end{bmatrix}$$

$$\lambda_3, \text{yield an eigenvector } \begin{bmatrix} E \\ N \\ Z \end{bmatrix} = \begin{bmatrix} \text{Value Component 1} \\ \text{Value Component 2} \\ \text{Value Component 3} \end{bmatrix}$$

The eigenvector components (E, N and Z) are in directional cosine and are illustrated below.

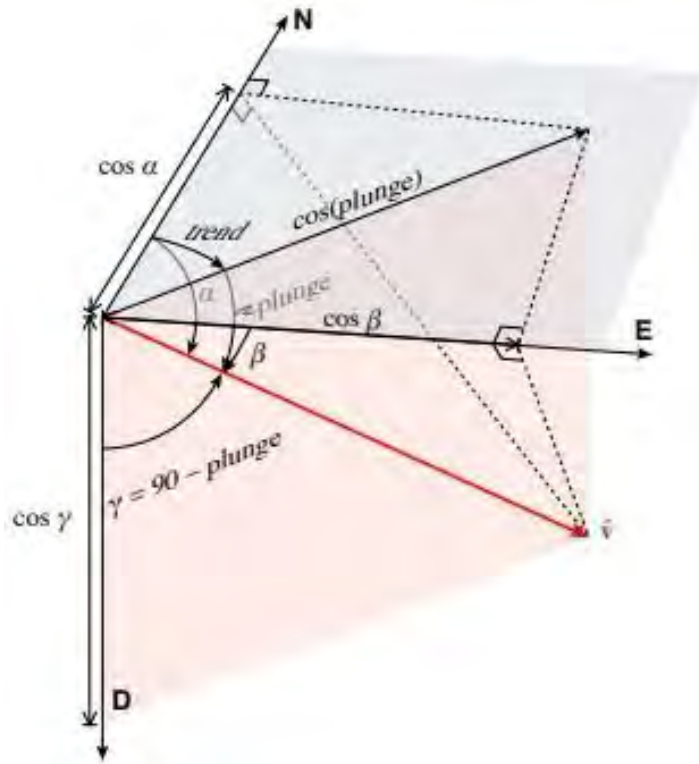


Figure 19. Illustration of the axis together with the angles of directional cosine (Allmendiger, 2015-16)

Table 5. Orientation of a vector by directional cosine (Allmendiger, 2015-16)

Axis	Directional Cosine	Poles
East	$\cos\beta$	$\sin(\text{trend})\cos(\text{plunge})$
North	$\cos\alpha$	$\cos(\text{trend})\cos(\text{plunge})$
Down	$\cos\gamma$	$\sin(\text{plunge})$

The orientation of a line (vector) is represented by directional cosine. The eigenvector components, which are represented as directional cosine were converted into trend and plunge and plotted in Cartesian coordinates. Refer to appendix for details on the calculation procedure.

CHAPTER 5:

RESULTS

Our field and laboratory results from the water samples and geological measurements are shown in tables 4 and 5. The results include water field parameters, laboratory analytical results and fracture measurements. The data allowed the generation of numerous figures to graphically illustrate the results and provide a comprehensive understanding to address our research questions. The results are divided into three (3) sections: 1) physiochemical parameters, 2) water analytical analysis and 3) geological measurements. The physiochemical parameters and analytical results are based on the water samples collected and the geological measurements that were centered on bedding planes and fracture joints measurements.

5.1 Physiochemical Parameters

The field parameters collected in the water samples included temperature, pH and electro conductivity (EC). The alkalinity and total dissolve solid (TDS) were calculated in the laboratory. The physiochemical results are shown in Appendix B . The water samples ranged from 9.3 °C to 31.2 °C with sample O-S-1 holding the highest temperature of 31.2 °C. The EC was variable across all water samples and fluctuated according to the time of year. The highest EC reading was observed in sample O-S-1 with 12.15 millisemens per centimeter (mS/cm) at temperature of 25.5 °C. The overall EC ranged from 0.001 mS/cm to 12.15 mS/cm. The pH ranged from 7.15 to 8.67 with the highest pH reading of 8.47 in sample O-S-1. The average measured pH was 8.14 ± 0.03 .

The alkalinity was calculated using formula 2 and obtained in mg/L, but then converted in to meq/ L, which is the preferred method for water quality analysis. The alkalinity estimated average was 52.5 ± 4.6 meq/L with the highest observed value of 114.02 meq/L

in sample W-S-2. The total dissolved solid (TDS) was calculated using the EC obtained from our field measurements and a conversion factor of 0.64 provided by the U.S salinity laboratory staff (1958). This conversion factor between EC and TDS is generally used in waters that are predominantly rich in chloride (Evangelou, 1998), and for an approximation of TDS in natural waters. EC and TDS share a direct proportionality due to the dissolved ions present in natural waters. The formula used was $TDS = (0.64) (EC)$. The calculated TDS ranged between 1.6 and 7776 part per million (ppm).

5.2 Analytical Results

The water samples collected were analyzed for five (5) anions fluoride, chloride nitrate, bromide and sulfate. The results are presented in Appendix C. The concentrations of fluoride ranged between 0.14 mg/L and 3.61 mg/L with the highest average of 2.20 mg/L found in samples O-S-1. Chloride concentrations ranged between 18.12 mg/L and 8983.2 mg/L. The highest chloride concentrations were observed in location W-S-2 with an average of 6096.54 mg/L. Nitrate concentration ranged between 0.22 mg/L and 47.91 mg/L with the highest average observed in location W-S-2 of 30.38 mg/L. Bromide wasn't detected in six (6) out of fifty (50) water samples analyzed. The concentrations of bromide ranged between not detected and 42.60 mg/L with the highest average observed in location W-S-2 of 7.36 mg/L. Sulfate concentrations ranged between 7.77 mg/L and 2956.95 mg/L with the highest average observed in location W-STR-5 of 1988.36 mg/L. Rainwater was analyzed and had detections of 0.781 mg/L of chloride, 0.42 mg/L of nitrate, 1.26 mg/L of sulfate and no detection of fluoride and bromide. The overall concentrations of chloride in all sample locations decreased after several rainfall events while the remaining anions concentrations fluctuated after the first rain event.

5.3 Geological Measurements

A simplified and modified geological map (Plate 1) at scale of 1:6000 and a schematic cross-section (Plate 2) were constructed, and both were compared to Dibbles's 1991 geological map. The bulk of the field measurements were obtained from the northern limb of the Pico anticline. The outcrops used for the joint fracture measurements were located in the northern limb. The average bedding orientation was 287.2° with an average dip of 69.2 to the north-east in the northern limb and a dip of 22.4° to the south-west in the southern limb. The fold axis had a trend of 305.8° and plunge of 7.9° . Stereographic projections of the bedding planes and poles to bedding are illustrated in Figure 20. These measurements show the bedding planes to dip steeper in the northern limb than the bedding planes in the southern limb.

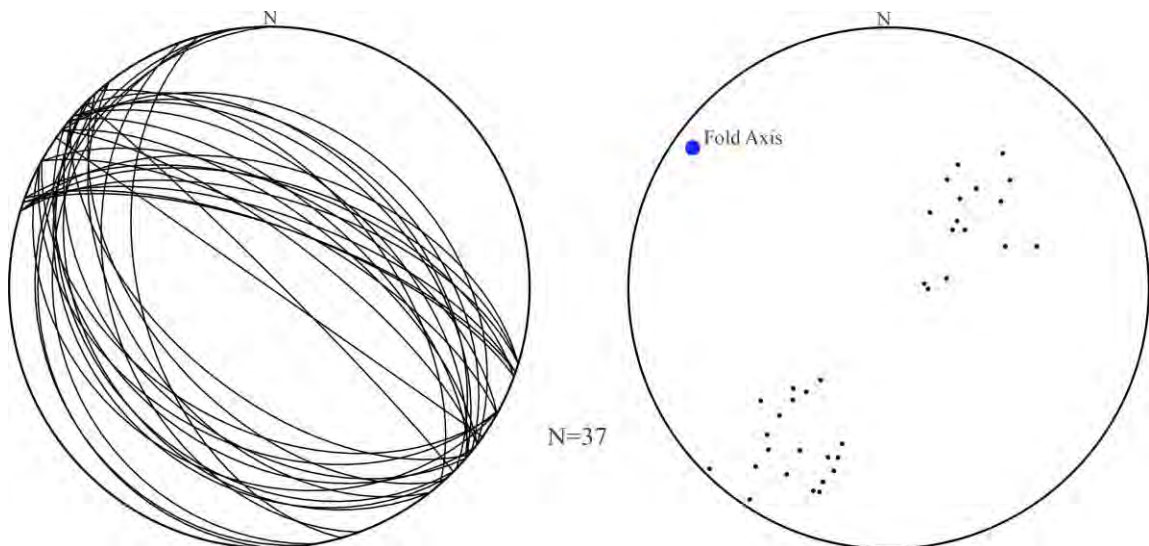


Figure 19. The right stereonet shows the bedding planes of the northern and southern limbs from broadly distributed outcrops. The left stereonet shows the poles to planes and the fold axis of the Pico anticline

The dominant structure in Wiley Canyon is the Pico anticline with an overall trend towards the NW and nearly horizontal beddings near the anticline axis. Approximate 200

meters north of the anticline axis, near sampling location W-S-2, kink fold seems to be present based on the cataclastic deformation, orientation of bedding and fluid seepage observed; although no displacement was measured, field observations point towards some highly brittle deformation zone. Minor antiform folds in the shales and siltstones are present near the anticline axis in the northern flank, and it appears to be the highest deformation zone.

The rose diagrams were generated from the poles to fracture planes and set for a full 360-degree rose with bin size of 20° and 50% of total perimeter of the circle. Based on the rose diagrams for all the joint fractures measured in the five outcrops, the bedding joint fracture set had a mean vector of $228.9^{\circ} \pm 10.4^{\circ}$ with a maximum value of 26.3 % between 221° and 230° . The poles cluster showed three distinct patterns indicating three different dip directions. The first cluster dips towards the northeast with an average dip of 71° , a second cluster dips towards the southwest with an average dip of 68.5° and the third cluster dips towards the west-northwest with an average dip of 12.3° . The longitudinal joint fracture set had a mean value vector of $46.8^{\circ} \pm 16.8^{\circ}$ with a maximum value of 20 % between 41° and 50° . The longitudinal fracture poles also showed three distinct clusters. The first cluster dips towards the southwest with an average dip of 19.3° , a second cluster dips towards the northeast with an average dip of 14.8° , and the third cluster dips towards the east with an average dip of 85.1° . The transverse joint fracture set had a mean vector of $121.3^{\circ} \pm 3.2^{\circ}$ with a maximum value 69 % between 111° and 120° . The transverse fracture poles showed three clusters. The first cluster dips towards the northwest with an average dip of 42.2° , a second cluster dips towards the northwest with an average dip of 81.2° , and the third cluster dips towards the northeast with an average dip of 70.5° . The transverse joint fracture set had a mean vector of $121.3^{\circ} \pm 3.2^{\circ}$ with a maximum value 69 % between

111⁰ and 120⁰. The rose diagrams together with a 1% area counterering method used to display orientation patterns of the fracture's joints are illustrated in Plate 4.

Three sets of fracture joints were measured in five outcrops, except for outcrop 1 where no longitudinal fractures were measured. The rose diagram in outcrop 1 showed the poles to bedding plane fractures and poles to transverse plane fractures to have a mean vector of $22.3^0 \pm 6.6^0$ and $118.3^0 \pm 2.2^0$, respectively. The highest bedding fracture poles were between 11⁰ and 20⁰ with a maximum value of 33%. The highest transverse fracture poles were between 116⁰ and 120⁰ with a maximum value of 71.4%. The rose diagram in outcrop 2 showed the poles to bedding, longitudinal and transverse plane fractures to have a mean vector of $212^0 \pm 2.9^0$, $32^0 \pm 3.3^0$, and $110.6^0 \pm 1.3^0$, respectively. The highest bedding fractures poles were between 221⁰ and 230⁰ with a maximum value of 43.7%, the highest longitudinal fractures poles were between 41⁰ and 50⁰ with a maximum value of 33.3%, and the highest transverse fractures poles were between 111⁰ and 120⁰ with a maximum value of 61.9%. The rose diagram in outcrop 3 showed the poles to bedding, longitudinal and transverse plane fractures to have a mean vector of $37.3^0 \pm 2.3^0$, $229.7^0 \pm 4.0^0$, and $115.2^0 \pm 1.7^0$, respectively. The highest bedding fractures poles were between 41⁰ and 50⁰ with a maximum value of 61.5%, the highest longitudinal fractures poles were between 221⁰ and 230⁰ with a maximum value of 23.5%, and the highest transverse fractures poles were between 111⁰ and 120⁰ with a maximum value of 75%. The rose diagram in outcrop 4 showed the poles to bedding, longitudinal and transverse plane fractures to have a mean vector of $40.8^0 \pm 5.0^0$, $33.8^0 \pm 6.6^0$, and $112^0 \pm 1.7^0$, respectively. The highest bedding fractures poles were between 36⁰ and 40⁰ with a maximum value of 31.6%, the highest longitudinal fractures poles were between 41⁰ and 45⁰ with a maximum value of 28.5%, and the highest transverse fractures poles were between 111⁰ and 115⁰ with maximum value

of 63.6%. Finally, the rose diagram in outcrop 5 showed the poles to bedding, longitudinal and transverse plane fractures to have a mean vector of $83.2^{\circ} \pm 2.3^{\circ}$, $264.7^{\circ} \pm 2.2^{\circ}$, and $190^{\circ} \pm 1.8^{\circ}$, respectively. The highest bedding fractures poles were between 81° and 90° with a maximum value of 50%, the highest longitudinal fractures poles were between 261° and 270° with a maximum value of 57%, and the highest transverse fractures poles were between 181° and 190° with maximum value of 50%. A schematic cross-section with stereographic illustrations of the fracture joint sets on each outcrop is shown in Plate 2.

The matrix addition calculations for each outcrop are presented in appendix and the eigenvalues and eigenvectors calculated from the summation of tensors by site are displayed below.

Outcrop 1

$$\lambda_1 = 6.2889 \text{ ,yield an eigenvector } \begin{bmatrix} E \\ N \\ Z \end{bmatrix} = \begin{bmatrix} -0.4820 \\ -0.6579 \\ 0.5787 \end{bmatrix}$$

$$\lambda_2 = 6.1633 \text{ ,yield an eigenvector } \begin{bmatrix} E \\ N \\ Z \end{bmatrix} = \begin{bmatrix} -0.6394 \\ 0.7157 \\ 0.2811 \end{bmatrix}$$

$$\lambda_3 = 0.1256 \text{ ,yield an eigenvector } \begin{bmatrix} E \\ N \\ Z \end{bmatrix} = \begin{bmatrix} 0.5991 \\ 0.2345 \\ 0.7656 \end{bmatrix}$$

Outcrop 2

$$\lambda_1 = 2.5806E-03 \text{ ,yield an eigenvector } \begin{bmatrix} E \\ N \\ Z \end{bmatrix} = \begin{bmatrix} -8.9035E - 01 \\ -2.9016E - 01 \\ 3.5083E - 01 \end{bmatrix}$$

$$\lambda_2 = 2.3893E-03 \text{ ,yield an eigenvector } \begin{bmatrix} E \\ N \\ Z \end{bmatrix} = \begin{bmatrix} -3.1349E - 01 \\ 9.4954E - 01 \\ -1.0262E - 02 \end{bmatrix}$$

$$\lambda_3 = 1.9909E-04 \text{ ,yield an eigenvector } \begin{bmatrix} E \\ N \\ Z \end{bmatrix} = \begin{bmatrix} 3.3015E - 01 \\ 1.1912E - 01 \\ 9.3638 - 01 \end{bmatrix}$$

Outcrop 3

$$\lambda_1 = 2.6376E-02, \text{ yield an eigenvector } \begin{bmatrix} E \\ N \\ Z \end{bmatrix} = \begin{bmatrix} -5.9560E - 01 \\ -2.3134E - 01 \\ 7.6925E - 01 \end{bmatrix}$$

$$\lambda_2 = 2.3577E-02, \text{ yield an eigenvector } \begin{bmatrix} E \\ N \\ Z \end{bmatrix} = \begin{bmatrix} 7.9972E - 01 \\ -8.0689E - 02 \\ 5.9493E - 01 \end{bmatrix}$$

$$\lambda_3 = 8.9100E-03, \text{ yield an eigenvector } \begin{bmatrix} E \\ N \\ Z \end{bmatrix} = \begin{bmatrix} -7.5560E - 02 \\ 9.6952E - 01 \\ 2.3306E - 01 \end{bmatrix}$$

Outcrop 4

$$\lambda_1 = 1.8104E-02, \text{ yield an eigenvector } \begin{bmatrix} E \\ N \\ Z \end{bmatrix} = \begin{bmatrix} -6.8496E - 01 \\ -6.9644E - 01 \\ 2.2353E - 01 \end{bmatrix}$$

$$\lambda_2 = 1.2531E-02, \text{ yield an eigenvector } \begin{bmatrix} E \\ N \\ Z \end{bmatrix} = \begin{bmatrix} -3.6890E - 01 \\ 5.9466E - 01 \\ 7.1434E - 01 \end{bmatrix}$$

$$\lambda_3 = 5.5786E-02, \text{ yield an eigenvector } \begin{bmatrix} E \\ N \\ Z \end{bmatrix} = \begin{bmatrix} 6.2828E - 01 \\ -4.0684E - 01 \\ 6.6314E - 01 \end{bmatrix}$$

Outcrop 5

$$\lambda_1 = 1.8576E-04, \text{ yield an eigenvector } \begin{bmatrix} E \\ N \\ Z \end{bmatrix} = \begin{bmatrix} -3.8666E - 01 \\ 9.2220E - 01 \\ -6.9645E - 01 \end{bmatrix}$$

$$\lambda_2 = 1.1136E-04, \text{ yield an eigenvector } \begin{bmatrix} E \\ N \\ Z \end{bmatrix} = \begin{bmatrix} -8.0057E - 01 \\ -3.3190E - 01 \\ 4.9893E - 01 \end{bmatrix}$$

$$\lambda_3 = 1.0013E-04, \text{ yield an eigenvector } \begin{bmatrix} E \\ N \\ Z \end{bmatrix} = \begin{bmatrix} 4.5780E - 01 \\ 1.9849E - 01 \\ 8.6662E - 01 \end{bmatrix}$$

Using the above values of the eigenvector components, the vectors were converted back to trend and plunge and plotted as Cartesian vectors on a stereonet. The trend and plunge values are shown below in Table 7 for each outcrop and are illustrated stereographically in Plate 4.

Table 6. Trend and plunge of eigenvectors

Outcrops	Trend	Plunge
1	36.23	35.36
	138.22	16.33
	248.62	49.96
2	71.95	20.54
	341.73	0.59
	250.16	69.45
3	68.77	50.29
	275.76	36.50
	175.54	13.48
4	44.65	12.92
	148.19	36.50
	302.92	41.54
5	337.25	0.40
	67.48	29.93
	246.56	60.07

PLATE 1

Outcrops Locations with Stereographic Projection of Fracture Joints Planes on Wiley Canyon, California

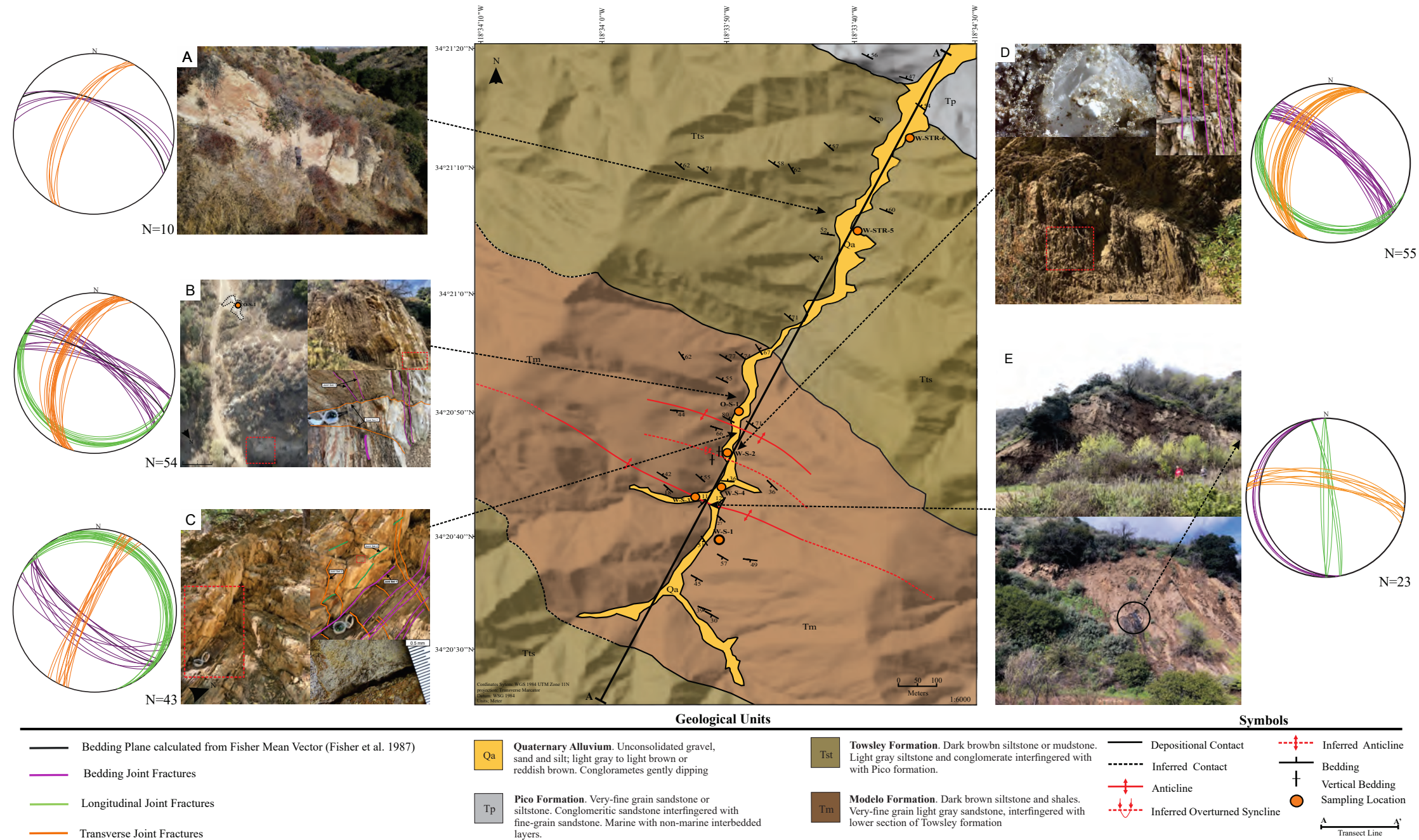
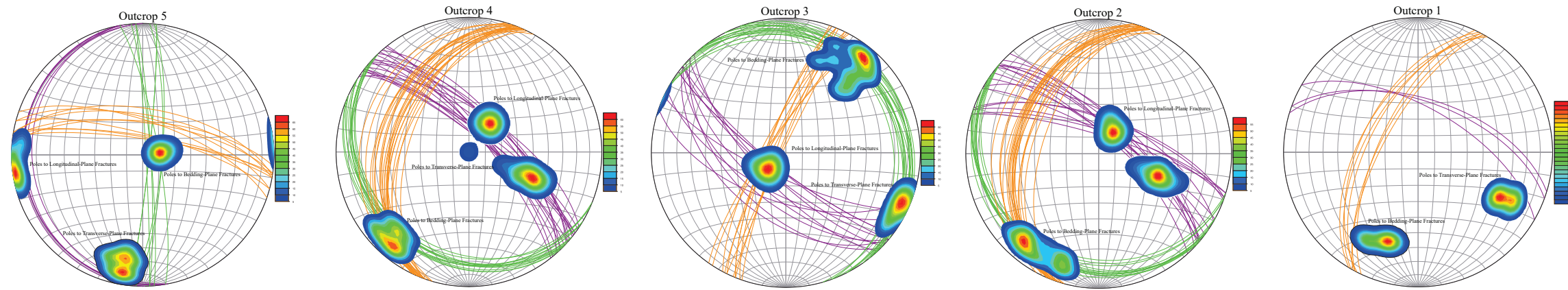


Plate 1. All five outcrops, where fracture joint measurements were taken, are illustrated throughout Wiley canyon together with a spatial relationship with sampling locations and structural features. Photographs of each outcrop location along with a stereonet that illustrates the orientation of fracture planes can be observed. Photograph A. shows outcrop 1, and illustrates where the measurements were taken on a fine to coarse grain sandstone outcrop, which is part of the Towsley formation. Photograph B. shows outcrop 2 and displays the fracture joints taken on a shales and fine grain sandstone. In addition, it shows the proximity of the outcrop relative to sampling location O-S-1. Photograph C shows outcrop 3. Photograph D shows outcrop 4 and illustrates evaporate deposits observed between shales layers. Photograph E shows outcrop 5, which is located in the axis of the Pico anticline. Photopgraph E also display a close-up of an oil seep after two days of rainfall.

PLATE 2

Schematic Cross-Section of Potential Fluid Flow Pathways and Fracture Joints Density on Wiley Canyon, California



63

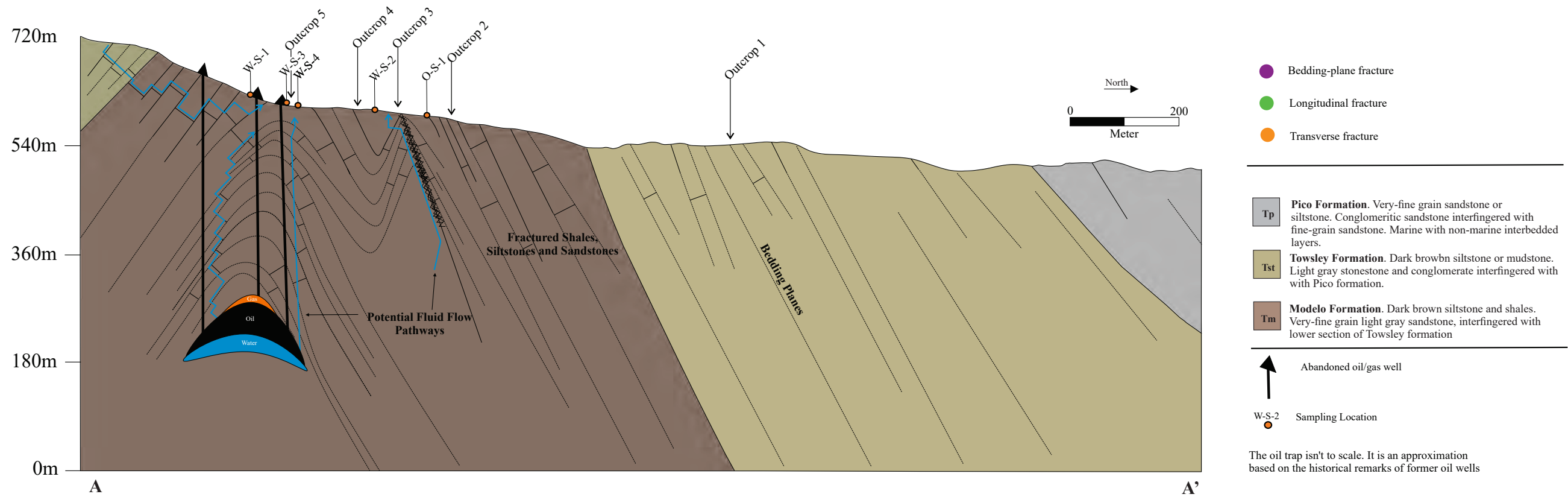
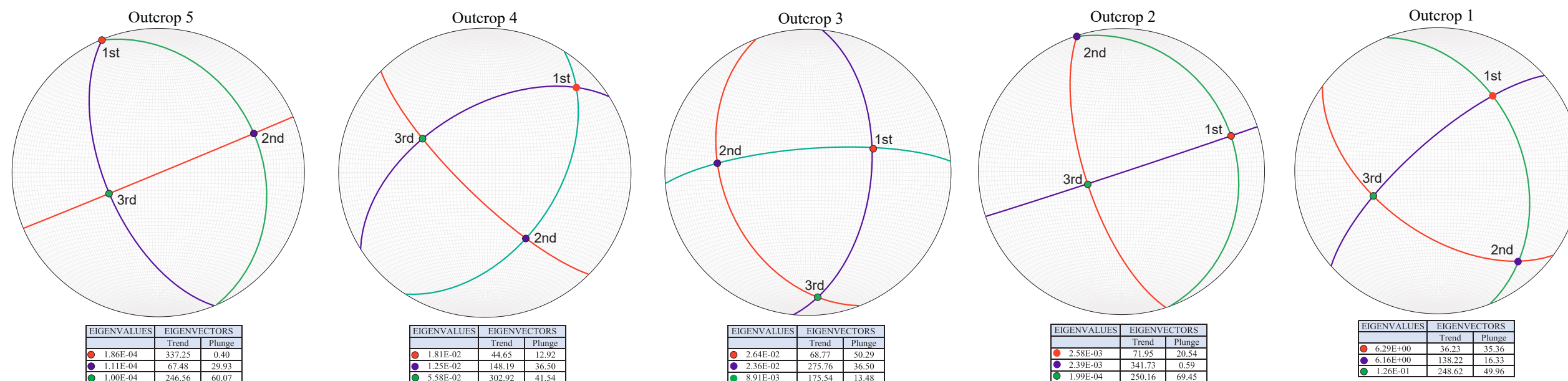
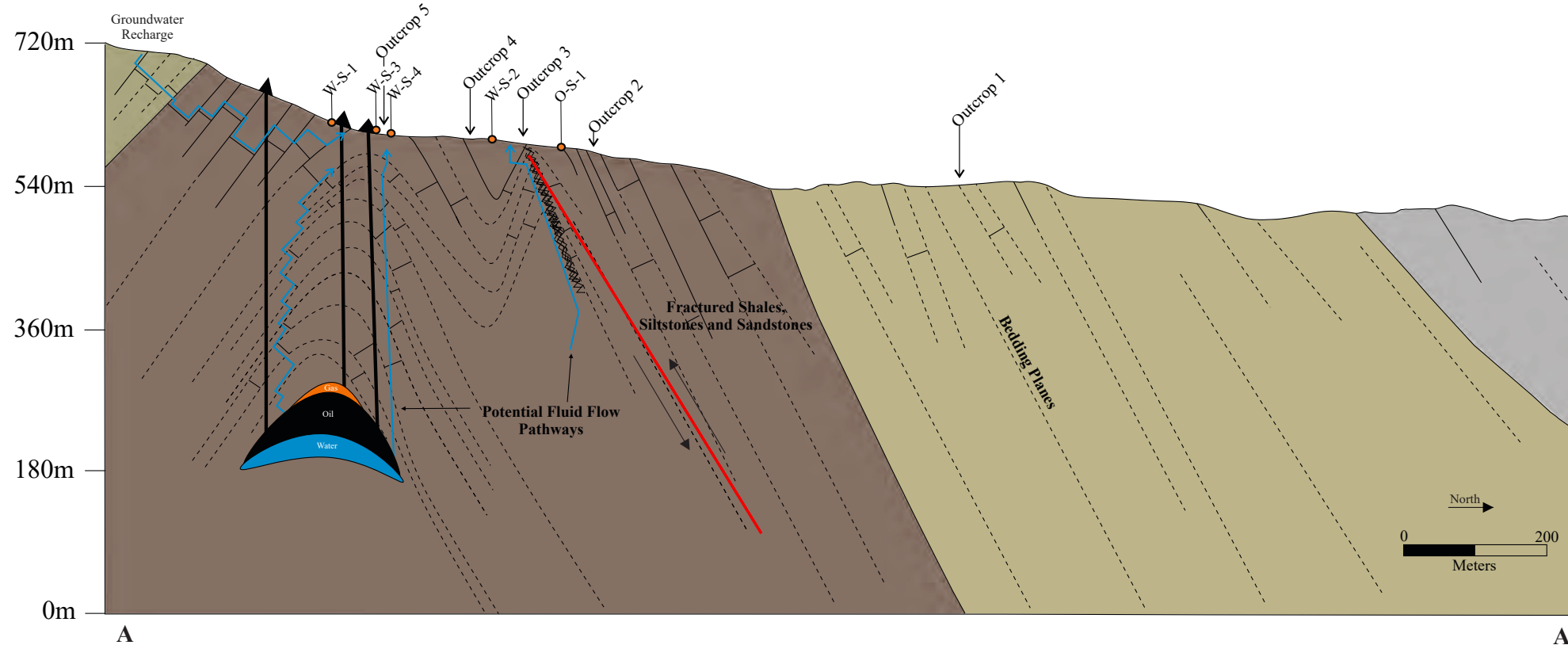


PLATE 3

Eigenvectors of each Permeability Tensor from Outcrops on Wiley Canyon, California



64



- 1st EIGENVECTOR
- 2nd EIGENVECTOR
- 3rd EIGENVECTOR

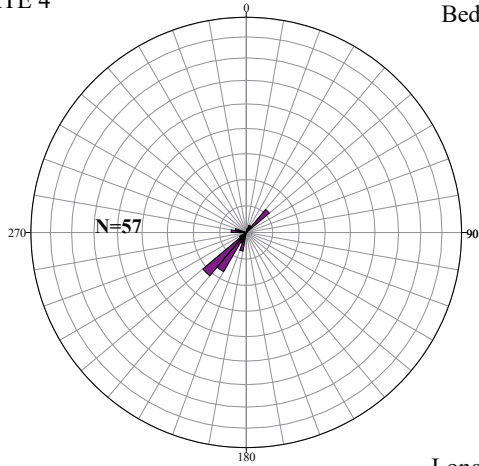
- Tp **Pico Formation.** Very-fine grain sandstone or siltstone. Conglomeritic sandstone interfingered with fine-grain sandstone. Marine with non-marine interbedded layers.
- Tst **Towsley Formation.** Dark brown siltstone or mudstone. Light gray sandstone and conglomerate interfingered with Pico formation.
- Tm **Modelo Formation.** Dark brown siltstone and shales. Very-fine grain light gray sandstone, interfingered with lower section of Towsley formation

- Abandoned oil/gas well
- W-S-2 Sampling Location
- Approximation of Blind Thrust Fault

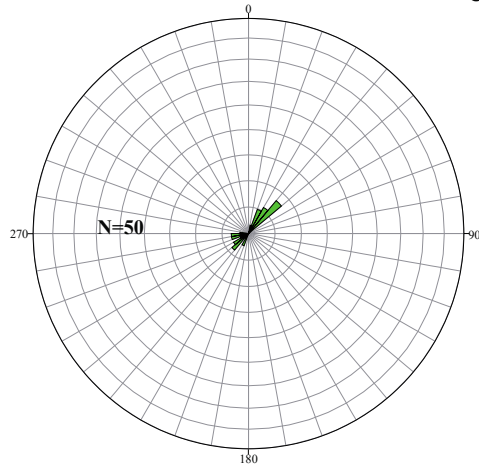
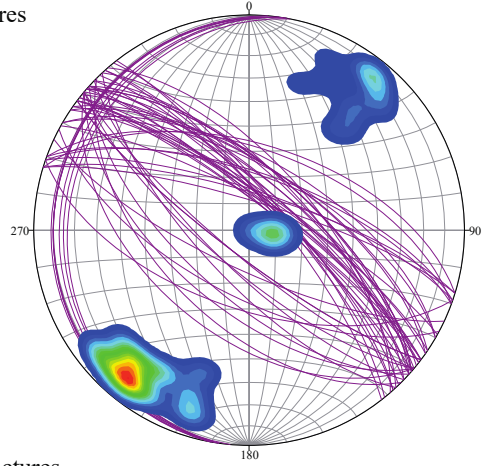
The oil trap isn't to scale. It is an approximation based on the historical remarks of former oil wells

Stereographic Projection of Fracture Planes

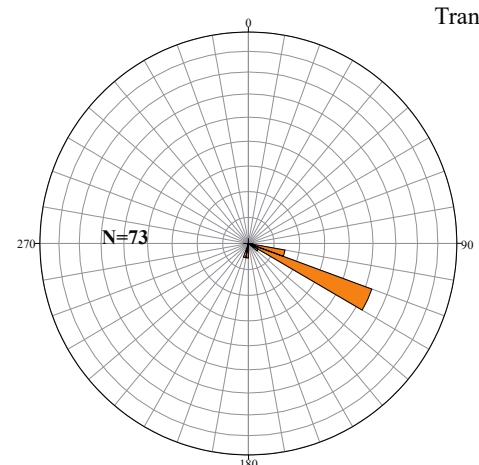
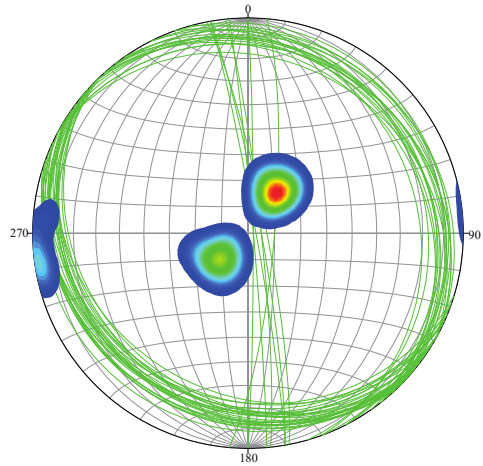
PLATE 4



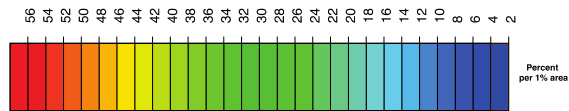
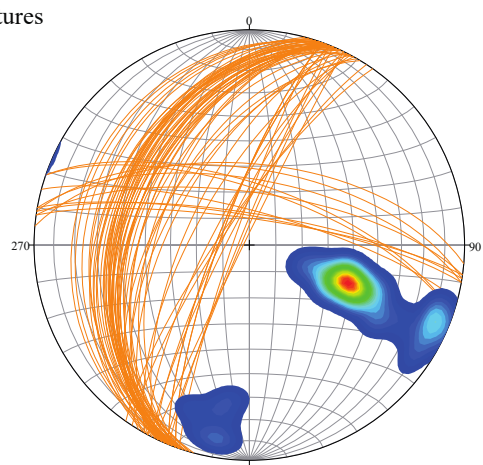
Bedding Fractures



Longitudinal Fractures



Transverse Fractures



CHAPTER 6:

DISCUSSION

This section examines the results of the water samples obtained for this research and integrates the analytical data from Kunath (2014) to address the research questions. Additionally, the geological measurements results are discussed in terms of the potential pathways for fluid migration that might be occurring in Wiley Canyon.

6.1 Field Parameters and Water Quality

The physiochemical parameters observed in the samples collected had a limited range in values. The average pH in all samples was within the range of natural waters, and slightly above the neutral value. The TDS in samples O-S-1, W-S-1 and W-S-2 weren't far apart in values relative to each other, but were from the rest of the samples, which might indicate different water sources. Samples W-STR-5 and W-STR-6 had similar TDS values with W-S-3 and W-S-4 suggesting some type of mixing between surface and groundwater, respectively. A decrease in TDS and temperature was observed in samples collected in winter after the first rain event. In several water samples, the TDS values decreased 2 and 3 orders of magnitude and were near the values observed in surface waters, suggesting that groundwater is mixing with meteoric waters, potentially driven by a seasonal effect. Figure 15 illustrates the TDS over time and shows a sudden decline in values after the first rain event. Commonly, surface waters in arid environments like Wiley Canyon hold higher temperatures than groundwater due to the sun exposure; however, our surface waters samples yielded different results. This can be attributed to the fact that the waters were collected from a flowing stream surrounded by dense vegetation. The alkalinity observed in the surface and groundwater samples were above the typical values for fresh water, indicating that the alkalinity was likely caused by the contact of the surrounding siliciclastic

rocks as the water travels through the streams, and by the water residence time and rock-water interaction in the subsurface, respectively. Stream water has an average residence time of 2.5 weeks (Oki, 2005); compared to groundwater that has a residence time of approximately 20,000 years (Fitts, 2013).

The analytical results were compared to the Environmental Protection Agency (EPA) primary and secondary drinking water regulation values to determine the water quality of our samples. None of the water samples exceeded the maximum concentration level (MCL) of fluoride. The samples collected at O-S-1 and W-S-2 exceeded the MCL value of chloride up to one order of magnitude and plotted within the brackish water range values. Even though our samples were below the typical chloride concentrations of ~20000 mg/L observed in hypersaline brines (Osborn and McIntosh, 2010), it seems, based on the chloride concentrations that these waters might have been in contact with evaporate minerals or mixed with residual brines. The chloride concentrations in all water samples were well above the value of what might be considered for natural waters of a meteoric origin.

Waters with high salt content similar to brackish waters are likely derived from evaporate beds and oil-field brines. One sample, W-S-2, gave an exceeding value of MCL of nitrate, which correspond to 44.2 mg/L when measured as nitrate ion, NO_3^- . Although the rest of the samples didn't exceed MCL for nitrate, many of them plotted well above the concentrations found in natural waters. Figure 15 illustrates the nitrate concentrations in all samples relative to the MCL of nitrate. The elevated concentrations of nitrate might have been a product of nitrification, which is basically the oxidation of ammonium to nitrate. The concentrations of nitrate on samples O-S-1 and W-S-2, which values were near the MCL, might have been a result of rocks holding abundant concentrations of ammonia

in pore water gained from the accumulation and sedimentation of organic matter (Holloway and Dahlgren, 2002), or by diagenesis processes and dissolution of clay minerals (Schroeder et al., 1998). Elevated nitrates are a result of chemical fertilizers, septic systems, industrial waste and animal farming (CDC, 2019), nevertheless these sources aren't apparent to be the cause of the elevated nitrate present in our samples.

The bromide concentrations in our samples were compared to the values obtained from a study done on the variation of bromide in potable groundwater by Davis et al. (Davis, Fabryka-Martin and Wolfsberg 2004). The comparison was made based on the fact that Wiley Canyon is located less than 20 miles from the coast, which is likely to hold higher values due to the input of seaborne aerosol in comparison to waters that exist inland. The comparison showed our bromide values to be closer to those found in coastal regions, but not a single sample surpassed modern seawater concentrations of 65-68mg/L. The highest concentrations of bromide were observed in samples O-S-1 and W-S-2 and our field observations suggest that both locations might be associated with a deep hydrocarbon system. Bromide is present in oil / gas production fields (Kogel, Trivedi, Barker, and Krukowski 2006; Dresel and Rose 2010), and since Wiley Canyon was a former oil field, it does not eradicate that discharging waters from both locations (O-S-1 and W-S-2) may have some association with a hydrocarbon system.

Sulfate values in all samples were well above the concentrations found in fresh water, even in the waters collected from streams (W-STR-5 and W-STR-6). Sulfate concentration in drinking water is between 0 to 1,000 mg/L in the United States (Trembaczowski 1991). The high concentrations of sulfate observed in surface waters might be linked to the dissolution of sulfate bearing minerals, such as barite (BaSO_4), epsomite ($\text{MgSO}_4 \cdot 7\text{H}_2\text{O}$) and gypsum ($\text{CaSO}_4 \cdot 2\text{H}_2\text{O}$) (Greenwood & Earnshaw, 1984). Gypsum deposits were

observed within the shale layers and between the sand-shale interbedded formations, which might explain the high concentration found in the surface waters. Commonly, oil field brines hold a wide range of sulfate values; and generally, the highest concentrations are found in groundwater (Abernathy et al., 2003).

Aqueous sulfate is usually subject to redox reactions. The low sulfate values in O-S-1 might have been a result of sulfate reduction. If barium and strontium were analyzed on our samples, a more apparent claim could have been made. A study on brines from the Upper Devonian in western Pennsylvania indicated that low sulfate combined with high barium and strontium values is the result of the precipitation of anhydrite and the oxidation of pyrite followed by the dissolution of barium and strontium during interactions of brines with silicates and carbonates rocks (Evan Dresel and Arthur W. Rose, 2003).

The sulfate source in W-S-2 is likely the result of microbial oxidation. This location periodically had a strong rotten egg smell and rust colored spots on the soil. Under certain conditions, dissolved hydrogen sulfide often has a rotten-egg odor, which is the result of dissimilatory sulfate reduction, a process where sulfate is reduced and hydrogen sulfide oxidizes (Canifield, 2001).

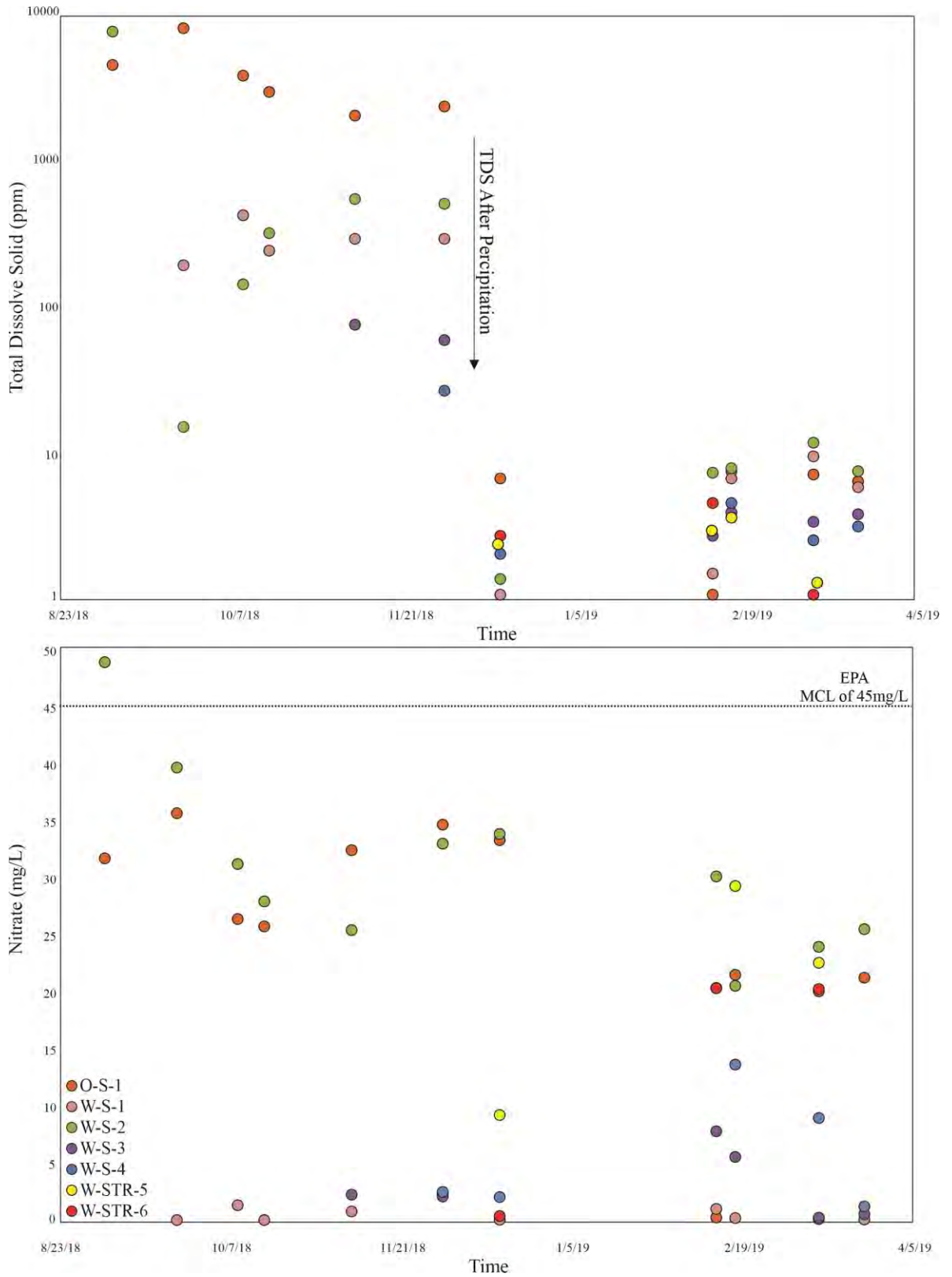


Figure 20. Total Dissolved Solid (TDS) and Nitrate over Time.

6.2 Salinity Source

The samples appear to have a wide-range of salinity concentrations based on the chloride-bromide values. Both of these constituents were carefully analyzed and used as an approximation to identify the different waters' sources present at the research site. To determine the origin and evolution of waters relative to their salinity content, the well-established Cl vs. Br and Cl/Br ratio vs. Cl concentration graphs were used. These graphs were made on a Log-Log scale due to the broad concentrations detected on the water samples.

The data revealed three apparent trends shown in Figure 16 and Figure 17. The bulk of the samples followed the seawater evaporation trend (SET) line, with each sample plotted below the modern value of seawater, suggesting that the waters of Wiley and Towsley are governed by a freshwater source. The samples plotted closer to the seawater end member suggest some sort of mixing with evaporated seawater, and those plotted near the freshwater end member are likely meteoritic in origin. A noticeable trend was observed in Figure 16, Line 1. These samples were plotted above the SET line shadowing the halite dissolution trajectory. Hydrochemical investigations carried out in sedimentary basins have shown dissolution of halite to plot above the SET line, and those that plot below generally are derived from evaporation of seawater that has been diluted by fresh or saline water (Carpenter, 1978; Gupta, 2009; Wilson, 2009). Samples O-S-1 and W-S-2 probably originated from halite dissolution based on the concentrations near the seawater, and above the SET line that follows the halite dissolution course with relative constant chloride and depleted bromide values. Additionally, the presence of gypsum deposits observed in rocks formation might suggest the possibility of halite deposits. Gypsum deposits were observed in outcrops 2, 3 and 4, and are geospatially located near sampling locations O-S-1 and W-

S-2 (Refer to Plate 1 and Plate 2, photograph D). Commonly, where gypsum deposits are found, halite deposits might be present. McIntosh et al (2004) showed in a study done in the Michigan Basin that samples with high Cl/Br are results of halite dissolution. This implies that O-S-1 and W-S-2 might have been in direct contact with halite deposits, or perhaps the high Cl/Br ratios is the product of mixing with a hyper-saline source from depth. If the high chloride and low bromide values is a product of mixing with hyper-saline waters generated at profound depths, the salinity of these waters might have originated during the Miocene paleoenvironment. This critical geological period experienced extreme warming that globally altered the seawater levels and likely formed evaporitic deposits during those changes. This period was called the Mid-Miocene Climatic Optimum (MMCO).

A small cluster of 5 samples from Towsley (Kunath, 2014) are plotted above the SET line and it seems to be inclined to a freshwater end-member (refer to Line 2 in Figure 16). These samples that plotted on and above the Cl/Br ratio of seawater shown in Figure 17 (refer to Line 2) might suggest slight evaporate dissolution with a freshwater source. These samples might be originated from shallow depths where there may be a lack of halite deposits with high freshwater circulation. A trend parallel and below the SET line was observed on Kunath, 2014 samples, and it is possible that these samples originated from the mixing of freshwater with residual brines. None of our samples were plotted below the SET line. Several studies on sedimentary basins (Bruno et al., 2003; Kharaka, Y. K., and J. S. Hanor, 2003; Osborn S, and McIntosh J, 2010), have interpreted samples that plotted below the SET line and that contained fairly low Cl/Br values to be from the mixing between brines that were evaporated past halite saturation or from concentrated seawater. The Cl/Br ratios on Kunath (2014) samples were to 2 to 4 orders of magnitude lower than

our samples that are suspected to be from halite dissolution. The low Cl/Br ratio together with low chloride concentrations points towards a non-marine source or mixing with a freshwater source. It is possible that the suspected residual brines are remnant fluids trapped during the deposition and accumulation of Paleogene and Neogene sediments due to faulting and thrusting of the Ventura Basin (Deméré, 1983; Namson and Davis, 1990; Yeats et al., 1994), or by the sea level fluctuation through the Plio-Pleistocene (Buczeck et al., 2020). The samples collected for this research are reasonably comparable with Kunath, 2014 data, except for those samples abovementioned that plot below the SET line. Our sample revealed two apparent trends strongly influenced by a freshwater source.

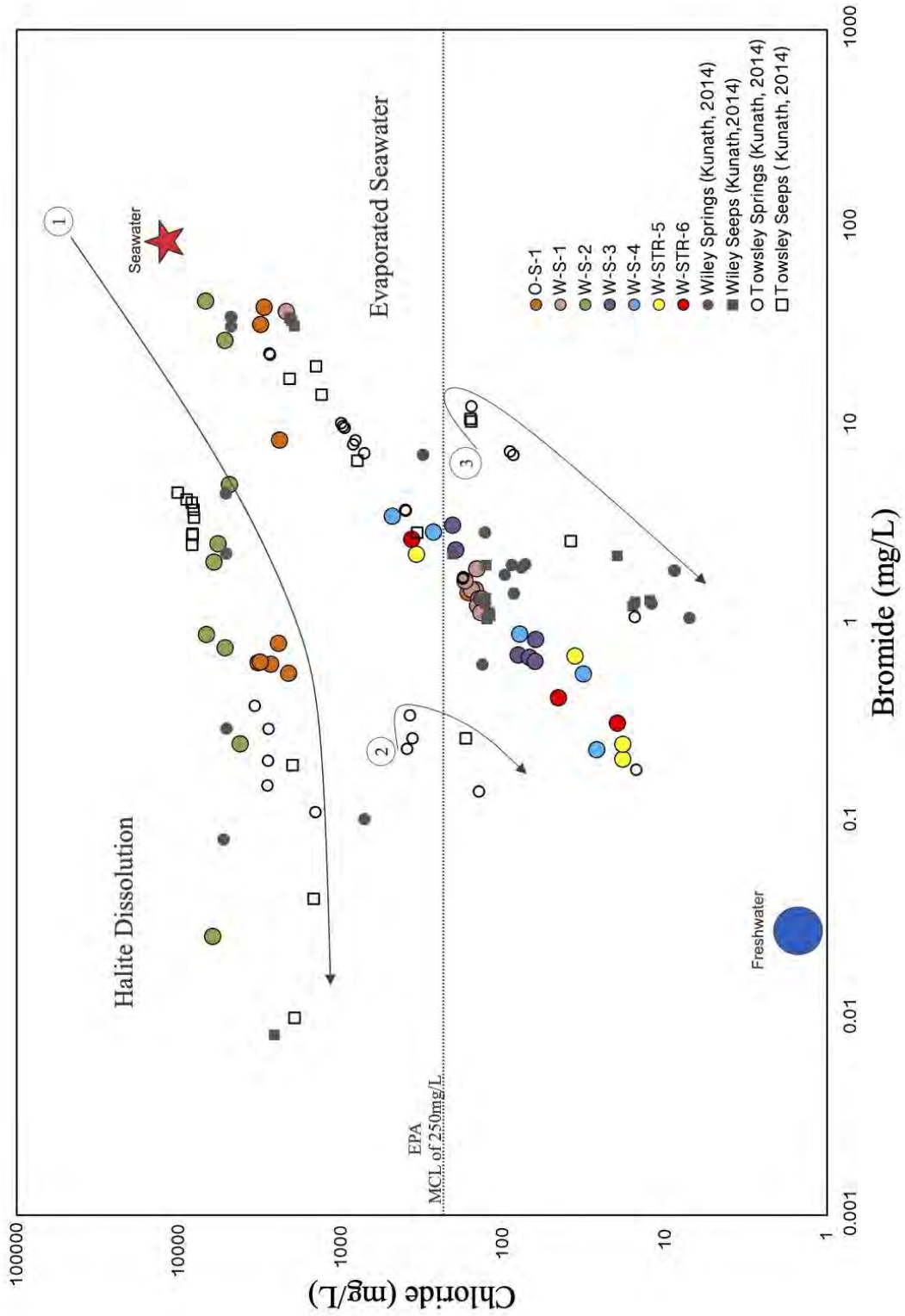


Figure 21. Binary graph of Chloride vs Bromide. The encircle numbers displayed the possible trends observed in the water samples.

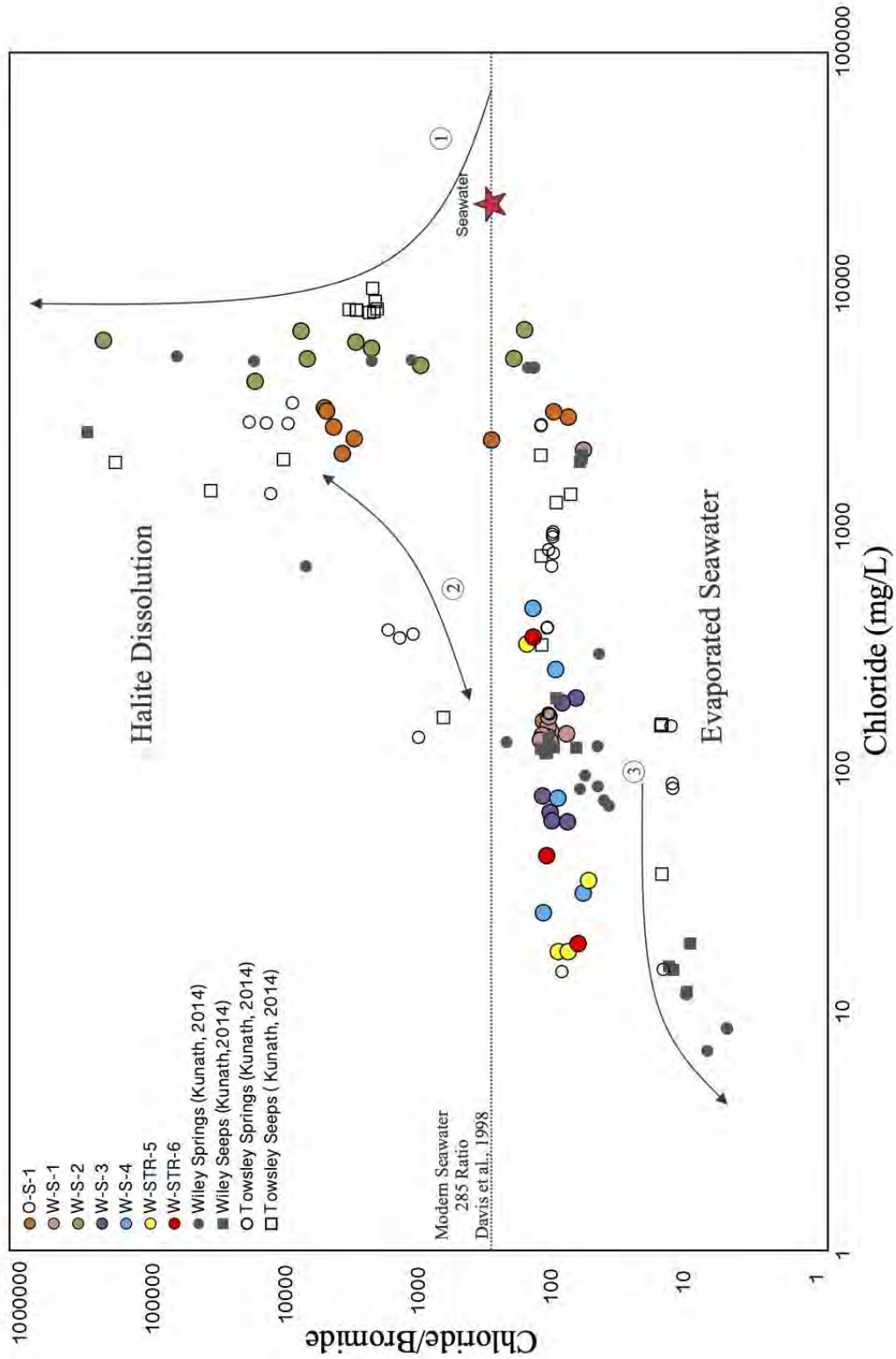


Figure 22. Binary graph of Chloride/Bromide ratio. The encircle numbers displayed the possible trends observed in the water samples.

Each sampling location was considered to evaluate any sort of correlation between the proximity of abandoned oil/gas wells and geological structures with chloride concentrations. The W-STR-5 and W-STR-6 locations, which are stream waters, appeared to have no correlation with oil/gas wells or any geological structure and their chloride concentrations are likely the result of contact with tar deposits along the creek. Sampling location O-S-1 was approximately 20 meters south of three abandoned oil wells (7, 9 and 17) and holds high chloride concentrations. Historical records show these wells to have discharged fluids to the surface after they were first abandoned in the late 19th and mid-20th centuries. This suggests that the salinity concentrations of O-S-1 could be related to the proximity of these wells or that O-S-1 is situated in a weak zone between the geological contact of the Modelo and Towsley Formation. Although W-S-1 is positioned less than 10 meters downgradient of well 11 and adjacent to well 6, the chloride concentrations in the water samples do not suggest any association between production fluids found in oil/gas wells. The nearest oil/gas well from W-S-2 is approximately 25 meters. The water samples on this location contain the highest chloride as well as bromide concentrations. The discharging fluids in W-S-2 were found adjacent to a kink fold and highly fractured rocks, which indicate a direct correlation between the salinity and geologic structures that might have some sort of communication with a deep hyper-saline water source, refer to Plate 2. W-S-3 and W-S-4 locations are surrounded by several abandoned wells and located near the Pico anticline. Both contain low to medium-low chloride concentrations, suggesting no correlation between the proximity of the wells and their salinity. Because of their locations, it is possible that the salinity concentrations derive from a fresh water source

6.3 Fractures and Permeability

Field observations, geological measurements and historical use of Wiley Canyon, suggest that there might be upward fluid migration along preferential pathways. It is likely, based on the topographic gradient, that groundwater is recharged up gradient south of the Pico anticline. In sedimentary basins, the topographic gradient has been shown to form long groundwater flow pathways (Flewelling and Sharma, 2014). Overpressure generally drives fluids to migrate upward, and the overpressure can be generated by many factors including sediment compaction, diagenesis, hydrocarbon generation and tectonics compression. These controlling factors of overpressure in sedimentary basins are likely present in Wiley Canyon. Oil and water was observed after rainfall oozing out of the surface in many locations (refer to Plate 1, Photograph E), in particular near the Pico anticline axis and around highly fractured rocks. It is likely that fluids seep out in zones where the rocks are extremely fractured. The more fractures in the rock, the greater the possibility of connectivity between the fractures and, therefore, the greater the permeability of the rock.

Several suggestions arose from this research in terms of what caused fluids to be discharged to the surface. There are many dynamic hydrogeological factors that influence fluid migration; however, based on the field observations and measurements it appears that the main controlling factor is the geology of Wiley Canyon. Fluids may be migrating upward along complex fracture networks that act as conduits for groundwater flow and considering that the rocks are extremely fractured with different dip orientations indicates the fracture joints may be experiencing different degrees of anisotropy. For example, fracture joints that are vertically dipped may experience maximum anisotropy, where groundwater will flow along the strike governed by the hydraulic gradient. However,

fracture joints that are horizontal have minimal or no anisotropy, and therefore the groundwater flow will be driven entirely by the direction of the gradient. The orientation of the bedding-plane fractures, which are moderately to nearly vertically tilted, might divert the groundwater flow of many water bearing units. It is possible that these fractures have some communication with deep brines and consequently transport the brines upwards where they mix with shallow freshwater aquifers. Fluid flow is generally greater in bedding-planes where fluid flows parallel to the planes than where fluid flows perpendicular to the planes. This can be visualized in figure 4 and 5, which based on the nearly vertical bedding-planes fluid flow might be migrating upwards in between planes caused by an upwards pressure gradient. A conceptual groundwater flow model concluded that flow occurs along bedding planes fractures of fairly homogenous sedimentary rocks (Marin, 1992). At location W-S-2, water was seeping out of highly fractured shales layers. A schematic cross section (Plate 2) illustrates groundwater flow that might potentially be occurring along different damage zones. These damage zones are made of complex fracture networks that particularly enhance the permeability of the rock and act as preferential pathways for fluid flow. It appears that upward fluid migration might be occurring between and near sampling locations O-S-1 and W-S-2 based on the bedding planes that are nearly vertical and highly fractured (refer to Plate 1, photographs B, C and D). In addition, there is a geospatial relationship between locations O-S-1 and W-S-2 with outcrops 2, 3 and 4. O-S-1 is located between outcrop 2 and outcrop 3, roughly 50 meters to the north and 43 meters to the south, respectively. Both of these outcrops have fracture joints with steep angles that can act as preferential pathways in the vertical direction (Plate 2). Location W-S-2 is located within a deformation zone where bedding layers are overturned and folded, and based on our field interpretation; this might be an overturned syncline. Plate 1,

photograph D shows vertical shales layers with minor drag folds. It seems that the density and the aperture of the joint fractures observed near W-S-2 are enhancing the permeability of the rocks layers facilitating fluid to migrate upward along these joint fracture sets. Near the axis of the Pico anticline, where the bedding planes are near horizontal, it is assumed that the groundwater flow will be driven by the hydraulic gradient.

It appears to be a fault-propagation fold between sampling locations W-S-2 and O-S-1 based on the highest deformation zone and cluster density distribution of the poles shown in outcrops 2, 3 and 4 (Plate 2). The dominant joint fracture sets in outcrop 2 appear to be the bedding fractures and transverse fractures, both of which have steep dip angles. A geospatial relationship of outcrop 2 to O-S-1 is illustrated in Plate 1, photograph B. The distance between outcrop 2 and O-S-1 is approximate 40 meters, which suggest that might be some type of some correlation between the discharging fluids and rock deformation. Outcrop 5 is near sampling locations W-S-3 and W-S-4, and approximately 80 meters north of W-S-1 (Plate 1 and 2). Although the longitudinal and transverse fractures are nearly vertical in outcrop 5, which potentially can act as conduits for upward fluids, the rock layers and bedding fractures are nearly horizontal. In addition, the fracture frequency in outcrop 5 is far less than outcrops north of the Pico anticline (Plate 2), and based on these factors, vertical migration is likely not as frequent as in outcrops 2, 3, and 4. Besides the permeability of fluid flow perpendicular to bedding is less than fluid flow parallel to bedding. However, it is possible that there are other factors that drive fluids upwards near outcrop 5, and perhaps fracture joints are just enhancers for preferential conduits.

The assumption was made that fracture joints apertures at the surface were likely enlarged by a similar ratio, and therefore the direction of the eigenvectors were considered for permeability approximation instead of the absolute magnitude. In addition, it was

thought that the fracture joints apertures would varied with depth, which was considered as the biggest uncertainty for the permeability tensor approach. Since the fracture joints aperture were measured at the surface and were expected to be widen by surface weathering, the permeability tensor was cautiously used as an approximation for the overall permeability direction. It was considered that permeability would decreases with depth as the joint fractures apertures are narrower or closed by an overburden pressure and/or by stress changes in the subsurface. Fluid circulation occurs at depth, so other processes that might influence the fracture joints aperture at depth were considered. For example, mineral dissolution or precipitation can cause fracture joints to either be open or closed. Physical and/or chemical weathering can easily alter the aperture of the fracture, and the rate of weathering between each outcrop will varied depending on the overall physiochemical properties of the rocks. Is been shown that dissolution of minerals in carbonate aquifers increase the fracture aperture generating a positive feedback look for fluid flow (Kaufmann, 2012). It was observed that the permeability tensor in the fracture joint sets was weighted on the average opening of the fractures, which was to be expected considering that equation 9 incorporates Snow's (1969) equation of fluid flow velocity between two parallel plates in which the aperture of the plates have strong influence on the fluid flow velocity.

Due to likely overestimation of the permeability tensor related to fracture joints aperture caused by surface weathering, the absolute magnitude calculations of the tensors were cautiously used for interpretation. The vertical permeability obtained from the permeability tensor matrix on each outcrop was carefully analyzed. High density fracture joints were observed in shales layers than in fine to coarse grain sandstones. Outcrop 1 had very few fractures joints, yet their aperture was noticeably higher than the rest of the outcrops. The

average aperture of the fracture joints in outcrop 1 was 16.3mm while the rest of the outcrops had an average of 2.1mm. However, the spacing between fracture joints in outcrop 1 was noticeably larger and contained very minimum fractures within a 5 square meter area. Plate 1; photograph A, shows the fracture joints on the sandstone widely spaced out. It appears that fracture joints aperture on outcrop 1 is controlled by physical weathering. Precipitated minerals were overserved in outcrops 2, 3 and 4, which indicates that the frequency of fracture joints might be higher due to chemical and physical weathering. The dissolution of minerals (chemical weathering) generally removes material, which allows for physical weathering to break the rock easier. Plate 1, photograph D, illustrates precipitated minerals between fracture joints; in addition, fracture aperture ($< 0.5\text{mm}$) can be observed in photograph C.

Based on outcrop 1 eigenvalues, the highest value was observed in K_{yy} , which indicates the outcrop's highest permeability direction is towards the north caused by a northward pressure gradient. Similar to outcrop 1, all other outcrops except outcrop 3 have the highest eigenvalue in K_{yy} . Outcrop 3 highest eigenvalues were observed in K_{xx} and K_{yy} , which indicates the highest permeability to be towards the east and upward direction generated by an eastward, upward pressure gradient. Interestingly, outcrop 3 is located in a possible fault bend fold and between the two sampling locations where it is suspected, based on the analytical analysis of the discharge waters, that both locations OS-1 and WS-2 are being influenced by some kind of ascending fluids.

Stereographic illustrations of the eigenvectors directions together with their eigenvalues, which is the magnitude of permeability along those directions, are shown in Plate 3. To address the claim that there could be upward fluids migrating from depths along the fracture joints, the high angle eigenvectors with their corresponding magnitude at each

outcrop were considered to see if the maximum permeability is along the vertical direction. To simplify the classification of the eigenvector direction, the following angle directions were considered 1) vertical 90^0-80^0 , 2) sub-vertical 80^0-70^0 , 3) high angle 60^0-50^0 , and 4) moderate to horizontal 50^0-0^0 . The highest eigenvalue observed was in outcrop 3, with an eigenvector in the high angle direction. This outcrop has been of interest because it lies between sampling locations O-S-1 and W-S-2, in addition as previously mentioned, this outcrop is located near the suspected fault bend fold and within a highest deformation zone. The rest of the outcrops contained the highest eigenvalues pointing towards a moderate to horizontal direction; however, these values aren't far apart from those that point towards a more vertical direction. In fact, some of values are in the same order of magnitude. There might be some sort of fracture connectivity network between outcrops 2, 3 and 4 that are acting as preferential pathways for fluids to migrate along the fractures.

6.4 Abandoned Oil Wells

It was considered that fluid might be migrating along abandoned vertical oil/gas wells. This consideration was made because the majority of oil wells were drilled on the Pico anticline and in the northern flank, and based upon two assumptions: 1) Numerous oil/gas wells were abandoned before the existence of the Division of Oil and Gas (D.O.G) and 2) Seal integrity. The first assumption was obvious due to the lack of documentation in how the wells were abandoned, which means there is no record of the types of materials used to seal the different oil or water bearing units, and no record of the depths between seals or whether casing was left in the borehole or pulled out. These are just some of the concerns that were considered in terms of possible fluid migration along these abandoned oil/gas wells. The integrity of a seal, combined with the plug and abandonment operations, ensures long lasting well integrity. Generally, the purpose of well abandonment is to plug or isolate

different oil/gas and water bearing units and to prevent fluids from migrating into uncontaminated groundwater. However, there are situations where preferential pathways can form along abandoned wells.

It is challenging to confirm that fluids are migrating throughout the abandoned oil/gas wells in Wiley Canyon, but it is possible that the cement seals and casings could have been deteriorated over time. Celia et al. (2005) showed that possible leakage can occur between cement and casings, between cement and formation rocks, through cracks in the cement or through the casing itself. It was considered that these possible causes could be altered by natural occurring earthquakes. Perhaps, the mechanism of upwards fluid migration can be a combination of geological structures and abandoned well integrity.

CHAPTER 7:

CONCLUSIONS

The results from water samples, together with previous data, field measurements and observations, gave an understanding of the possible origin of the waters present and the mechanism that drives the fluids to the surface. The conclusions of this study are as follows:

- There are conceivably two water sources in Wiley Canyon based on the trends observed in the chloride and bromide results. Five samples are from a freshwater source and possibly two out the five are mixing with some sort saline waters. The other two water samples are evident to originate from halite dissolution and mixing with a freshwater source, likely a shallow aquifer.
- The results from Kunath, 2014 of Wiley Canyon and Towsley Canyon are similar to this study in terms of the waters' origin. However, certain samples in Towsley Canyon show to be mixing with some sort of brines from depth or residuals of evaporated seawater. Additional analysis on the Towsley Canyon water should be carried out to delineate their origin.
- There is a geological control on the oil/gas and water seeps. It is expected, based on the field measurements and observations, that fractures joints might be one of the controlling factors driving fluids upward from depth to the surface and the fracture connectivity network is acting as preferential pathways fluid flow.
- The integrity of abandoned oil / gas wells could be contributing as a possible source for upward fluid migration.

FUTURE WORK

To further define and constrain the origin and evolution of the discharging waters present in Wiley Canyon, a more vigorous analytical study of the discharging waters should be implemented. These analyses comprise of cations, trace metals and stable isotopes. The study of these constituents would allow a better insight of the hydrogeological processes such as recharge and weathering processes, age of the waters, biogeochemical cycles and a higher understanding of the water salinity sources. Additionally, a similar study should be applied in Towsley Canyon and neighbor Canyons (Pico, De Witt, Rice and East), situated along the Pico anticline. This would allow to test if there are any sort of regional fluid migration from depth and if discharging waters are constrained along the axis of the Pico anticline. A more advanced analysis on structural measurements would enhance the understanding on geological controls of local and regional groundwater flow. This would include a 2-D model on fault displacement caused by regional stresses to investigate and compare paleo and present-day groundwater flow assuming that water was and is flowing along faults. Also, hydraulic head measurements can be used to identify with horizontal flow paths, and as a tool for contaminant transport assessment.

REFERENCES

- Alcalá, Francisco J and Custodio, Emilio. Using the Cl/Br ratio as a tracer to identify the origin of salinity in aquifers in Spain and Portugal. *Journal of Hydrology*, Volume 359, Issues 1–2, 2008. 189-207.
- Allmendinger, R., Cardozo, N., & Fisher, D. (2011). Coordinate systems, scalars, and vectors. In *Structural Geology Algorithms: Vectors and Tensors* (pp. 23-43). Cambridge: Cambridge University Press.
- Apostolos Kantzas; Jonathan Bryan; and Saeed Taheri. *Fundamentals of fluid flow in porous media*. 2014
- Aristides C. Liakopoulos (1965) Theoretical solution of the unsteady unsaturated flow problems in soils, *International Association of Scientific Hydrology. Bulletin*, 10:1, 5-39.
- Arndt Schimmelmann, Scott A. Ensminger, Agnieszka Drobniak, Maria Mastalerz, Giuseppe Etiope, Robert D. Jacobi, Christian Frankenberg, Natural geological seepage of hydrocarbon gas in the Appalachian Basin and Midwest USA in relation to shale tectonic fracturing and past industrial hydrocarbon production, *Science of The Total Environment*, Volume 644, 2018, Pages 982-993.
- Atwater, T. “Plate Tectonic History of Southern California with Emphasis on the Western Transverse Ranges and Northern Channel Islands.” (1998).
- Awadh, S. M., Al-Auweidy, M. R., & Al-Yaseri, A. A. (2019). Hydrochemistry as a tool for interpreting brine origin and chemical equilibrium in oilfields: Zubair reservoir southern Iraq case study. *Applied Water Science*, 9(3).
- Bachu, S., & Hitchon, B. (1996). Regional-scale flow of formation waters in the Williston Basin. *AAPG Bulletin*, **80** (2), 248– 264.
- Banks D. A., Gutzmer J., Lüders V., Beukes N. J. and Von Bezing K. L. (2003) The composition of seawater in the Palaeoproterozoic. *Trans. Inst. Min. Metall. B Appl. Earth Science*.
- Berre, I. et al. “Flow in Fractured Porous Media: A Review of Conceptual Models and Discretization Approaches.” *Transport in Porous Media* (2018): 1-22.
- Brief History of Oil Development in Wiley Canyon. Retrieved July 12, 2019,
- Caine, J. S., Forster, C. B., and Evans, J. P., 1993, A classification scheme for permeability structures in fault zones: *Eos* (Transactions, American Geophysical Union), v. 74, p. 677.

- Campbell, R. H., Wills, C. J., Irvine, P. J., & Swanson, B. J. (2014). Preliminary geologic map of the Los Angeles 30' × 60' quadrangle, Southern California (Vol. 2.0). California: California Geological Survey, United States Geological Survey.
- Campbell, R.H., McCulloh, T.H., and Vedder, J.G., 2007, revised 2009, The Topanga Group; a 100-year history of changes in stratigraphic nomenclature: U.S. Geological Survey, Open-File Report 2007-1385, version 1.1, 36 p.
- Carpenter, A. B. (1978). Origin and chemical evolution of brines in sedimentary basins. Paper presented at the SPE Annual Fall Technical Conference and Exhibition, Houston, Texas.
- Celia, M. A. and Bachu, S.: 2003, 'Geological sequestration of CO₂: Is leakage unavoidable and acceptable', in Gale, J. and Kaya, Y. (eds), Sixth International Conference on Greenhouse Gas Control Technologies, Kyoto, vol. I, Pergamon, Amsterdam, pp. 477–482.
- Custodio, E. and Llamas, M.R. (1983). Hidrología Subterránea. Editorial Omega. Barcelona (2 Vols). 1-2350.
- Davis, S. N., Whittemore, D. O., & Fabryka-Martin, J. (March-April 1998). Uses of Chloride/Bromide Ratios in Studies of Potable Water. *Ground Water*, 338-349.
- DesRoches, A., Danielescu, S. & Butler, K. Structural controls on groundwater flow in a fractured bedrock aquifer underlying an agricultural region of northwestern New Brunswick, Canada. *Hydrogeology J* 22, 1067–1086 (2014).
- Dickey, P. A. (1969). Increasing concentration of subsurface brines with depth. *Chemical Geology*, 4(1–2), 361–370.
- Dibblee, T.W. Jr., 1992c, Geologic map of the Oat Mountain and Canoga Park (North 1/2) Quadrangles, Los Angeles County, California: Dibblee Geological Foundation Map DF-36, Santa Barbara, California, scale 1:24,000
- Donaldson, E. C., & Alam, W. (2013). *Wettability*. Burlington: Elsevier Science.
- Dresel, P.E., Rose, A.W., 2010. Chemistry and Origin of Oil and Gas well Brines in Western Pennsylvania. *Pennsylvania Geol. Surv.*, 4th ser.,
- Evangelou VP, Seta AK, Holt A. Potential role of bicarbonate during pyrite oxidation. *Environ Sci Technol* 1998;32:2084–91.
- Ferguson, G., McIntosh, J. C., Grasby, S. E., Hendry, M. J., Jasechko, S., Lindsay, M. B. J., & Luijendijk, E. (2018). The persistence of brines in sedimentary basins. *Geophysical Research Letters*, 45

- Flewelling, S.A. and Sharma, M. (2014), Constraints on Upward Migration of Hydraulic Fracturing Fluid and Brine. *Groundwater*, 52: 9-19.
- Forjanes P, Astilleros JM, Fernández-Díaz L. The Formation of Barite and Celestite through the Replacement of Gypsum. *Minerals*. 2020; 10(2):189.
- Gaupp, Reinhard & Moeller, Peter & Lüders, Volker & di Primio, Rolando & Littke, Ralf & Urai, Janos & Nover, Georg & Zwach, C. & Ondrak, Robert & Schöner, R. & Krooss, Bernhard & Cramer, B. & Plessen, Birgit & Machel, Hans. (2008). *Fluid Systems*.
- Gelcich, V. (1866, January 02). Petroleum in Los Angeles County. *Wilmington Journal*.
- Grasby, S. E., & Chen, Z. (2005). Subglacial recharge into the Western Canada Sedimentary Basin—Impact of Pleistocene glaciation on basin hydrodynamics. *Geological Society of America Bulletin*, 117(3), 500– 514
- Greenwood NN, Earnshaw A. 1984. *Chemistry of the Elements*. Oxford, England: Pergamon Press.
- Gupta, I., Wilson, A. M., & Rostron, B. J. (2012). Cl/Br compositions as indicators of the origin of brines: Hydrogeologic simulations of the Alberta Basin, Canada. *Geological Society of America Bulletin*, 124(1–2), 200– 212.
- Harraz, H. Z. (2015, October). *Evaporite Salt Deposits*. Lecture.
- Hem, J. D. (1970) Study and interpretation of the chemical characteristics of natural water. *USGS Wat. Supply Pap.* 1473
- Holloway, JoAnn & Dahlgren, Randy. (2002). Holloway, J. M. & Dahlgren, R. A. Nitrogen in rock: Occurrences and biogeochemical implications. *Glob. Biogeochem. Cycles* 16, 1118. *Global biogeochemical*.
- Hoori Ajami, *Geohydrology: Groundwater*, Editor(s): David Alderton, Scott A. Elias, *Encyclopedia of Geology (Second Edition)*, Academic Press, 2021, Pages 408-415.
- Jørgensen Bo Barker, Findlay Alyssa J., Pellerin André. The Biogeochemical Sulfur Cycle of Marine Sediments. *Frontiers in Microbiology*. 2019. 10.3389/fmicb.2019.00849
- Joris M. Gieskes, W. Carl Rogers. Alkalinity Determination in Interstitial Waters of Marine Sediments *SEPM Journal of Sedimentary Research*(1973), Vol. 43
- Kamerling, M. J., and Luyendyk, B. P. (1985), Paleomagnetism and neogene tectonics of the Northern Channel Islands, California, *J. Geophys. Res.*, 90(B14).
- Kendall, A.C. and Harwood, G.M. (1996) Marine evaporites; arid shorelines and basins. In H.G.Reading (ed.), *Sedimentary Environments, Processes, Facies and Stratigraphy*. Blackwell Science, pp. 281-324.

- Kew, W. S. W., 1919b, Structure and oil resources of the Simi Valley, southern California: U. S. Geological Survey, Bulletin 691, p. 323-347
- Kharaka, Y., & Hanor, J. (2003). Deep Fluids in the Continents: I. Sedimentary Basins. *Treatise on Geochemistry*, 1-48. doi:10.1016/b0-08-043751-6/05085-4
- Kharaka, Y. and Nancy S. Dorsey. “Environmental issues of petroleum exploration and production: Introduction.” *Environmental Geosciences* 12 (2005): 61-63.
- Lang, P. S., Paluszny, A., Nejati, M., & Zimmerman, R. W. (2018). Relationship between the orientation of maximum permeability and intermediate principal stress in fractured rocks. *Water Resources Research*, 54.
- Lang, P. S., Paluszny, A., and Zimmerman, R. W. (2014), Permeability tensor of three-dimensional fractured porous rock and a comparison to trace map predictions, *J. Geophys. Res. Solid Earth*, 119, 6288– 6307, doi:10.1002/2014JB011027.
- Lasseter, T. J., Waggoner, J. R. and Lake, L. W. 1986. “Reservoir heterogeneities and their influence on ultimate recovery”. In *Reservoir Characterization*, Vol. 545, Orlando, Florida: Academic Press Inc.
- Lawrence Cook Bonham; Structural petrology of the Pico Anticline, Los Angeles County, California. *Journal of Sedimentary Research* 1957;; 27 (3): 251–264.
- Letouzey, J., 1990, Fault reactivation, inversion and fold-thrust belt, in J. Letouzey, ed., *Petroleum and tectonics in mobile belts*: Paris, Editions Technip, p. 101 – 128
- Link, W. K. Significance of oil and gas. Seeps in world oil exploration. *AAPG Bull.* 36, 1505–1541 (1952).
- Mainguy, M., Longuemare, P., Audibert, A., & Lecolier, E. (2007). Analyzing the Risk of Well Plug Failure after Abandonment. *Oil and Gas Science and Technology*, 62 (3), 311-324.
- Maillot, J., Davy, P., Goc, R. L., Darcel, C., & Dreuzy, J. R. d. (2016). Connectivity, permeability, and channeling in randomly distributed and kinematically defined discrete fracture network models. *Water Resources Research*, 52(11).
- McIntosh, J., Garven, G., & Hanor, J. (2011). Impacts of Pleistocene glaciation on large-scale groundwater flow and salinity in the Michigan Basin. *Geofluids*, 11(1), 18–33.
- Miao, Z., Brusseau, M.L., Carroll, K.C. et al. Sulfate reduction in groundwater: characterization and applications for remediation. *Environ Geochem Health* 34, 539–550 (2012).
- Nicolas Beaudoin, Damien Huyghe, Nicolas Bellahsen, Olivier Lacombe, Laurent

- Emmanuel, et al.. Fluid systems and fracture development during syn-depositional 1 fold growth: an example from the Pico del Aguila anticline, Sierras Exteriores, Southern Pyrenees, Spain.. *Journal of Structural Geology*, Elsevier, 2015, 70, pp.23-38.
- Osborn, S. G., & McIntosh, J. C. (2010). Chemical and isotopic tracers of the contribution of microbial gas in Devonian organic-rich shales and reservoirsandstones, northern Appalachian Basin. *Applied Geochemistry*, 456-471
- Qinghua Lei, John-Paul Latham, Chin-Fu Tsang, The use of discrete fracture networks for modelling coupled geomechanical and hydrological behaviour of fractured rocks, *Computers and Geotechnics*, Volume 85, 2017, Pages 151-176.
- Rittenhouse G. (1967) Bromine in oil-field waters and its use in determining possibilities of origin of these waters. *Bull. Amer. ASSOC. Petrol. Geol.* 51, 2430-2440
- R. Meyer. Anisotropy of sandstone permeability. *CREWES Res. Rep.*, 14 (2002)
- Shedid, S.A. 2009. Influences of different modes of reservoir heterogeneity on performance and oil recovery of carbon dioxide miscible flooding. *Journal of Canadian Petroleum Technology*, 48, 29–35
- Sollars CJ, Peters CJ, Perry R (1982) Bromide in urban runoff—water quality considerations. *Effects of Waste Disposal on Groundwater and Surface Water (Proceedings of the Exeter Symposium, July 1982)*.IAHS 139:101–112
- S.I. Dworkin, L.S. Land. The origin of aqueous sulfate in Frio pore fluids and its implication for the origin of oil field brines. *Applied Geochemistry*. Volume 11, Issue 3, 1996, Pages 403-408,
- Stephan Bergbauer, David D. Pollard; A new conceptual fold-fracture model including prefolding joints, based on the Emigrant Gap anticline, Wyoming. *GSA Bulletin* 2004;; 116 (3-4): 294–307.
- Stephen E. Kesler, Anna M. Martini, Martin S. Appold, Lynn M. Walter, Ted J. huston, Francis C. furman. Na-Cl-Br systematics of fluid inclusions from Mississippi Valley-type deposits, Appalachian Basin: Constraints on solute origin and migration paths, *Geochimica et Cosmochimica Acta*, Volume 60, Issue 2, 1996, Pages 225-233.
- Taylor, J. C., 1976, *Geologic appraisal of the petroleum potential of offshore southern California: The borderland compared to onshore coastal basins*: United States Geological Survey Circular 730, 43 p.
- The Department of Conservation, Geologic Energy Management Division (Cal GEM), Well Finder. Retrieved May 09, 2020.

Tissot, B.P., and Welte, D.H., 1978, Petroleum formation and occurrence: New York, Springer-Verlag, 538 p.

Trembaczowski A. 1991. Sulphur and oxygen isotopes behavior in sulphates of atmospheric groundwater system observations and model. *Nordic Hydro* 22:49-66.

USGS, National Map 3D Elevation Program (3DEP). Retrieved April 12, 2020,

Warren J. K. (2006). *Evaporites: Sediments, Resources and Hydrocarbons*. Berlin: Springer; 10.1007/3-540-32344-9.

Winterer, E.L., and Durham, D.L., 1962, Geology of southeastern Ventura basin, Los Angeles County, California: U.S. Geological Survey Professional Paper 334-H, p. 274-366, 6 plates, map scale 1:24,000.

Xiaorong Luo, Zhijun Jin, Keyu Liu, Shuichang Zhang, "Geofluids in Deep Sedimentary Basins and Their Significance for Petroleum Accumulation", *Geofluids*, vol. 2017, Article ID 3571359, 4 pages, 2017.

Yeats, R. S., & Huftile, G. J. (1994). Late Cenozoic Tectonics of the East Ventura Basin, Transverse Ranges, California. *American Association of Petroleum Geologists Bulletin*, 78(7), 1040-1074.

Yu-Shu Wu. Chapter 2 - Multiphase Fluids in Porous Media, Editor(s): Yu-Shu Wu, *Multiphase Fluid Flow in Porous and Fractured Reservoirs*, Gulf Professional Publishing, 2016, Pages 15-27.

APPENDIX A.

Permeability Tensor Calculations

1) The fracture joints field measurements were converted into poles, then the mean vectors for all three fracture joint sets were calculated using Fisher Mean Vector from Allmendinger (2016) stereonet 11.

Outcrop 2

Fisher Mean Vector

<i>Poles to Bedding Joints</i>		<i>Poles to Longitudinal Joints</i>		<i>Poles to Transverse Joints</i>	
Trend	Plunge	Trend	Plunge	Trend	Plunge
212.5	16.8	31.2	73.7	110.6	51.4

2) The aperture of the fracture joints and the spacing between the fracture joints were averaged out.

<i>Bedding Joints</i>	<i>Longitudinal Joints</i>	<i>Transverse Joints</i>
Aperture = 1.24mm Spacing = 145mm	Aperture = 0.72mm Spacing = 954.61mm	Aperture = 1.23mm Spacing = 105mm

3) Using Chen et al. 1996 *Permeability Tensors of Anisotropic Fracture Networks* equation for a single set of parallel fractures, the permeability tensor for each fracture joint set was calculated.

$$[k_{ij}] = \frac{b^3}{12d} \begin{bmatrix} (n_2)^2 + (n_3)^2 & -n_1n_2 & -n_3n_1 \\ -n_1n_2 & (n_3)^2 + (n_1)^2 & -n_1n_2 \\ -n_3n_1 & -n_2n_3 & (n_1)^2 + (n_2)^2 \end{bmatrix}$$

Source: Chen et al. 1996

K_{ij} = Permeability Tensor

b = Fracture Aperture

d = Fracture Spacing

$n_1 = \cos(p) \sin(t)$

$n_2 = \cos(p) \cos(t)$

$n_3 = -\sin(p)$

p = Plunge

t = Trend

n_1, n_2 and n_3 are the components of the unit vector in the directions x, y and z, respectively.

Bedding Joints

$$[k_{ij}] = \begin{bmatrix} 8.9558e - 04 & 8.8965e - 05 & -4.0029e - 04 \\ 8.8965e - 05 & 1.0412e - 03 & 1.8967e - 04 \\ -4.0029e - 04 & 1.8967e - 04 & 2.2991e - 04 \end{bmatrix}$$

Longitudinal Joints

$$[k_{ij}] = \begin{bmatrix} 3.4042e - 05 & 1.1514e - 07 & 9.2004e - 07 \\ 1.1514e - 07 & 3.3542e - 05 & -4.1945e - 06 \\ 9.2004e - 07 & -4.1945e - 06 & 5.5018e - 08 \end{bmatrix}$$

Transverse Joints

$$[k_{ij}] = \begin{bmatrix} 1.3726e - 03 & -1.2580e - 04 & -3.3746e - 04 \\ -1.2580e - 05 & 1.2996e - 03 & -4.4924e - 04 \\ -3.746e - 04 & -4.4924e - 04 & 2.6197e - 04 \end{bmatrix}$$

4) After the calculation of each fracture joint set, matrix addition was used to calculate the overall permeability tensor of each outcrop.

Permeability Tensor of Outcrop 2

$$[k_{ij}] = \begin{bmatrix} 2.3022e - 03 & -3.6720e - 05 & -7.3684e - 04 \\ -3.6720e - 05 & 2.3743e - 03 & -2.6377e - 04 \\ -7.3684e - 04 & -2.6377e - 04 & 4.9243e - 04 \end{bmatrix}$$

5) Using the permeability tensor of each outcrop, the eigenvalues and eigenvectors were calculated using dcode.fr/matrix-eigenvalues, where λ is the eigenvalue with its corresponding eigenvectors.

Outcrop 2

$$\lambda_1 = 2.5806E-03, \text{ yield an eigenvector } \begin{bmatrix} E \\ N \\ Z \end{bmatrix} = \begin{bmatrix} -8.9035E - 01 \\ -2.9016E - 01 \\ 3.5083E - 01 \end{bmatrix}$$

$$\lambda_2 = 2.3893E-03, \text{ yield an eigenvector } \begin{bmatrix} E \\ N \\ Z \end{bmatrix} = \begin{bmatrix} -3.1349E - 01 \\ 9.4954E - 01 \\ -1.0262E - 02 \end{bmatrix}$$

$$\lambda_3 = 1.9909E-04, \text{ yield an eigenvector } \begin{bmatrix} E \\ N \\ Z \end{bmatrix} = \begin{bmatrix} 3.3015E - 01 \\ 1.1912E - 01 \\ 9.3638 - 01 \end{bmatrix}$$

6) The eigenvectors components (E, N and Z) that are in directional cosine were converted back to trend and plunge using the following excel formulas:

$$\text{Trend} = 180/3.14159 * \text{ATAN}(C55/D55) + \text{IF}(D55 < 0, 180, \text{IF}(C55 < 0, 360, 0))$$

$$\text{Plunge} = -180/3.14159 * \text{ATAN}(E55/\text{SQRT}(C55^2 + D55^2))$$

B	C	D	E	F	G	H	I	J	K	L	M	N	O	P
OUTCROP 2														
8.9558E-04	8.8965E-05	-4.0029E-04		3.4042E-05	1.1514E-07	9.2004E-07		1.3728E-03	-1.2580E-04	-3.3746E-04		2.3022E-03	-3.6720E-05	-7.3684E-04
8.8965E-05	1.0412E-03	1.8967E-04	+	1.1514E-07	3.3542E-05	-4.1945E-06	+	-1.2580E-04	1.2996E-03	-4.4924E-04	=	-3.6720E-05	2.3743E-03	-2.6377E-04
-4.0029E-04	1.8967E-04	2.2991E-04		9.2004E-07	-4.1945E-06	5.5018E-07		-3.3746E-04	-4.4924E-04	2.6197E-04		-7.3684E-04	-2.6377E-04	4.9243E-04
EIGENVALUE														
EIGENVECTORS														
	E	N	Z	Trend	Plunge			Trend	Plunge					
2.5806E-03	-8.9055E-01	-2.9016E-01	3.5083E-01	251.95	-20.54			71.95	20.54					
2.3893E-03	-3.1349E-01	9.4054E-01	-1.0262E-02	341.73	0.59			341.73	0.59					
1.9909E-04	3.3015E-01	1.1912E-01	9.3638E-01	70.16	-69.45			250.16	69.45					

7) Once the eigenvector trend and plunge were calculated, they were plotted in a stereonet.

	<i>Eigenvalues</i>	<i>Eigenvectors</i>	
		Trend	Plunge
1 st	2.58e-03	71.95	20.54
2 nd	2.39e-03	341.73	0.59
3 rd	1.99e-04	250.16	69.45

APPENDIX B.

Water sample physiochemical parameters

Sample ID	Sample Date	Temperature (°C)	pH	EC (microsemens)	Alkalinity (mg/L)	Alkalinity (meq/L)	TDS
O-S-1	9/4/2018	31.2	8.29	6850	4860	97.2	4384
O-S-1	9/23/2018	25.2	8.35	12150	4985.8	99.716	7776
O-S-1	10/9/2018	19.8	8.47	5800	4261.48	85.2296	3712
O-S-1	10/16/2018	19.2	8.31	4500	4771.61	95.4322	2880
O-S-1	11/8/2018	20.1	8.34	3111	4768	95.36	1991.04
O-S-1	12/2/2018	19.8	8.06	3589.2	4575.41	91.5082	2297.088
O-S-1	12/17/2018	19.2	7.99	11	4704.1	94.082	7.04
O-S-1	2/12/2019	14.5	8.1	1.8	3456.6	69.132	1.152
O-S-1	2/17/2019	14.2	8.07	12.3	4451	89.02	7.872
O-S-1	3/11/2019	16.5	8.14	11.7	3500.8	70.016	7.488
O-S-1	3/23/2019	15.2	8.33	10.5	4513.68	90.2736	6.72
W-S-1	9/23/2018	21.2	8.23	303.2	1912.75	38.255	194.048
W-S-1	10/9/2018	17.2	8.24	660	1769.74	35.3948	422.4
W-S-1	10/16/2018	17.4	8.4	380.7	1829.83	36.5966	243.648
W-S-1	11/8/2018	20.3	8.43	458	1901.73	38.0346	293.12
W-S-1	12/2/2018	17.8	8.01	458	2114.454	42.28908	293.12
W-S-1	12/17/2018	18.2	8.04	1.8	1879.9	37.598	1.152
W-S-1	2/12/2019	10.1	7.98	2.5	2211.4	44.228	1.6
W-S-1	2/17/2019	12.2	8.12	11	2004.4	40.088	7.04
W-S-1	3/11/2019	14	8.03	15.5	2366.8	47.336	9.92
W-S-1	3/23/2019	14.3	8.1	9.6	2008.25	40.165	6.144
W-S-2	9/4/2018	25.5	8.37	11510	5701.49	114.0298	7366.4
W-S-2	9/23/2018	26.2	8.34	24.5	5390.88	107.8176	15.68
W-S-2	10/9/2018	18.5	8.19	225.5	4585.23	91.7046	144.32
W-S-2	10/16/2018	18.7	8.15	500.3	4489.74	89.7948	320.192
W-S-2	11/8/2018	19.2	8.09	850.5	3546.56	70.9312	544.32
W-S-2	12/2/2018	15.2	7.81	789.2	4018.37	80.3674	505.088
W-S-2	12/17/2018	16.2	8.11	2.3	3897.7	77.954	1.472
W-S-2	2/12/2019	11.8	8.24	12	3789.6	75.792	7.68
W-S-2	2/17/2019	13.1	8.24	12.9	2879.6	57.592	8.256
W-S-2	3/11/2019	14.5	8.23	19.2	3006.8	60.136	12.288
W-S-2	3/23/2019	13.5	8.16	12.3	3781.28	75.6256	7.872
W-S-3	11/8/2018	12.5	8.66	120.2	2408.53	48.1706	76.928
W-S-3	12/2/2018	9.3	8.78	94.6	2456.76	49.1352	60.544

W-S-3	2/12/2019	10.1	8.15	4.5	2100.7	42.014	2.88
W-S-3	2/17/2019	10	8.1	6.5	1798	35.96	4.16
W-S-3	3/11/2019	11.2	7.9	5.6	1898.3	37.966	3.584
W-S-3	3/23/2019	12.5	8.16	6.3	848.36	16.9672	4.032
W-S-4	12/2/2018	11.6	7.78	43	579.8	11.596	27.52
W-S-4	12/17/2018	12.5	7.89	3.4	678.9	13.578	2.176
W-S-4	2/17/2019	10.1	8.11	7.5	614.44	12.2888	4.8
W-S-4	3/11/2019	10.2	7.93	4.2	376.92	7.5384	2.688
W-S-4	3/23/2019	12.9	8.3	5.2	703.1	14.062	3.328
W-STR-5	12/17/2018	11.3	7.78	4	345	6.9	2.56
W-STR-5	2/12/2019	10.3	7.78	4.9	411	8.22	3.136
W-STR-5	2/17/2019	10.3	7.79	6.1	578.98	11.5796	3.904
W-STR-5	3/11/2019	11.2	8.08	2.3	251.2	5.024	1.472
W-STR-6	12/17/2018	11.2	7.98	4.5	289	5.78	2.88
W-STR-6	2/12/2019	10.1	7.98	7.5	356.9	7.138	4.8
W-STR-6	3/11/2019	11	8.27	1.8	289.1	5.782	1.152
RW	2/17/2019	10.1	7.95	0	2949.69	58.9938	0

APPENDIX C.

Analytical results of water samples. The samples are displayed in microgram per liter mg/L. ND= not detected.

Sample ID	Sample Date	Fluoride	Chloride	Nitrate	Bromide	Sulfate
O-S-1	9/4/2018	0.27	2956.2853	31.1548	39.569	21.272
O-S-1	9/23/2018	0.2722	3223.4001	35.0152	0.628	9.935
O-S-1	10/9/2018	0.2194	2407.6561	25.9673	0.788	8.337
O-S-1	10/16/2018	0.1887	2374.8687	25.3403	8.42	12.524
O-S-1	11/8/2018	0.2245	2690.2383	31.8563	0.617	7.775
O-S-1	12/2/2018	0.2695	3129.0927	34.0395	0.633	9.472
O-S-1	12/17/2018	0.2983	3106.4338	32.708	32.366	9.336
O-S-1	2/12/2019	0.2899	2157.311	1.1861	37.653	24.241
O-S-1	2/17/2019	0.3156	2085.2417	21.1943	0.556	15.088
O-S-1	3/11/2019	0.2427	1871.6934	19.7975	ND	20.662
O-S-1	3/23/2019	0.256	2090.3139	20.9546	ND	15.641
W-S-1	9/23/2018	0.7023	146.8705	0.234	1.471	63.248
W-S-1	10/9/2018	0.7004	155.2623	1.5035	1.473	50.778
W-S-1	10/16/2018	0.7553	170.1339	0.2268	1.63	52.837
W-S-1	11/8/2018	0.7336	140.5796	0.9668	1.321	36.908
W-S-1	12/2/2018	0.7372	144.3817	2.4588	1.877	46.405
W-S-1	12/17/2018	0.7541	163.9507	0.2578	ND	23.98
W-S-1	2/12/2019	0.7734	163.3026	0.4565	1.421	66.539
W-S-1	2/17/2019	0.6887	142.7168	0.4005	1.223	50.79
W-S-1	3/11/2019	0.6537	134.3628	0.3212	1.323	64.939
W-S-1	3/23/2019	0.7952	136.0643	0.2829	1.128	51.036
W-S-2	9/4/2018	0.3426	8983.222	47.9187	ND	400.152
W-S-2	9/23/2018	0.2884	7423.0112	38.9154	ND	94.49
W-S-2	10/9/2018	0.212	6138.4986	30.6716	0.026	111.989
W-S-2	10/16/2018	0.1745	5691.6059	27.4724	2.516	82.322
W-S-2	11/8/2018	0.145	5161.6366	25.0172	26.916	37.541
W-S-2	12/2/2018	1.0878	6786.445	32.4151	42.607	66.183
W-S-2	12/17/2018	0.2807	6712.0361	33.2376	0.873	185.987
W-S-2	2/12/2019	0.3681	6028.1848	29.6096	2.031	181.467
W-S-2	2/17/2019	0.2826	4152.612	20.2596	0.244	859.284
W-S-2	3/11/2019	0.1543	4839.8455	23.5875	5.013	343.379
W-S-2	3/23/2019	0.1653	5144.9435	25.1013	0.747	119.771
W-S-3	11/8/2018	3.6186	203.1878	2.4014	3.121	120.977
W-S-3	12/2/2018	3.3429	193.8956	2.2494	2.34	423.943
W-S-3	2/12/2019	1.7097	79.9357	7.8222	0.688	1082.614

W-S-3	2/17/2019	1.6228	68.2527	5.6281	0.669	820.579
W-S-3	3/11/2019	1.5489	62.9695	0.4438	0.639	1086.239
W-S-3	3/23/2019	1.3715	62.3922	0.725	0.825	1262.694
W-S-4	12/2/2018	2.9686	477.8452	2.6316	3.468	1772.147
W-S-4	12/17/2018	2.5833	266.6004	2.1981	2.88	1401.999
W-S-4	2/17/2019	1.8069	78.2893	13.5183	0.877	2166.157
W-S-4	3/11/2019	1.6921	26.247	8.9615	0.228	1588.716
W-S-4	3/23/2019	1.8761	31.6758	1.3886	0.551	1856.319
W-STR-5	12/17/2018	2.5011	339.3298	9.2166	2.223	2956.959
W-STR-5	2/12/2019	2.0003	35.708	20.075	0.68	1942.269
W-STR-5	2/17/2019	1.8599	18.1239	28.7869	0.204	1499.559
W-STR-5	3/11/2019	1.8155	18.136	22.2189	0.243	1554.666
W-STR-6	12/17/2018	2.4166	362.9137	0.5697	2.653	2649.061
W-STR-6	2/12/2019	2.0741	45.1809	20.0498	0.417	2206.719
W-STR-6	3/11/2019	1.7222	19.5568	19.9781	0.311	1703.303
RW	2/17/2019	ND	0.78	0.4264	ND	1.264

